Ambient noise in the Ligurian Sea as background to acoustic particle detection

Masterarbeit aus der Physik

Vorgelegt von
Dominik Kießling
26. 03. 2013

Erlangen Centre for Astroparticle Physics
Physikalisches Institut 1
Friedrich-Alexander-Universität Erlangen-Nürnberg

Betreuer: Prof. Dr. Ulrich Katz

Contents

1. Introduction

The study of elementary particles originating from space, e.g. cosmic rays, gamma rays and neutrinos, is called astroparticle physics. A wide range of detection methods is used, and a lot of them were developed for experiments with particle accelerators. But also completely new techniques are investigated for their feasibility, as large detectors have to be constructed to get reliable statistics mainly at high energies.
A field, in which research is carried out only recently, is neutrino astronomy. The search for ultra-high energy neutrinos is motivated for example by the flux predicted by the *Greisen-Zatsepin-Kuzmin* effect [1, 2]. It predicts that protons propagating through space with energies above 10^{18} eV interact with photons from the cosmic microwave background, producing other particles in the process. Another reason for astronomy with neutrino telescopes at UH energies is the fact that neutrinos are the only viable messenger from sources of UHE particles (e.g. active galactic nuclei) beyond the local universe, as protons and photons cannot reach the earth without interactions or deflections from magnetic fields. It provides also an opportunity for cosmology to verify e.g. the top-down scenarios. Accordingly, many fields of research would highly benefit from a detector for neutrinos with energies at or above the GZK cutoff. But such a detector would require an effective volume on the order of 100 km^3. While this could be achieved with the classical Cherenkov detectors, it would produce enormous costs. Therefore, other detection techniques are considered.
One of these methods, studied for example at the Erlangen Centre for Astroparticle Physics (ECAP [3]), is the acoustic neutrino detection in water. Therefore the acoustic test system AMADEUS [4] has been integrated in the ANTARES detector [5], and several studies regarding the practicability of a full-scale acoustic detector were carried out. For example, the applicability of different sensor types, including self-made hydrophones, is investigated [6]. The read-out electronics for these sensors was also developed and characterized [7]. Further important aspects are signal classification, the development of efficient trigger algorithms [8] and the simulation of current and future detectors.
The main background for acoustic neutrino detection is the ambient noise in the sea. It determines the energy threshold of a future detector and a good knowledge is essential. Thus a parametrization of the noise spectrum is required for simulations for the feasibility of a large-scale acoustic detector. The analysis of the ambient noise in the deep sea as background for acoustic particle detection and the development of a model describing it will be the main focus of this thesis. A similar analysis was already performed e.g. by the SAUND-Collaboration [9] using a military array of the U.S. Navy located at the Tongue of the Ocean in the Bahamas.
The data for this thesis however was recorded by the sensors integrated in AMADEUS, and a short description of the detector will be given in the next section.

2. The ANTARES Detector

2.1. General information

This chapter will provide a brief summary about the ANTARES detector and its acoustic test system AMADEUS (see Fig. 2.1). For further reading their respective detector papers [10, 11] are recommended. ANTARES is the first operational neutrino telescope in the Mediterranean Sea. The detector was completed in May 2008 and has been taking data continuously since then. It is fixated at the sea bed in 2475 m depth, about 40 km away from Toulon or approximately 25 km from the French coast, as shown in Fig. 3.1. ANTARES is composed of twelve anchored *detection lines*, each kept taut vertically by a buoy at the top. On each line there are up to 25 storeys with three optical modules (OM). An OM contains a photomultiplier as active sensor element. The first instruments start about 100 m above the sea bed and the following storeys have a spacing of 14.5 m. The buoy finishes the line 20 m above the last storey. This leads to a total length of the lines of approximately 480 m. The anchors are arranged in an octagonal pattern with a quadratic inset on the sea bed, which defines the shape of the detector. One detection line, Line 12, has less optical modules than the other lines, but it has additional hydrophones for the acoustic neutrino detection test system AMADEUS. The whole detector-setup is completed by another line, the Instrumentation Line (IL). The IL houses instruments for environmental research and monitoring; additional hydrophones are located there as well.
The sensor data is digitized on the storeys, and then transferred optically with inter link cables to a junction box on the sea bed. A standard deep-sea communication cable connects the junction box with the onshore facilities. The power supply is also provided through these cables. Since the buoys are drifting in the current of the ocean, and the lines are also affected by sea currents, the position of the individual storeys is not fixed. In order to efficiently reconstruct the recorded events, it is necessary to know the position of the sensors with an accuracy on the centimetre scale. Therefore, an acoustic positioning system [12] is integrated in the setup. A transceiver (pinger) is mounted on the bottom sockets of each line, emitting a short acoustic sinusoidal signal with a defined frequency above 45 kHz. Each line has several receivers for these pings and the relative distance to the source can be trilaterated by the signal propagation times: Because the position of the transducers is well known, the position of each hydrophone can be reconstructed and the shape of the whole line can be determined by a fit. The maximum displacement of the buoy for high currents of $30\,\mathrm{cm\,s^{-1}}$ is less than 30 m, which is well below the distance between two lines. The emission of all pingers is repeated every two minutes and takes about 10 seconds.
Although the main purpose of ANTARES is neutrino detection, it can be utilized for different fields of research like earth and marine sciences, see e.g. [13, 14, 15]. As another example, the acoustic data is also used to determine the population size of whales and dolphins in the Mediterranean Sea and asses the impact of the anthropogenic noise on marine mammals [16].

2.2. Optical Neutrino Detection

The optical neutrino detection with ANTARES is based on the Cherenkov effect [17] in water. The ANTARES telescope detects the weak interactions of high-energy neutrinos with the

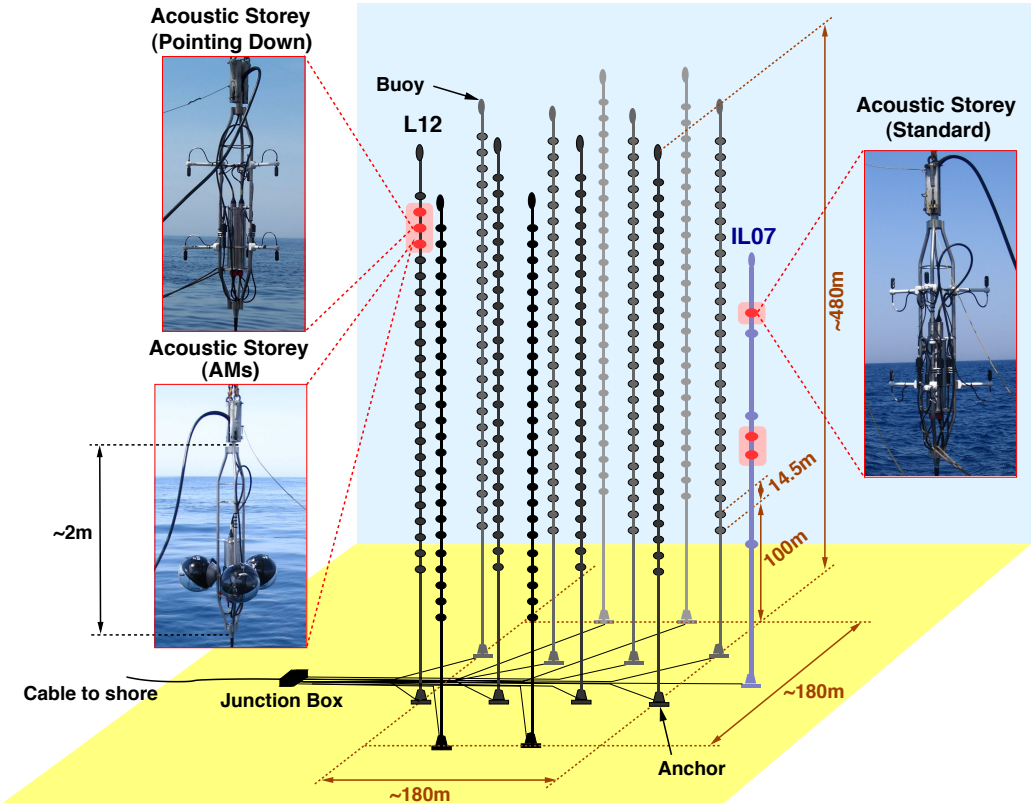

Figure 2.1.: *A sketch of the ANTARES Detector in the Ligurian Sea. The acoustic storeys (see Sec. 2.3) are marked in red. Adapted from [10].*

surrounding matter of the detector, where a charged lepton with high energy is produced in a charged-current interaction. Even though this detection principle works with all lepton flavors, it is best suited for muons, because of the long range of muon tracks. Due to their high energy, the velocity of the leptons is almost the speed of light in vacuum. The relativistic charged leptons produce a Cherenkov cone of light similar to a Mach cone in a sonic boom. The photons are emitted with an angle $\theta \approx 42°$ to the trajectory of the lepton, which is determined by the refraction index n of water and the velocity of the lepton β:

$$\cos\theta = \frac{1}{n\beta} \quad . \tag{2.1}$$

The Cherenkov photons are then recorded by the photomultiplier tubes in the optical modules. Since the attenuation length for light in the detected wavelength region approximately 60 m, it is necessary to use a instrumentation with spacings of the same order. Because the cosmic neutrino energy spectrum is assumed to follow a power law similar to the cosmic rays, the amount of events per unit volume is drastically reduced with higher energies. In order to get an effective volume, which is large enough to produce good statistics for neutrino events with energies above 1 EeV on a realistic time scale, while also keeping the costs in check, other detection methods are considered.

2.3. Acoustic neutrino detection with AMADEUS

A promising approach is acoustic neutrino detection. If a neutrino performs an interaction in sea water, a hadronic particle shower is initiated. The whole energy of the shower is deposited in a small column of ~10 m length. Because the particles in the shower are highly energetic, they travel almost at the speed of light, which means that the timescale for the energy deposition is

almost negligible compared to the time it takes for the sea water to return to an equilibrium state. Accordingly, this column of water is heated up and expands acceleratedly, causing a tiny explosion. The superposition of all elementary sound waves originating from this column leads to a bipolar pressure pulse with emission mostly perpendicular to the direction of the shower. One can imagine the propagation geometry of this sound signal as a flat disk, often referred to as *pancake*. The sound generation is predicted by the thermo-acoustic model [18, 19] and has been verified by previous experiments [20]. The advantage compared to the optical detection is the increased attenuation length in the magnitude of 1 km. Accordingly, the detector requires less instruments in the same volume, and the attenuation is no longer the limiting factor for sensor spacing.

To investigate the acoustic technique, the test system AMADEUS (ANTARES Modules for the Acoustic Detection Under the Sea) has been integrated in the ANTARES detector. The system consists of 36 sensors, which have been mounted on 6 different storeys spread across two lines: three on the IL and another three on a detection line (Line 12). So there is a total of 6 sensors per storey, which enables the reconstruction of the direction of an incoming signal and allows to apply a coincidence trigger, increasing the purity of the recorded events, both on the storey level. Since AMADEUS is an R&D project, three different sensor types are used: commercial hydrophones (HTI [21]), custom-built hydrophones (called LTI) and acoustic modules (AM). An acoustic module consists of two piezoelectric sensors, that are glued into a standard glass sphere as used for the optical modules. The hydrophones (see Fig. 2.2) also contain piezoelectric elements, but they are coated with polyurethane and can be put in direct contact with the sea water. The hydrophones show a strong dependency of the sensitivity on the receiving angle, because the preamplifier and the cable junction are positioned at the same end of the hydrophone, blocking the sound signals from this direction; and due to the cylindric shape of the piezo. The sensors are designed with a low self noise and an approximate sensitivity of $-145\,\mathrm{dB\,re\,1\ V/\mu Pa}$. The calibration of the hydrophones was performed in the laboratory with a calibrated emitter. It is limited to frequencies above 15 kHz, because the measurement is not significant for low frequencies, due to the quadratic frequency dependency of the emitter's transmit voltage response [6].

An acoustic storey consists of a titanium support structure that holds the electronics container and the sensors, either on arms or in glass spheres (AM). The hydrophones are distributed in the following way: Line 12 has a total of three acoustic storeys, each one with a different kind of sensor. On storey 21, counted from the bottom, there are AMs, storey 22 has downwards pointing HTIs, and storey 23 upwards pointing LTIs. The IL also houses three storeys, all with hydrophones facing upwards. Here, storey 2 and 6 hold HTI sensors, and storey 3 holds LTIs. The distance between the upper two of the acoustic clusters on the IL is 80 m, while the distance of the other neighboring storeys is 14.5 m. The horizontal distance between the anchors of the IL and Line 12 on the sea bed is about 240 m and the maximum distance between acoustic storeys on different lines is 340 m.

A custom-built electronics board, the AcouADC board, digitizes the data. It has several purposes: it performs an adjustable amplification of the analogue signal and anti-aliasing filtering; the board provides the power supply for the sensors and the interface for control from the shore. The amplification can be set to 12 different values from 1 to 512 through slow control commands. The standard value for the gain factor is 10, which leads to a typical hydrophone sensitivity of $-125\,\mathrm{dB\,re\,1\ V/\mu Pa}$. The sampling rate for the digitization can also be adjusted to 125 kSps (kilo Samples per second), 250 kSps or 500 kSps. The normal operation mode uses the 250 kSps sampling frequency (called DS2). The whole board acts as a bandpass filter, with the 3 dB cut off at 2.8 kHz and 108.8 kHz for DS2. Therefore, the data acquisition suffices the Nyquist-Shannon sampling theorem and the low frequency noise is removed, preventing a saturation of the electronics (mainly due to ambient noise, see Sec. 3.2).

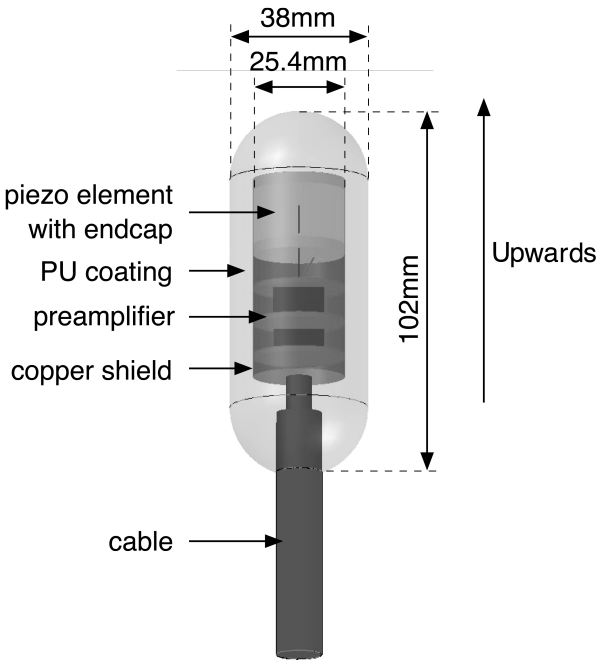

Figure 2.2.: *A schematic of the hydrophones used for AMADEUS. A pointing direction is defined due to its directional sensitivity. Adapted from [10].*

The data is transferred to the onshore facilities, where it is processed by 4 server-class computers. In order to keep the amount of data manageable, only the events which meet certain trigger criteria are stored. There are currently three different trigger schemes implemented, a pulse shape recognition trigger, a threshold trigger and a minimum bias trigger. For the analysis done in this thesis, only the minimum bias data is relevant, because a study of the ambient noise should not include transient signals, which are basically the only events that meet the requirements to pass the other two trigger mechanisms. The minimum bias trigger records a $\sim$10 s long data sample roughly every hour from all sensors, without any prerequisites. There is no guarantee that this sample is devoid of transient sources or positioning cycles, but it provides a realistic estimation for the average sound pressure level. Therefore it is best suited for the study of the ambient noise in the deep sea.

3. Weather and Noise in the Sea

3.1. Weather conditions at the ANTARES site

Figure 3.1.: *A map displaying the position of ANTARES (A) and the weather stations 0 to 4 (B to F respectively). The routes of regular ferry traffic are also shown with dashed lines. Source: Google maps.*

The weather conditions at the ANTARES site are one of the key components for the analysis of the ambient noise in the deep sea, since we are looking for a correlation between the wind speed and the recorded noise level. Therefore, it is essential to be able to determine the local weather conditions. Since the ANTARES site is located 40 km off the coast of Toulon, it is not feasible to get continuous weather data without a moored buoy. Because there is no buoy in close proximity, one has to rely on data provided by weather stations located at the Mediterranean coast. The locations of the stations considered (see Tab. 3.1) in this analysis are displayed in

Table 3.1.: *Location identifiers and positions of the weather stations used. The identification number used by the World Meteorological Organization (WMO) is also shown.*

Location	Station number	WMO ID	Position
Toulon	0	076600	43°6′N 5°56′E 2.7 m ASL
Cap Cépet	1	076610	43°5′N 5°56′E 13.6 m ASL
Îles d'Hyères	2	076670	43°6′N 6°9′E 0.4 m ASL
Porquerolles	3	076700	43°N 6°14′E 14.7 m ASL
Île du Levant	4	076780	43°2′N 6°28′E 13.1 m ASL

Fig. 3.1. The distance between the detector and the weather stations is obviously quite large, but the ocean only reacts to long–term average wind conditions, and not local gusts. The weather is a continuous phenomenon, so the measured value at the coast can be used as an estimate for the off–shore wind conditions. However, the wind speed changes at the coast line, depending on whether the the wind blows landward or offshore. The sea surface is usually much smoother than the landscape, which leads to reduced friction at the air/sea interface compared to the air/ground interface. In general, the wind speed on the ocean is usually larger than on shore. Therefore, one has to consider the surrounding landscape of the weather station, and also if there are dunes or hills which block the landward wind. The stations 1 and 4 are close to the coast line and have few obstacles to the shore, so these seem to be the best candidates to estimate the wind speed at the ANTARES site, as it was concluded in a previous thesis [22]. The wind speeds are recorded hourly by the weather stations. The distribution of the measured values at Cap Cépet in the years 2008 – 2011 can be seen in Fig. 3.2. A modified Maxwell distribution $f(v)$ can be used to fit the data (done here with ROOT [23]):

$$f(v) = a \cdot v^b \cdot \exp\left(-c \cdot v^d\right) \tag{3.1}$$

v is the wind speed in $\mathrm{m\,s^{-1}}$, with $a = 0.61(8)$, $b = 2.21(7)$, $c = 1.9(1)$ and $d = 0.75(2)$. However the resulting reduced χ^2 is quite large with 19.2. If you apply the smoothing algorithm also provided by ROOT to the distribution, the reduced χ^2 drops to 7.94. The formula 3.1 is probably not correct to describe the distribution, since the wind speed does not follow a Gaussian distribution. Additionally the data of the wind speeds conatins a rounding error, because its unit is converted with a limited precision before it becomes available for this analysis. This could explain the irregular bins at 7 kn to 8 kn and 16 kn to 17 kn.

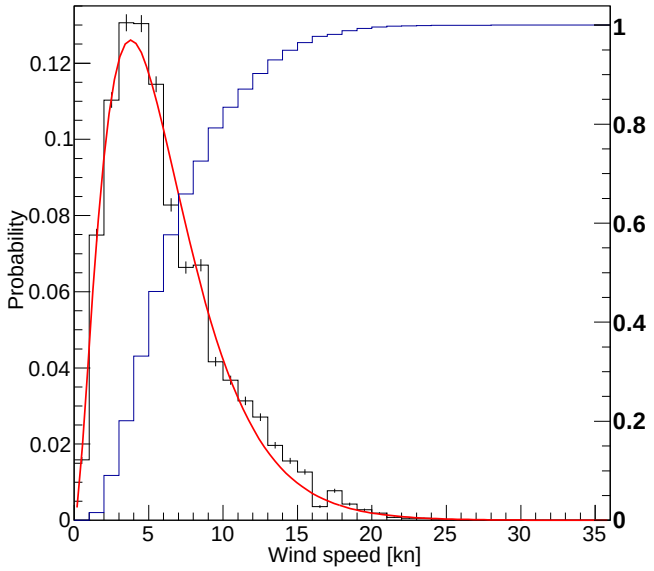

Figure 3.2.: *The occurrence of the 10–minute-averaged wind speed at weather station 1 (Cap Cépet) with a* 1 kn *bin size (black histogram, left ordinate). The blue graph (right ordinate) is the integrated probability of occurrence and can be interpreted as the probability of having equal or less wind speed, while the red line (left ordinate) is a modified Maxwell distribution fitted to the data, see Eq. 3.1.*

Sea states are linked to the Beaufort scale for wind speeds, but they describe the average wave height of the ocean. Because the wind agitates the sea and is accordingly the driving force for the waves, the sea state can be basically considered as an indication of the wind speed. A table with the wind speed corresponding to a sea state is shown in Tab. 3.2. The rate of occurrence of these weather conditions at weather station 1 is also displayed there. The Mediterranean Sea is

Table 3.2.: *Values describing the sea state as used by the World Meteorological Organisation. The number of recorded events with these conditions as well as the probability for that wind speed at weather station 1 (Cap Cépet) is shown in the last two columns. The data was measured once every hour in the years 2008–2011. Only values where AMADEUS and the weather station took data are considered.*

sea state	wave height [m]	wind speed [kn]	occurrence	probability [%]
0	0	$0-3$	5349	20.10
1	$0.0-0.3$	$4-6$	9989	37.54
2	$0.3-0.6$	$7-10$	6859	25.78
3	$0.6-1.2$	$11-16$	3811	14.32
4	$1.2-2.4$	$17-21$	538	2.02
5	$2.4-4.0$	$22-27$	57	0.21
6	$4.0-6.1$	$28-40$	4	0.02

quite calm, since the sea state derived from the wind speed is 1 or less for 58% of the time. For another 40% of the time the wave height is lower than 1.2 m. Accordingly, only very few days with high waves occur. However, there is another phenomenon called swell. It is independent of the local weather conditions, but it is caused by wind in a distant region and the generated waves travel along the ocean surface. Because the wind is measured onshore and due to the swell, the derived sea state should only be considered as an estimate. The estimator value can easily differ by one or even more from the real value, underestimating it most of the time.
Figure 3.3 shows the measured wind speeds and directions at Cap Cépet in a polar plot. The radial coordinate is the wind speed and the color in each bin marks the number of entries. There are two clearly preferred directions, from the Northwest (310° to 330°) and East (80° to 110°). This is caused by two weather phenomenona, the Mistral and the Levant. The Mistral is the Northwest wind in southern France, which is either caused locally by the different heat capacities of water and land during July or a certain constellation with an area of high pressure in the Bay of Biscay and an area of low pressure in the Gulf of Genoa, which can occur during the whole year. The Levant is an easterly wind in southern France and the west of the Mediterranean Sea with moderate strength. It can occur any time in the year, but it reaches its maximum strength from May to October.

The impact of these winds can be seen in Sec. 4.3.

3.2. Acoustic Background

The acoustic background for neutrino detection in the sea consists of multiple components, each one with a different origin. The first part to consider here is the shipping noise. The increasing marine traffic is the source of most of the noise in the ocean. A ship usually produces low frequency noise, which peaks below 1 kHz caused by the engine and the propeller. This is the main source for noise in this frequency domain, and because the attenuation length in seawater is so large[1], even ships in a distance of tens of km contribute to the total noise level. This part of the frequency spectrum has to be removed by the bandpass filter of AMADEUS in order to prevent a saturation of the electronics, but acoustic neutrino detection is still possible, because the expected signal has its peak at a frequency of about 10 kHz. But if the propeller rotates fast enough for cavitation to occur, the bubbles generated by this effect will cause an additional broadband noise. Unless the ships were built specifically to prevent cavation, which is only the

[1] Attenuation length for a plane wave at the sea surface with 1 kHz is: $\sim$70 km and for 10 kHz it is: $\sim$5 km

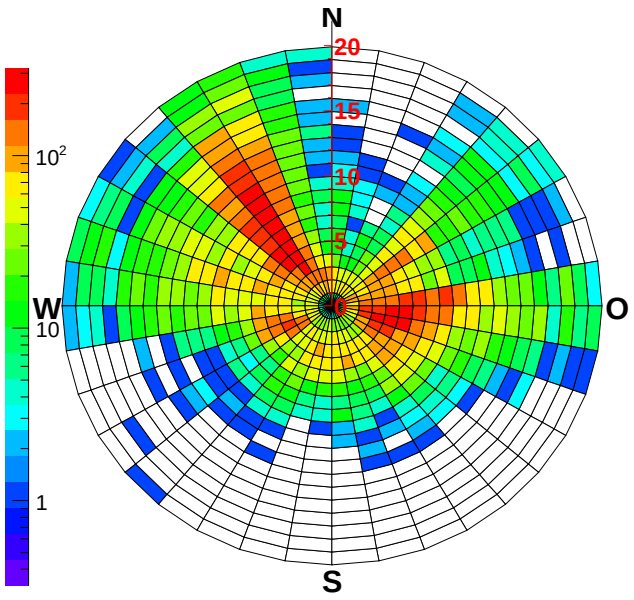

Figure 3.3.: *Polar plot of the wind speeds and corresponding wind directions at station 1 (Cap Cépet). The wind speed in knots is used as the radial coordinate, while the logarithmic color code represents the number of recorded events.*

case for military vessels like submarines, it will occur within the normal operational conditions for the ships. The ship itself can produce a lot of triggered events, if it is close enough to the detector to be resolved. Otherwise the shipping noise will simply contribute to the ambient noise level and thus raises the detection threshold of a signal. As a result, the best location for acoustic particle detection would be in an area that is completely blocked for shipping, which is highly unrealistic.
The next source of sound that should be mentioned here is marine life, like sperm whales, dolphins and snapping shrimps. Whales and dolphins for example use acoustic signals for their communication and orientation. These signals are in a frequency range of 10 kHz to 20 kHz, which happens to be the same range that is relevant for the acoustic neutrino detection. So, they are a source of transient signals, but they will usually send multiply signals from a similar position. Because it is very unlikely that multiple neutrinos interact with the matter in the ocean at the same place and time, the clustering of the events can be used to filter these signals. Additionally, each species produces a characteristic signal, which can also be used to identify and classify them (see [24]).
A further component of the noise in the deep ocean environment is the noise produced by the waves at the sea surface and the thermal noise of the water. This is the main focus of this thesis and it will be explained further in the next section.

3.3. Knudsen curves

The noise caused by the waves and its connection to the weather has been investigated for the first time in the second world war. The driving force behind these studies was the submarine warfare in the Atlantic. It was essential to detect the undersea boats, and the only working technique was the acoustic detection with active sonar. Therefore a parametrization of the ambient noise became necessary for the development of sonar systems and the correct interpretation of the signals. The first major analysis has been published by Knudsen et al. in 1948 [25]. The results of this study were the so called *Knudsen curves* (see Fig. 3.4), which

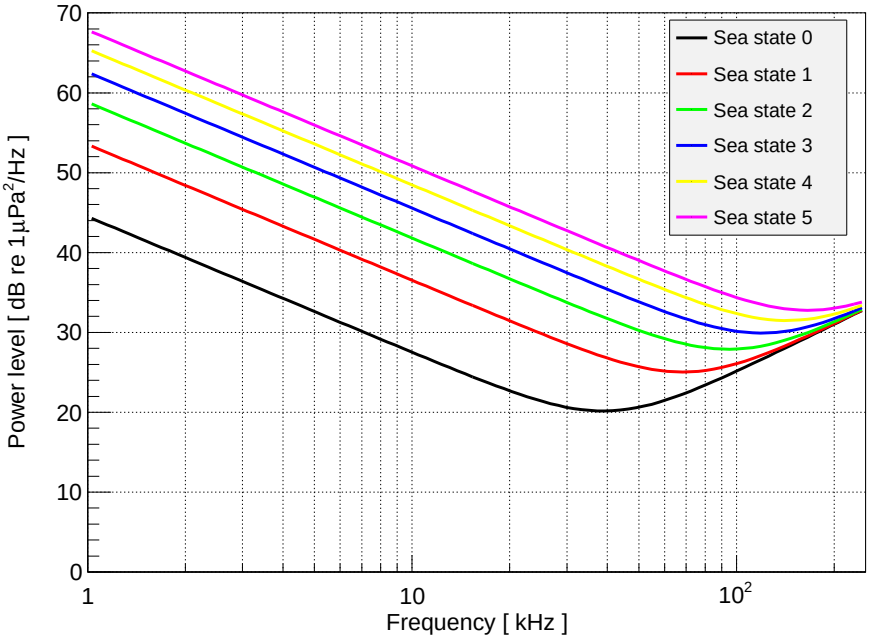

Figure 3.4.: *The Knudsen spectra and the thermal noise. The different colors represent the expected spectrum for different sea states.*

describe the relation between the noise level produced by waves and the sea state as well as the spectral behavior. In this model the spectrum is assumed to follow a power law:

$$P = NL_{1k} \cdot \left(\frac{f}{1\,\mathrm{kHz}}\right)^{i} \quad . \tag{3.2}$$

The value of NL_{1k} depends on the sea state and therefore also wind speed, while the spectral index i is assumed to be constant. The *Knudsen spectra* describe the dominant source of noise in the frequency range of 0.5 kHz to 50 kHz, but they are only valid for shallow water and do not account for local phenomenons.
The thermal movement of the water molecules hitting the surface of the hydrophones causes a high frequency noise, that rises in intensity with a spectral index of 2 [26]. Within this parametrization the thermal noise dominates the noise generated by waves above $\sim$50 kHz, which is still relevant for the acoustic neutrino detection. Simple formulas for the Knudsen curves NL, the thermal noise TN and the total noise TNL are:

$$\mathrm{NL} = 44.5 - 17 \cdot \log_{10}(f) + 30 \cdot \log_{10}(1 + ss) \tag{3.3}$$

$$\mathrm{TN} = -15 + 20 \cdot \log_{10}(f) \tag{3.4}$$

$$\mathrm{TNL} = 10 \cdot \log_{10}\left(10^{\mathrm{NL}/10} + 10^{\mathrm{TN}/10}\right) \tag{3.5}$$

Here ss is the sea state, f the frequency in kHz and the value for the noise level is returned in dB re 1 µPa^2/Hz. A plot of this function is displayed in Fig. 3.4

4. Ambient noise analysis

4.1. Raw data

Determining the ambient noise in the ocean with AMADEUS can be done by analyzing the minimum bias data. These samples are approximately 10 s long and they are recorded roughly once every hour. This provides 24 measurements per day for each sensor, which itself is not much, but since the data has been taken continuously since the setup was operational, a total of over 20 000 events were recorded for all hydrophones. Assuming that there are no signals in the sample, the ambient noise level can be estimated by the standard deviation of the recorded waveforms. The distributions of this value can be seen in Fig. 4.1. The mean value of these

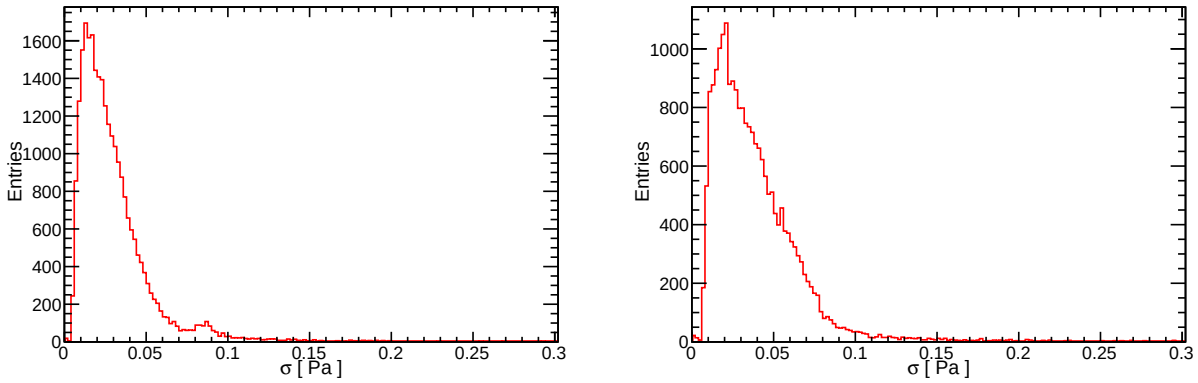

(a) Sensor 11 (b) Sensor 23

Figure 4.1.: *Distribution of the recorded noise level for the two hydrophones that are analyzed further. Also note the similar shape to the distribution of the wind speeds in Fig. 3.2.*

distributions for all 18 HTI hydrophones in the full frequency range is 34(3) mPa and the standard deviation is 36(4) mPa. The median of all these distributions is 26(3) mPa. These values mean that there are outliers in the samples, which greatly increase the standard deviation and the average value, while the median is less affected. In Figure 4.2 a power spectral density (PSD) of the unfiltered events is shown. It displays the noise power density contained in a small frequency band. In order to display the periodograms for all events, they were filled in a two dimensional histogram with a 500 Hz times 0.5 dB bin size. The color of each bin represents the amount of entries. The plot shows clear signs for transient sources, as there are for example the peaks at 45 kHz caused by the positioning system. The lower limit in that scatter plot is caused by the inherent noise of the sensors. The outliers below this lower limit are caused by test runs with a lower gain setting.

Another main feature for the analysis of the ambient noise is the correlation between the wind speed and the noise in the deep sea. If one assumes that the sources of the sound are mainly waves, which are driven by the long-term wind conditions (see Sec. 3.3), then it should be possible to observe an increasing sound level with increasing wind speed. For this analysis it is best to cover the longest possible time span, which cannot be done with a single hydrophone. The reason for that is the fact that the IL was only active from 2008 to 2010, while Line 12 had a long maintenance in 2009 and has been active since then. For example the correlation

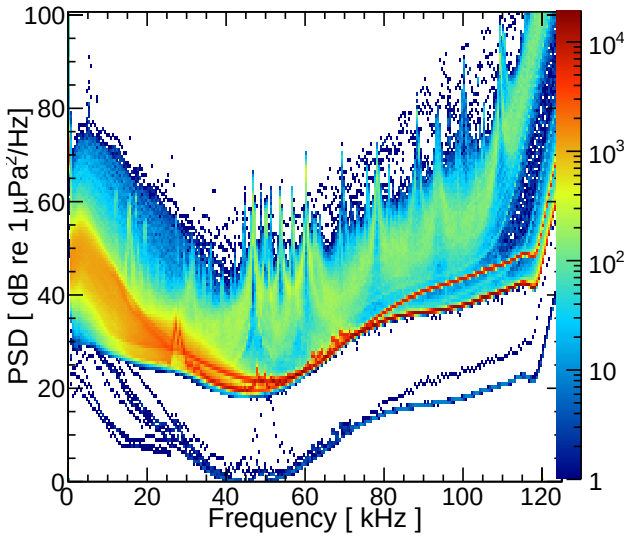

Figure 4.2.: *A scatter plot of the power spectral density of the unfiltered minimum bias data. There are clear signals in the spectrum, which means that the data has to be filtered in order to see the ambient noise.*

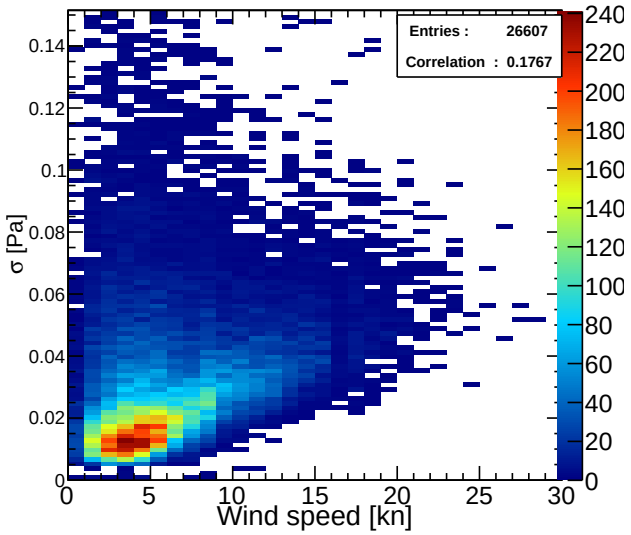

Figure 4.3.: *The correlation between the wind speed measured on shore at station 1 and ambient noise is displayed here.*

factor between the unfiltered data of sensors 11 (on the IL) and 23 (on Line 12) and the wind speed is 0.18, but there are also clear outliers visible in Fig. 4.3. This dataset was taken in the years 2008–2011. All of these outlying events are caused by transient sources, which should not be included in the analysis of the ambient noise. Because the measured data are just random intervals chosen by the minimum bias trigger, they will also include the pings of the ANTARES positioning system, shipping noise or other signals. The noise generated this way is obviously not related to the wind speed and therefore reduces the visibility of the correlation. Consequently, the minimum bias data has to be filtered in order to see the real ambient noise and the correlation factor.

4.2. Filtering the data

In order to remove the samples that contain transient sources, different types of cuts are used. First, there is a filter for signals at high frequencies, that is used mainly to remove the events with pings of the positioning system. The pingers operate with signals in the range 40 kHz to 65 kHz. The filter calculates the average sound level from 45 kHz to 80 kHz and discards all events with a value that is not within a specified range.
The next cut tests if the distribution of the amplitudes has similar tails like a Gaussian distribution, as one would expect it for random noise. The computation is executed in the following way: the recorded voltage during the 10 s frame is filled in a histogram. The mean value $\overline{x}$ and the standard deviation σ are determined. Then the ratio of the number of entries in the range $\overline{x} - \sigma$ to $\overline{x} + \sigma$ to the total number of entries is evaluated. Like the previous filter, only events that are in a certain parameter range are accepted. The purpose of these first two cuts is removing all transient signals, that would cause a peak in the spectrum, because it is safe to assume that the ambient noise has none. The values of these filter criteria were adjusted in such a way that almost all samples with peaks are discarded.
It is also possible that a transient signal has a broad noise spectrum, which simply increases the overall sound level, e.g. noise of far away shipping traffic. Removing events that are corrupted with this kind of signal is difficult. But it can be assumed that the ambient noise should change slowly with the weather conditions, unless it starts to rain. So it is plausible to put a constraint on the rate at which the noise level can increase in between subsequent measurements, see [27]. By calculating the difference of the noise level s_n in sample n and its predecessor s_{n-1}, one will get a histogram with a distribution that is centered around 0 and falls off fastly. Now it is possible to get an estimate of the rate of change in the noise level that is caused by natural means and not by anthropogenic ones, by simply looking at the width of the distribution. The standard deviation would be a huge overestimation for that rate, because there are many outliers caused by appearing and disappearing signals. It is advisable to fit a simple function, which is robust against outliers, to determine the width. Although its shape clearly differs from a Gaussian, it still can be used to get an estimation for the width. The reason to do it this way is the ease of reproducing the same analysis with different data. The width of the distribution has been determined to $3.7 \times 10^{-4}\,\mathrm{V}$ by a Gaussian curve fitted to the data of several HTI hydrophones. This value is now used to discard all events where one of the following conditions is met:

$$s_n - s_{n-1} > 3.7 \times 10^{-4}\,\mathrm{V\,h^{-1}} \cdot (t_n - t_{n-1}) \tag{4.1}$$

$$s_n - s_{n-2} > 3.7 \times 10^{-4}\,\mathrm{V\,h^{-1}} \cdot (t_n - t_{n-2}) \tag{4.2}$$

The first condition (Eq. 4.1) removes events with appearing signals and the second condition (Eq. 4.2) checks if an older signal has already disappeared. On its own, this filter provides the most efficient way to increase the correlation between the wind and the noise in the further analysis. However it will only remove some events with signals from the positioning system. Therefore it is crucial to apply all three of the described filter methods, if one wants to get a pure sample of the ambient noise. Finally, since we want to correlate the ambient noise with the wind speed, there has to be weather data available when the event was recorded. If there was no weather measurement within an hour, the event is also discarded (time offset). The actual parameters that were used for the cuts in this analysis are:

$$\begin{aligned} \text{High frequency filter} &\in [25\,\mathrm{dB}, 29\,\mathrm{dB}] \\ \text{Amplitude distribution} &\in [0.38, 0.44] \\ \text{Time offset (weather/noise)} &< 3600\,\mathrm{s} \\ \text{Maximum change rate} &= 3.7 \times 10^{-4}\,\mathrm{V\,h^{-1}} \end{aligned}$$

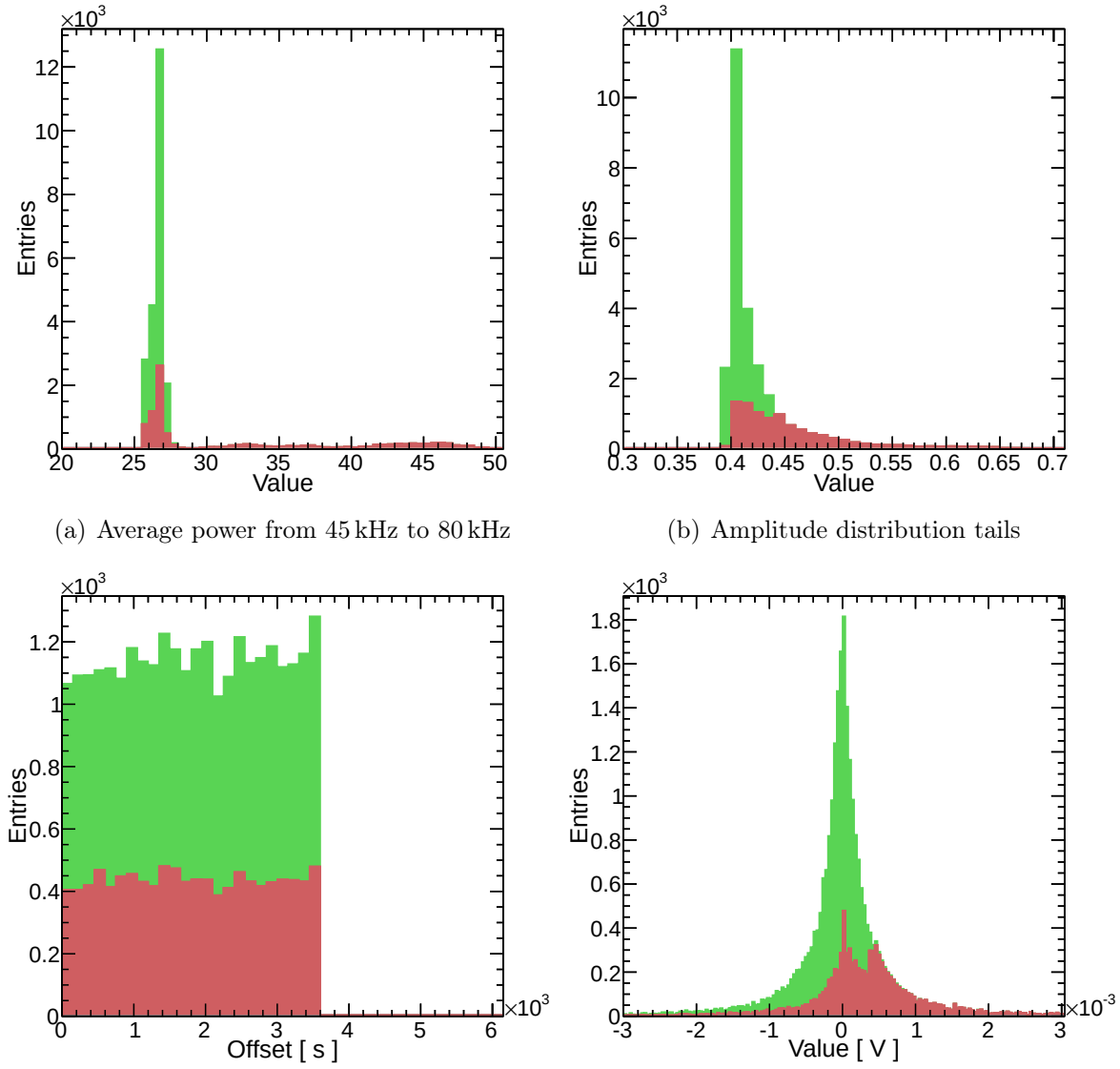

(a) Average power from 45 kHz to 80 kHz

(b) Amplitude distribution tails

(c) Time offset

(d) Noise difference between two events

Figure 4.4.: *Distributions of the values used for the cuts described in the text. The accepted events are shown in green, while the discarded ones are red. The histograms are stacked, so all events are displayed.*

The distribution of the filter values and the effects of the combined cuts are displayed in the Fig. 4.4. It is also possible to see if two filter trigger on similar events or if they are independent of each other. For example the time offset filter is independent of all others, because the events removed through them are equidistributed in the offset histogram. That is obviously the expected result, because it would be really strange if the time difference between the noise and weather measurement had an effect on the amount of transient sources. The high frequency filter and the Gaussian shape filter basically remove the same events, while the difference filter is independent of the latter two. In total these filters remove about 40 % of all recorded events. While that may sound high, one has to consider that over 10 % of the time frames contains signals of the ANTARES positioning system, and that there is regular ferry traffic above the ANTARES detector site, which renders at least another 20 % unusable for the analysis of the background ambient noise.

In order to get an estimate of the performance of the cuts, see Fig. 4.5. For this Figure the standard deviation of the recorded minimum bias samples is filled into histograms for each hour

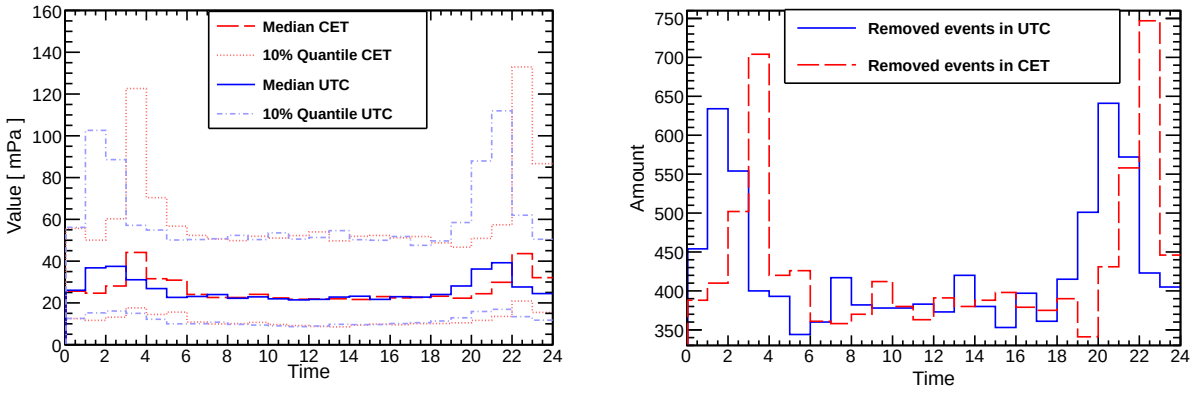

(a) Quantiles (b) Events removed

Figure 4.5.: *Graph (a) shows the quantiles of the distribution of the standard deviation from the minimum bias data of a HTI hydrophone during a day without filtering. There is a clear difference in the shape of the curves, depending on whether the daylight savings time is considered or not. Panel (b) shows the number of events removed per hour in the day, showing that the cuts used for the analysis are triggered more often during these high noise periods.*

of the day. The values are put in the histogram corresponding to the time when they where recorded. The quantiles of these distributions are displayed there together with the amount of events cut by the filter during each hour. There are significant peaks in the sound level between 3:00 to 4:00 and 22:00 to 23:00 in the local time (CET), that smear out if the daylight savings time is not considered. There is actually no reason, why that should happen, if the peaks are caused by biological activities or a natural weather phenomenon. The wind speed also shows no maxima for these time intervals. Therefore it is safe to assume that these peaks are caused by scheduled events like ferries passing the detector. Most ferry routes have night passages that depart on 21:00 o'clock, e.g. Toulon – Ajaccio [28]. These ferries travel at about 18 kn or 33 km h^{-1}, and since the detector is located about 40 km off the coast of Toulon, they will pass it about one hour later explaining that peak [29]. The second peak can be explained with the return passages, that also depart at 21:00 but take much longer to reach the detector, since it is now located at the end of the route. Although there are up to 30 trips per day, only the night passages have synchronized departure times, which causes a higher noise level than on average. The cuts also remove significantly more events in the same time intervals and show the same behavior regarding the daylight savings time.
The cuts have the following effect on the distribution of the recorded values for the standard deviation for all HTI hydrophones in the full frequency range: The average value is now 22(3) mPa, with the standard deviation of 11(2) mPa and the median is 20(3) mPa (see Fig. 4.6 for two examples). The standard deviation is drastically reduced, which was the intent behind the cuts. Most outliers are discarded, and the average and the median now yield similar values.

4.3. Long term correlation between ambient noise and wind speed

After the data has been filtered, it is possible to analyze the correlation between the wind speed and the ambient noise. Like in most cases in science, the bigger your statistical sample, the better are the results. So it is desirable to have a large sample of data, which requires a long operation time. But there were different periods of time, where one of the lines was not

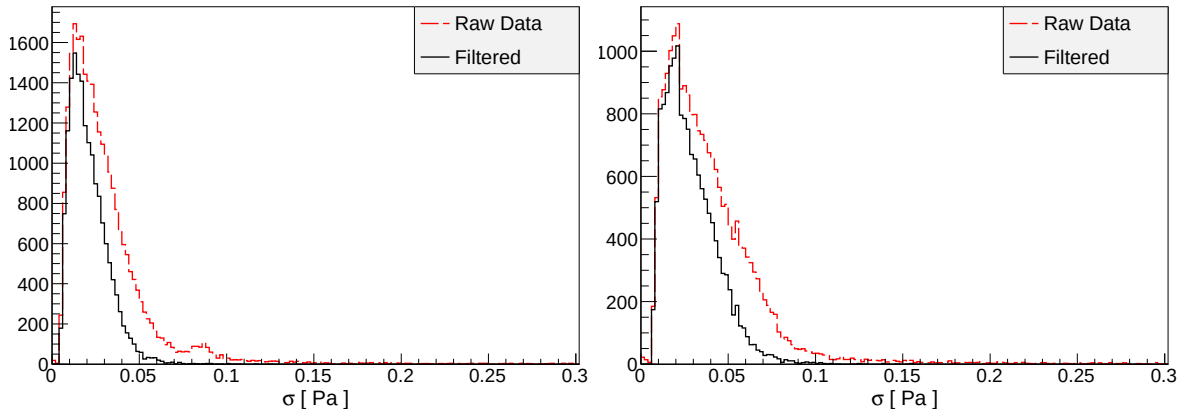

(a) Sensor 11 (b) Sensor 23

Figure 4.6.: *Filtered distribution of the recorded noise level for the two hydrophones that are analyzed further.*

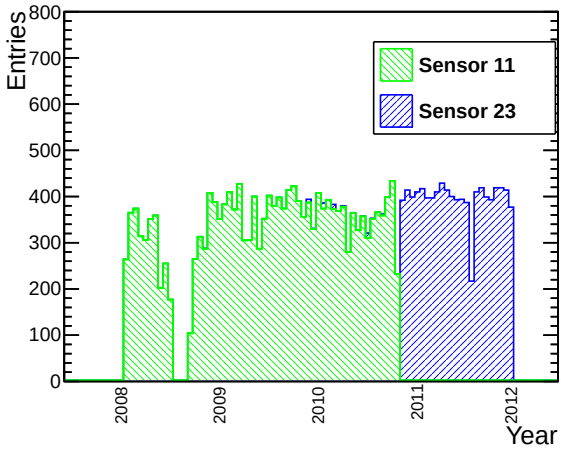

Figure 4.7.: *Histogram (19 days bins) of the recorded events by sensor.*

available for data taking (e.g. a broken cable, maintenance). Thus it is not possible to achieve the maximum coverage if one only considers a single hydrophone. In order to maximize the amount of data available, two different hydrophones were used for this study, one mounted on Line 12 and one mounted on the Instrumentation Line. Sensor 11 on the Instrumentation Line was prioritized, and if there was no data available sensor 23 was used, see Fig. 4.7. Both of these hydrophones are commercial ones from HTI, so that a similar sensitivity and inherent noise is ensured.

This leads to a sample size of 27 425 measurements acquired with the minimum bias trigger during 2008–2011, while there is only weather data available from station 1 for 26 607 measurements. After the cuts are applied, only 16 931 events remain, 61.7% of the original amount. The connection of the wind speed measured at Cap Cépet and the sound level is made visible by a two-dimensional histogram, as shown in Fig. 4.8. The correlation factor for this plot is 0.73. This shows that there is indeed a direct connection between the wind speed and the ambient noise in the deep sea. There is an almost linear relation between these two values, but there are statistical uncertainties. Using different weather stations to relate the wind speed and the noise yields similar results for the correlation factor, 0.70 for station 3 and 0.69 for station 4. Station 3 however only records data every 3 hours, reducing the amount of data significantly. The weather stations 0 and 2 are not directly at the coast, so the quality of the data is reduced and the correlation factor is only about 0.5. So there are two stations with

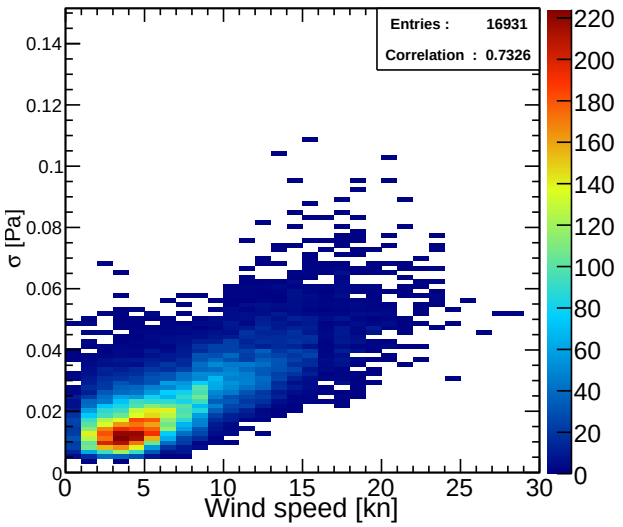

Figure 4.8.: *The correlation between the wind speed measured on shore at station 1 and the ambient noise. The color of each bin marks the number of entries.*

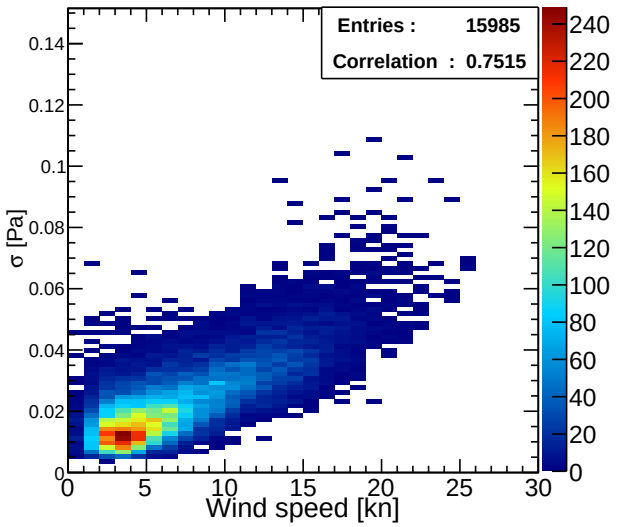

Figure 4.9.: *The correlation between the average wind speed from stations 1 and 4 and ambient noise.*

a continuous stream of data that produce good results. Since station 1 (Cap Cépet) provides the most measurements and also happens to give the best correlation factor, its data will be used for the further analysis. Using the average wind speed of stations 1 and 4 gives a slight increase in the correlation with an value of 0.75 at the loss of 1000 events due to different data timings (see Fig. 4.9). This is not too surprising, because the wind speed is a vector field that expands over the whole earth. The wave height is not determined by the wind velocity in one single location, but by the average in a large area. Considering more points in space obviously yields a better estimated for the real value of the average wind speed.

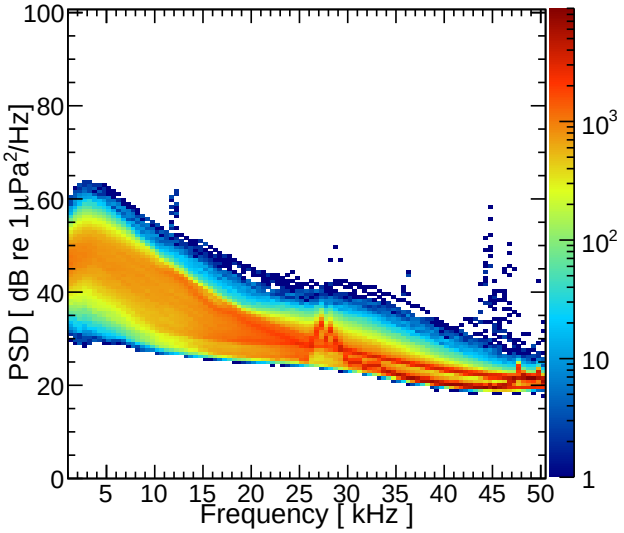

Figure 4.10.: *Power spectral density of the filtered events. The color of each bin marks the number of entries. There are two red lines in the spectra at higher frequencies, because the data of two hydrophones was used in order to cover the whole active time of AMADEUS.*

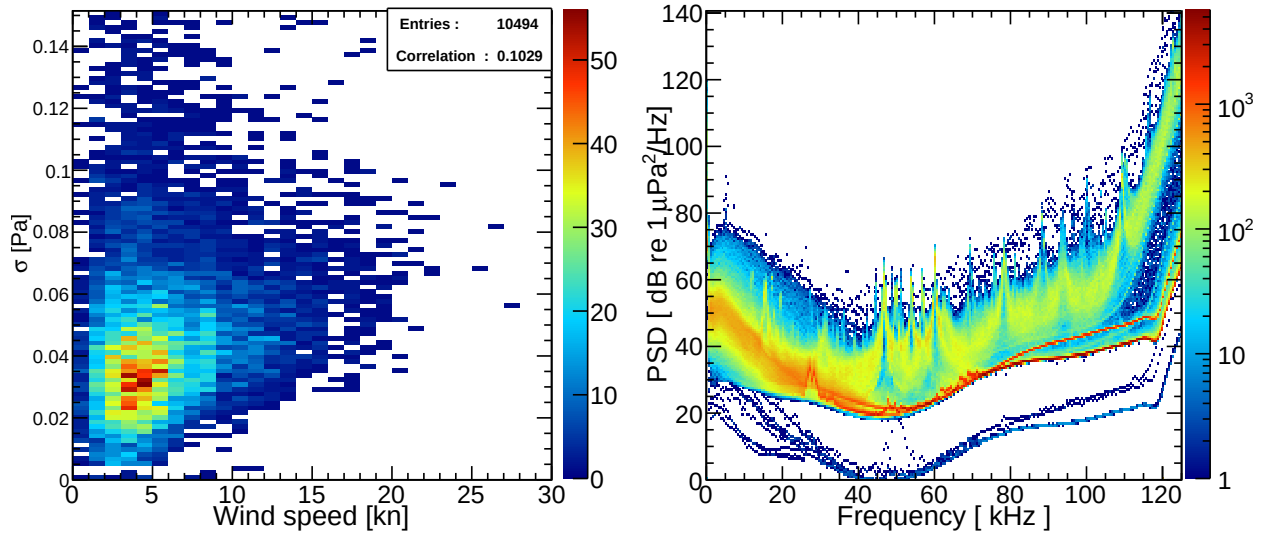

(a) Correlation (b) PSD

Figure 4.11.: *Wind-noise correlation and spectra of the discarded events.*

The histogram in Fig. 4.10 shows the power spectral density of all events in a single plot. Almost every event with a signal has been removed by the filter, but there are still very few events with the pings from the positioning system at approximately 45 kHz. These should not influence the obtained correlation factor by a large margin, since their number is negligible compared to the rest of the events. The two hydrophones do not record the exact same noise, since there is a peak at 25 kHz in the data of sensor 11. This is caused by an acoustic source on the Instrumentation Line, and that behavior can be seen for all hydrophones on that storey. So if one decides to analyze the data of both lines simultaneously, it is impossible to have a pure noise spectrum, but the acoustic power level is quite small and contained in a narrow frequency range, so the effect on the total noise is small. A detailed look at the power spectral density however should not be done with data from the IL, since these signals obviously change the shape of the spectrum. But it can already be concluded, that the spectral power decreases with increasing frequencies as it is predicted by the Knudsen curves. The peak at 5 kHz is not expected, but it is not necessarily a feature of the spectrum. It is likely caused by the non ideal sensor calibration used for the HTI hydrophones (c.f. Sec. 2.3), as this is not seen for the other sensor types. The spectrum of the ambient noise will be discussed in detail in Sec. 4.6.
The analogous plots as Figs. 4.8 and 4.10 for the filtered events are displayed in Fig. 4.11. Wind speed and noise level are almost not correlated. There are also some entries in the correlation plot that seem to be cut erroneously, but they usually contain signals of the positioning system in their spectrum. Also some outliers from data taking tests with reduced gain were removed.

This analysis was repeated for each of the HTI hydrophones, and the resulting correlation factors are shown in Fig. 4.12. The average correlation factor is 0.737(12). A linear function was fitted to the histograms of the wind-noise plots, and the resulting function, with its parameters averaged over all 18 HTI hydrophones, is:

$$f(v) = 0.0051(9)\,\mathrm{Pa} + 0.0023(3)\,\mathrm{Pa\,kn^{-1}} \cdot v \tag{4.3}$$

However, the fits are quite bad, with a reduced χ^2 of 3−6. This might be caused by the inherent noise of the hydrophones, which does not allow the standard deviation to drop below 5 mPa. Therefore it detoriates the linear relationship for wind speeds below 5 kn. The wind-noise correlation plot from Fig. 4.8 is shown together with this function in Fig. 4.12.

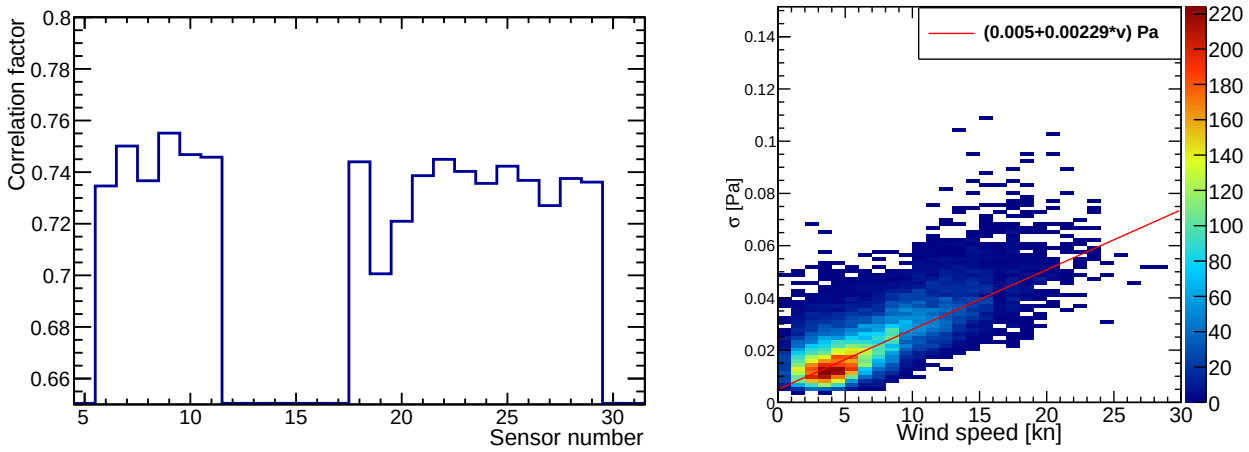

(a) Correlation for all HTI hydrophones

(b) Fitted function

Figure 4.12.: *The wind-noise correlation factor for all HTI hydrophones (sensors 6 to 11 and 18 to 29) is shown in (a), while (b) shows the linear function (Eq. 4.3) derived from fits to the histograms of all HTI hydrophones together with the plot from Fig. 4.8.*

The variation of the ambient noise in different time periods is also quite interesting. It is plausible that the ambient noise level varies with the season, as e.g. the wind phenomena change over the year. That would translate into a seasonally varying background for acoustic particle detection. This means that the sensitivity and the effective detector volume depend on the current month. So, to conduct this study, the recorded data were sorted by the month in which they occurred and are displayed in Fig. 4.13. The values of the standard deviation of the minimum bias samples are put in a two-dimensional histogram, with the abscissa determined by the month in which the sample was recorded, and the ordinance determined by the value of the standard deviation. The average noise level is higher during the winter, and there is also a significant peak during March, which coincides with the maximum strength of the the Sirocco. Additionally the small peak in July and August matches with the occurrence of the summer Mistral. See Section 3.1 for more details. This is an expected result, since the previous chapter has already shown the correlation between wind speed and ambient noise. The weather parameters are depicted in Fig. 4.14 together with the correlation factor of the ambient noise and the wind speed. Since the shape of the curves of correlation factor and wind speed are extremely similar, it is safe to say that higher sustained wind will increase the visibility of the coupling of these two values. The reason for that is quite simple to understand: there is a natural fluctuation in the noise, caused for example by biological sources or shipping noise. If the average wind velocity is low or does not vary much, one will only see the natural fluctuation. But once the wind alters by a big margin, the change in the noise level will be dominated by it. Therefore the correlation factor will be larger, simply because it becomes more apparent. If the wind speed covers a bigger span, then the mean value will increase, because the wind speed has a lower limit at zero knots. That explains why these two curves show a similar behaviour, if the wind is the cause for a major component of the ambient noise in the deep sea. The average sea surface temperature above the detector from 2008–2011 is also shown in that plot. It was generated by the HadISST 1.1 dataset provided by the Hadley centre [30]. The coupling of the wind and the ocean could also depend on the temperature difference at the air/sea interface, but there is no clear evidence for that.

As examined here, the ambient noise definitely varies during a year with the season. This raises the question of whether there are other periodic intervals in which the noise changes. The most apparent periodic event are the days themselves. So the noise data was arranged like in Fig. 4.5,

sorted by the time of the day it was recorded. This is shown in the Fig. 4.15. The first thing that jumps to the eye is the lack of events from 1:00 to 3:00 and 20:00 to 22:00 o'clock. This is caused by the cut that is used to remove the shipping noise (see Fig. 4.5). However the average noise level in these time frames is still 6 mPa above the rest of the day. There is no reason why these times should be special, except for increased shipping activity. Even though the filter should remove the shipping noise, it is not 100 % effective. The average noise level for the rest of the day is stable at about 21 mPa. The correlation factor calculated for the hours during the day has noticeable dips in these two intervals, see Fig. 4.16. If the cut on the rate of change for the noise level is not applied, the correlation in the two named intervals drops to 0.3, while the rest stays at roughly 0.65 to 0.7. Therefore this specific filter seems to work quite well, which confirms the assumption that the noise level changes slowly with the wind speed. The shape of the two curves for the wind speed and the correlation factor now clearly differs, which was not observed in Fig. 4.14. This might be caused by the fact that it takes some time for the wind to agitate the sea. This effect is not seen for binning intervals of a month, but for one hour bins it is noticeable. If the correlation factor is delayed by 2 hours, then the curves look quite similar again. But the broad peak from 6:00 to 21:00 in the correlation factor only resembles the peak in the wind speed from 12:00 to 22:00. However, an accurate interpretation of this behavior is not possible, as shipping noise and wind both cause dips and peaks in the shape of the curve.

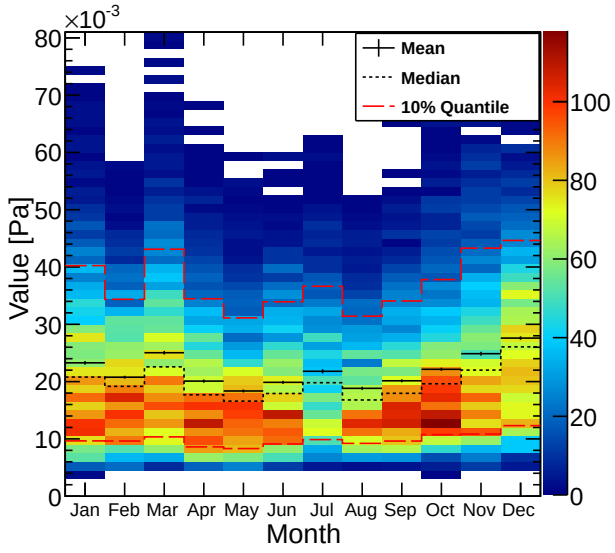

Figure 4.13.: *The recorded ambient noise level during a year and the quantiles of the histograms.*

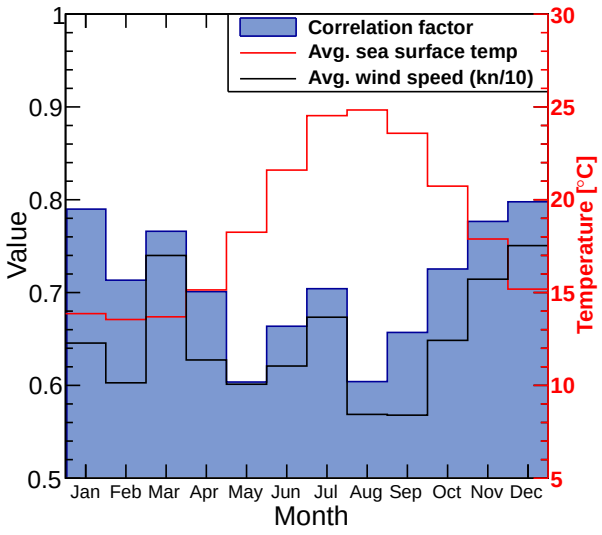

Figure 4.14.: *Monthly variation of the correlation factor in a year. The average wind speed and sea surface temperature are also shown.*

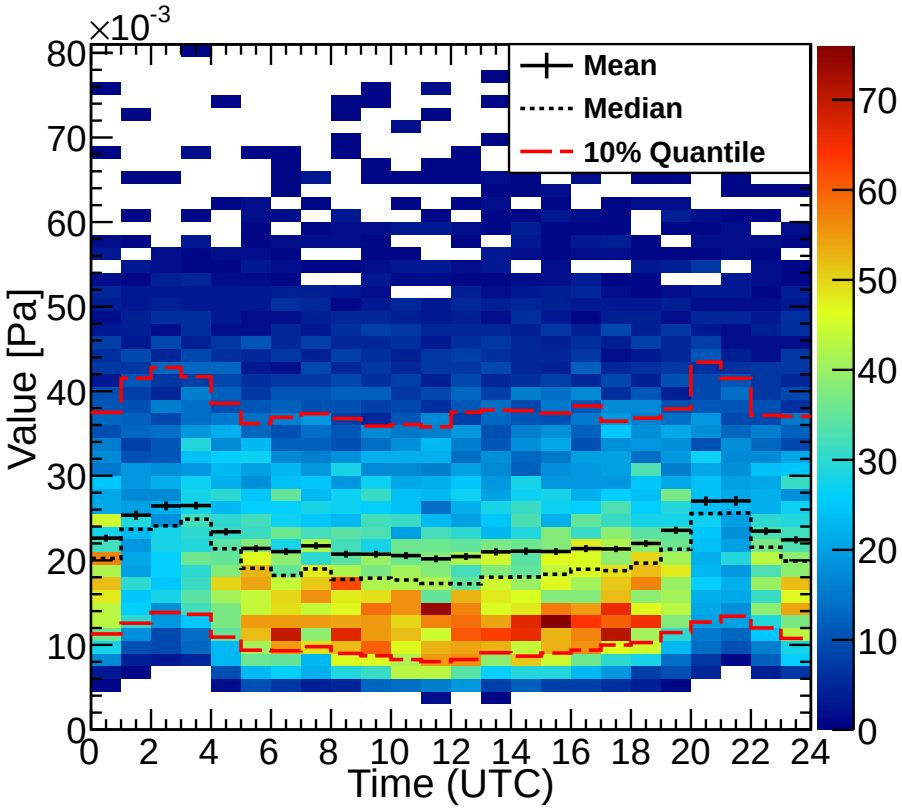

Figure 4.15.: *The ambient noise level during a day. There are less entries from 1:00 to 3:00 and 20:00 to 22:00, since the data was filtered for signals.*

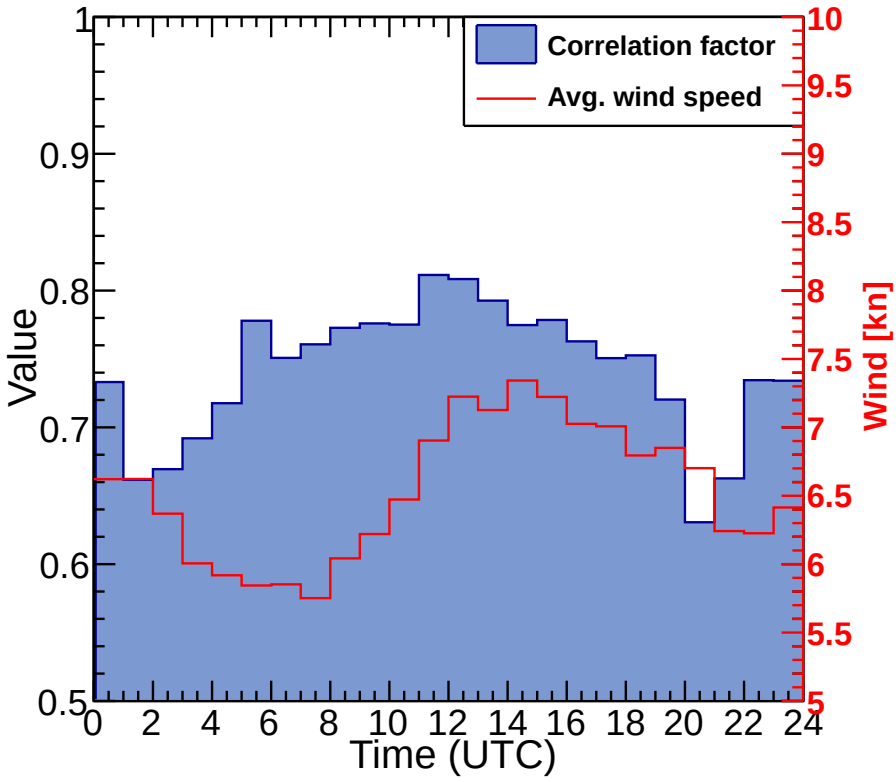

Figure 4.16.: *Variation of the wind-noise correlation factor during a day. The average wind speeds are also shown.*

4.4. Development of the Sensor Sensitivity

Since AMADEUS is an experimental study towards the acoustic detection of neutrinos, it is essential to understand the development of the sensor characteristics during the lifetime of the detector. As an R&D project, it is essential to check if the hydrophones loose a big portion of their sensitivity, especially if they are no longer able to detect the signals produced by neutrinos after some amount of time. Naturally it is impossible to completely prevent the degeneration of the sensors, so the main question is how much the sensitivity is lost during the lifetime of the detector. Another important point is whether the inherent noise remains at the same level, or if it varies over time. In order to find out whether the inherent noise of the system changes, one can look at the minimum bias data. This is based on the assumption that the total sound level in the ocean is constant, at least if the time frame is big enough. Here, a sampling length of 1 year was chosen. The data was acquired in the years 2008–2012. The year 2012 is also included here, because weather data is not needed for this analysis, which wasn't available for 2012.
The lower limit of the distribution of the standard deviation is determined by the inherent noise. This is at least the case for the sensors used in AMADEUS, because inherent noise has the same magnitude like the ambient noise at sea state 0. Therefore it is relatively simple to determine the development of this value, because an increase or decrease of this quantity can be observed directly. Rising inherent noise would also lead to a rising lower limit and the width of the distribution would be reduced, if the sensitivity remains unchanged. If the inherent noise would decrease while the sensitivity stays constant, the exact opposite would happen. The variation in the normalized distributions, with at least 2000 entries per year after the cuts explained in Sec. 4.2 were applied, can be seen in the Fig. 4.17. The data from the HTI hydrophones mounted on Line 12 storey 22 are shown, because this line has the longest active period. However, in 2009 the line was defective, which prevented the data acquisition for the majority of time in that year. This is the reason why the distribution of the standard deviations for the samples from 2009 is not shown there. The number of recorded minimum bias data for 2009 is small, and the sample contains only months with higher averaged wind speeds. Therefore it has low statistics and follows a different distribution, which would lead to false conclusions about the development of the sensors. But for the rest of the graphs a clear trend is visible. The width and the median value of them decreases, while the lower limit remains unchanged. This means that the inherent noise is constant for all these years, while either the sensitivity or the ambient noise level decreases. The development for these quantities is also shown in Fig. 4.18. The values displayed there represent the relative changes compared to 2008 averaged over all hydrophones mounted on a storey. The width in this plots is the difference between the .75 and the .25 quantile, which is more robust to outliers than the standard deviation. The median of the distributions for the hydrophones on Line 12 storey 22 has dropped to 0.76(3) of its original value in 2008, or a decrease of 6.3(7)% per year. The width was reduced to 0.81(3) or 5.1(7)% per year. The inherent noise didn't change during this period, because the lower limit of the distribution stayed at the same value. This corresponds to a sensitivity loss of 2.4 dB, which can also be observed in the recorded spectra in Fig. 4.20. The LTIs however show no sign of an aging process, neither in the sensitivity nor in the inherent noise, see Figs. 4.19and 4.20. The sensors on the IL varied less than 2% during the active time, and the ones from Line 12 first show an increase of both values by 10% in 2009, which rapidly drops back to the value of 2008. This is likely an effect of the reduced active time in that year, because the data was only taken in months with higher averaged wind speeds. The distributions for the sensors on the IL for the years 2009 and 2010 also pass a Kolmogorov-Smirnov test at a 5% significance, which supports that claim. Hence no clear trend is visible for the self-made hydrophones. However, the LTIs have a higher failure rate than the commercial hydrophones,

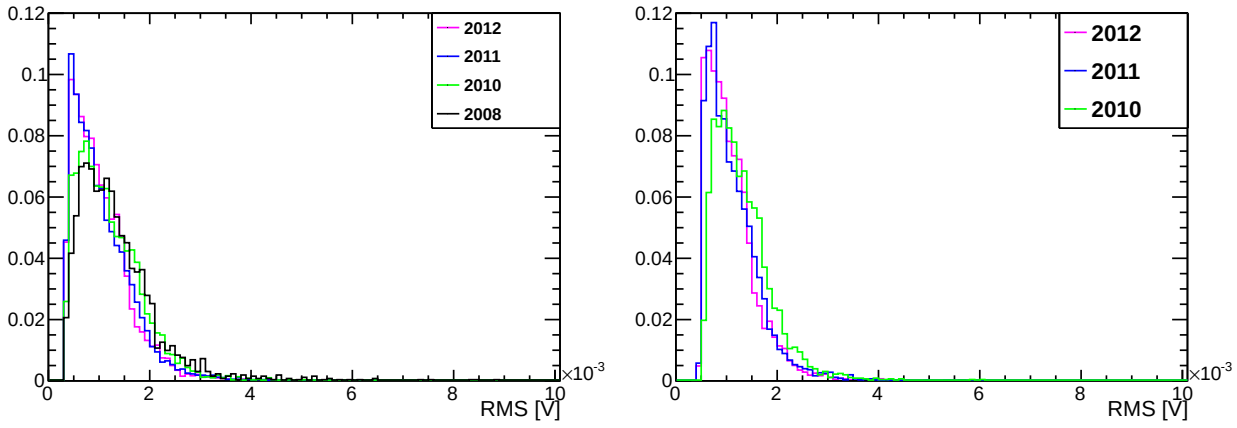

(a) Sensor 18

(b) Sensor 19

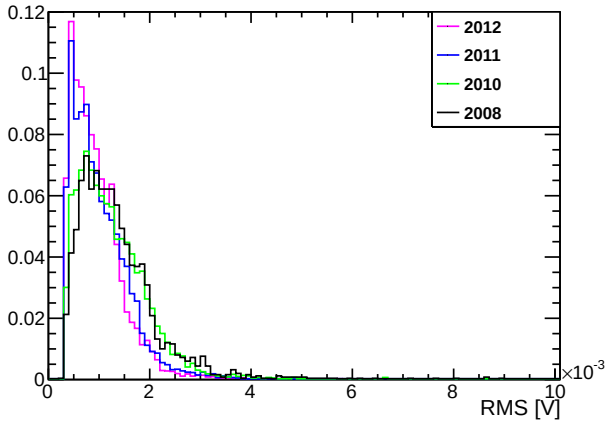

(c) Sensor 20

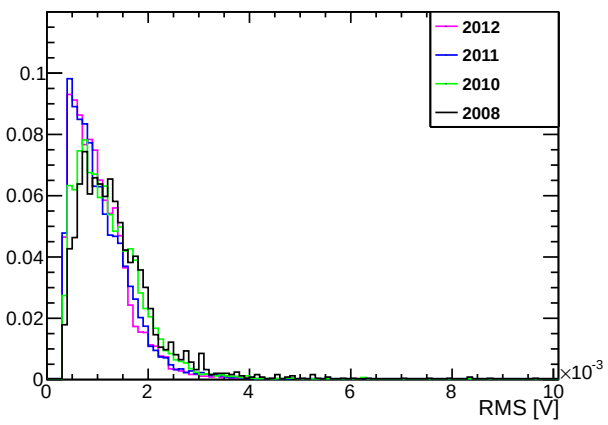

(d) Sensor 21

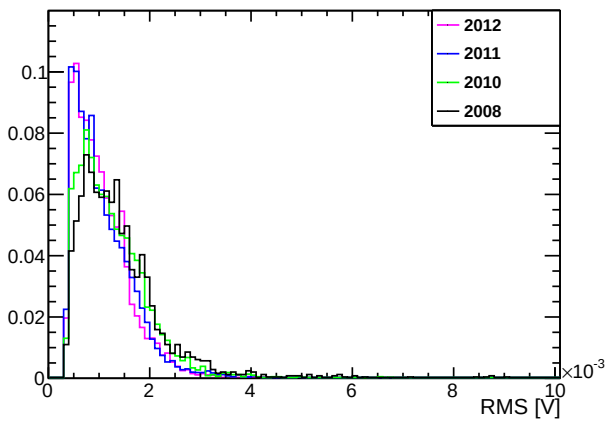

(e) Sensor 22

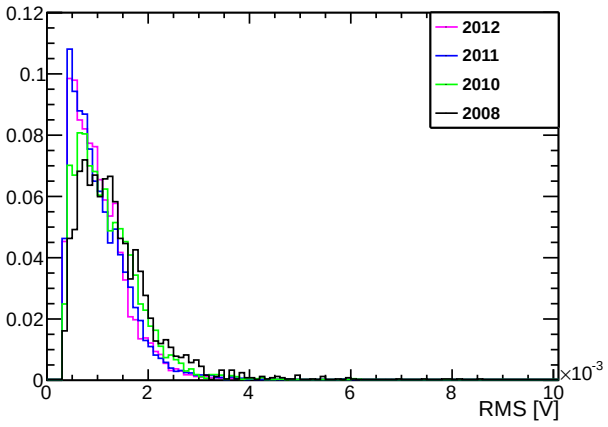

(f) Sensor 23

Figure 4.17.: *The distribution of the recorded noise of the sensors mounted on storey 22 on Line 12 during its active time for all years with more than 2000 recorded events. All of these hydrophones were made by HTI and the events are also filtered for signals, applying the same cuts as discussed in Sec. 4.2. Sensor 20 was replaced after the recovery in 2009.*

with a total of four defective hydrophones.
The AMs cannot be compared with the hydrophones, because the sensors were reglued to the glass spheres during the maintenance of Line 12 in 2009. Consequently, the development of the sensor is mostly caused by this intervention, and not by natural effects. However, the value of the width for the AMs has only varied by 4(2)% per year since the maintenance, which is still

in agreement with no change. The median shows a larger variance with 7.5(10)% per year, but for both of them there is no clear direction.
See Appendix A.1 for a full table of the evolution of noise width and median for the individual sensors. In conclusion, the inherent noise of the system stays constant for all sensors, but the sensitivity of the HTIs is decreasing.

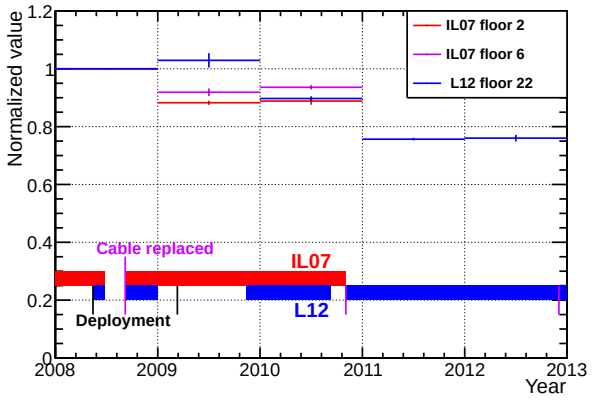

(a) HTI median

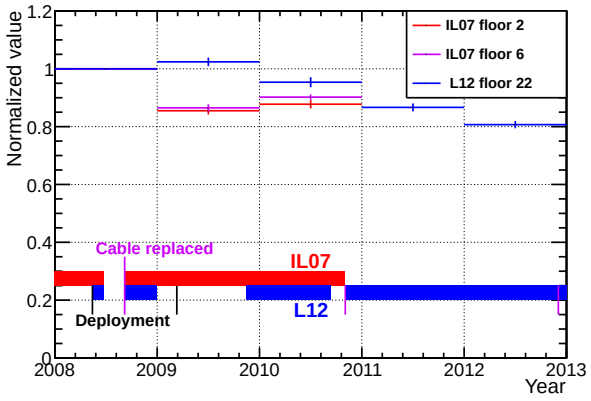

(b) HTI width

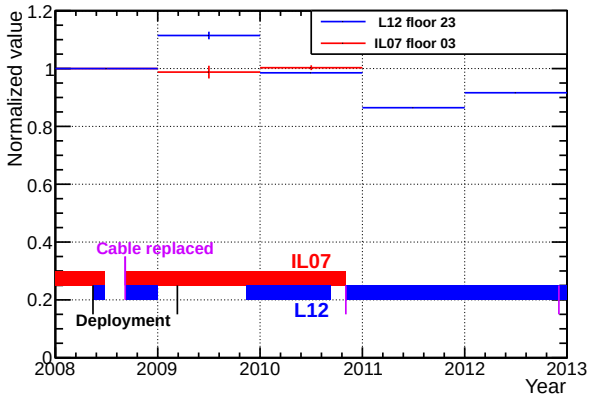

(c) LTI median

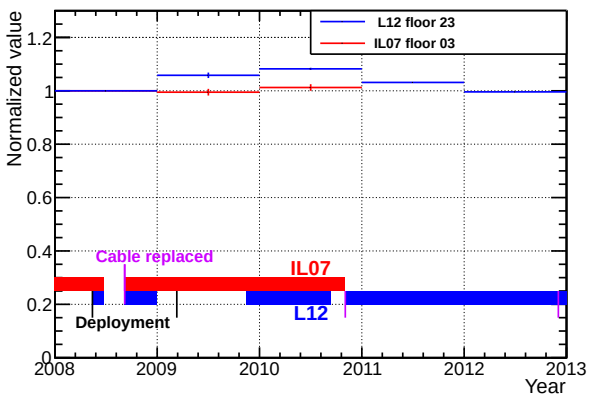

(d) LTI width

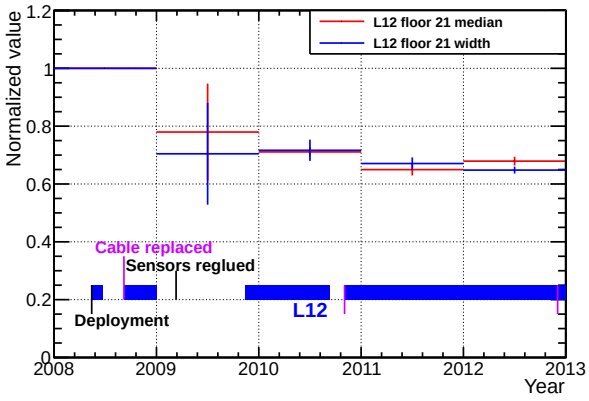

(e) Acoustic modules

Figure 4.18.: *The development of the median and width of the recorded noise distributions by the sensors used in AMADEUS. The values are averaged over all hydrophones on each storey, while defective or replaced sensors were excluded. The filled bar marks the intervals when the lines were available for data acquisition.*

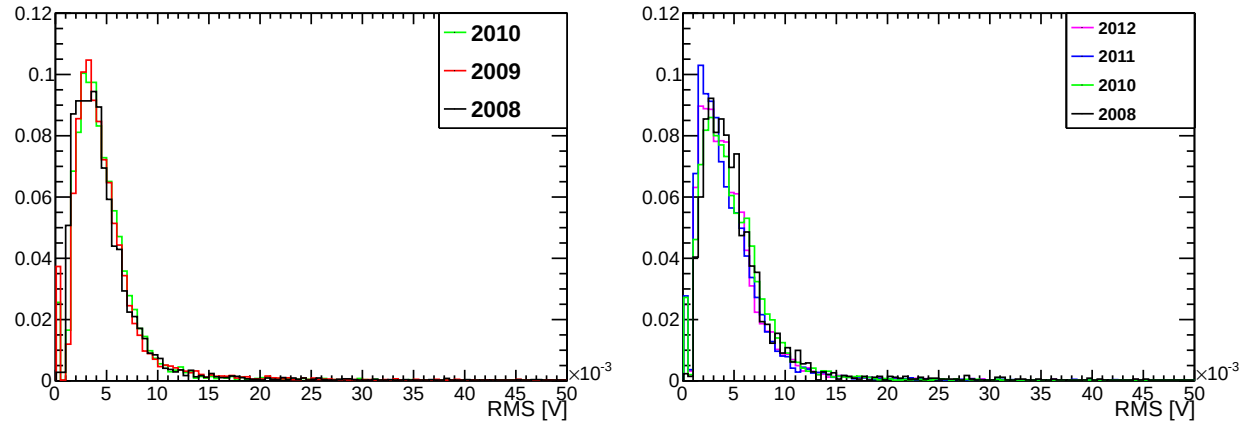

(a) Sensor 1(LTI) (b) Sensor 30(LTI)

Figure 4.19.: *Two examples for the normalized distribution of the standard deviation for the minimum bias data for LTI hydrophones. No significant change in the shape of the distributions is observed.*

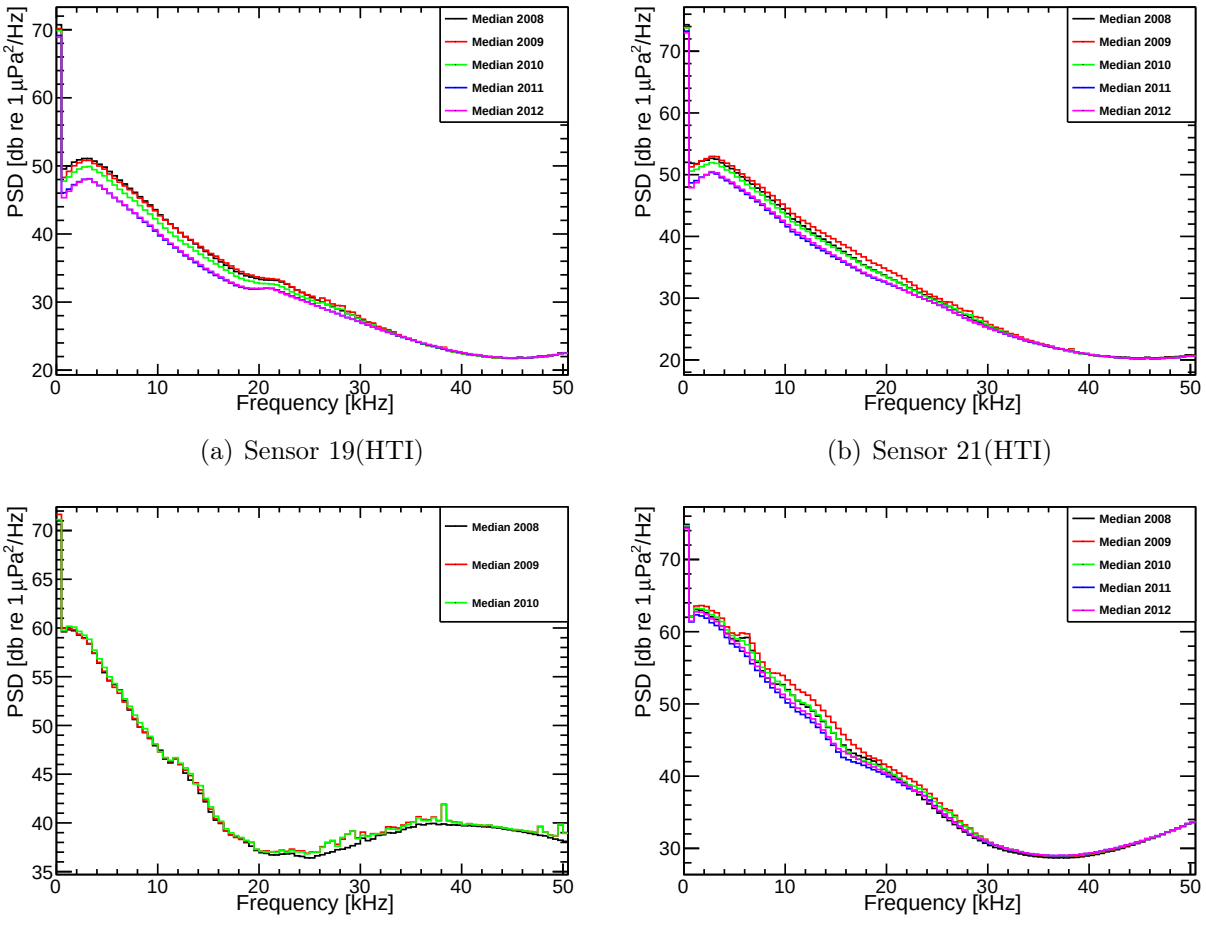

(a) Sensor 19(HTI) (b) Sensor 21(HTI)

(c) Sensor 1(LTI) (d) Sensor 30(LTI)

Figure 4.20.: *The development of the recorded noise spectra for each year. The median of the spectra for four exemplary hydrophones is shown, which reveals a clear trend for the HTIs, but not for the LTIs.*

4.4.1. Aging process

The process behind the aging can probably be explained partly by the rapid pressure variation during the maintenance of a line. When the sensor has been submerged for a long time in such a depth, then the sea water will have penetrated the material of the detectors. The underlying

mechanism causing the penetration is diffusion, which cannot be prevented. But there is also the possibility that small hollows near the surface of the material are present. They can be caused by chemical reactions between the sea water and the material of the sensors, or they already existed when the line was deployed. When the line is recovered, the pressure is reduced from about 220 bar to the normal pressure of the atmosphere at the sea level. If any of these hollow spaces in the sensor are filled with water, then the excess pressure might cause damage to the material when there is no other way to equalize the pressure. For example, the LTI hydrophones can develop cracks during these pressure cycles, while the HTI are not affected, at least not visible to the eye. This might be consequence of the different rigidity of the different materials coating the piezoelectric elements used in those sensor types.
However, the line recovery and redeployment is probably not the only reason for a loss in sensitivity, since the sea water affects many materials negatively. For example, the polyurethane used in the hydrophones is affected [31]. The PU is slowly destroyed by the aggressive components in sea water, which induce chemical reactions with the plastic. There are also micro-organisms that can settle on the surface of the sensors, and their metabolic products can also harm the material. Additionally, the acoustic transmissivity will be changed with diffused water, which further influences the sensor characteristics.

4.5. Determination of the inherent noise of the sensors

4.5.1. Theoretical considerations

The spectrum of the constant noise background, caused by the inherent noise of the detector (e.g. electronic noise or shot noise) should be subtracted for the analysis of the ambient noise spectrum. An inherent noise spectrum was measured in the laboratory prior to installation. This noise spectrum is a good estimate for the inherent noise up to 40 kHz, see Fig. 4.21. It is dominated by electronics noise in the laboratory above 40 kHz, however. The deep sea environment is free of electronics noise.

Therefore, an estimate for the inherent noise of the detector has to be determined from the data recorded in the deep sea. But this causes another problem, because it is not possible to get a pure inherent noise sample, as there is always a contribution of the ambient noise. However, it should be possible to get an estimation for the inherent noise from the distribution of the recorded spectra. One method is the lower $3\,\sigma$ quantile of the spectra, but this overestimates the inherent noise when the sensor is fully sensitive to the ambient noise, and if the inherent noise dominates over ambient noise. In the following, a better way to determine the inherent noise level for each frequency is presented.
The recorded sound pressure level x in dB at a given frequency f is composed of the true ambient noise y and the noise of the detector c. If one assumes that they add up incoherently, this leads to the following formula in dB:

$$x = 10 \cdot \log_{10}\left(10^{y/10} + 10^{c/10}\right) \quad . \tag{4.4}$$

Assuming that c is only one constant value, the probability $P'(x)$ to measure a spectrum with the power level x should be the same as the probability to measure y:

$$P'(x) = P_{\mathrm{NL}}(y) \tag{4.5}$$

$$= P_{\mathrm{NL}}(\alpha(x,c)) \cdot \frac{\partial \alpha(x,c)}{\partial x} \tag{4.6}$$

While α is derived from 4.4:

$$\alpha\left(x,c\right) = 10 \cdot \log_{10}\left(10^{x/10} - 10^{c/10}\right) \tag{4.7}$$

$$\frac{\partial\alpha(x,c)}{\partial x} = \frac{10^{x/10}}{10^{x/10} - 10^{c/10}} \tag{4.8}$$

The term $\frac{\partial\alpha}{\partial x}$ is required to keep the probability density normalized to 1. However, the assumption that the c is constant is flawed, because the inherent noise background is not a single value, but distributed following a Gauss distribution. This can be seen if one takes a look at the shape of the recorded noise spectra at high frequencies above 80 kHz, see Fig. 4.22. The recorded noise power level at 97 kHz is filled into a histogram and a Gaussian is fitted to the normalized distribution. For these frequencies, the hydrophones are sensitive to transients only, which have been removed by the cuts that were applied previously. Since the noise of the detector c cannot be expressed as a single value, it is necessary to consider all possible combinations of c and y, that cause a recorded signal x. This is done by multiplying the probability $g(c)$ to encounter a certain self noise c to P'. This expression has to be integrated over c from $-\infty$ to x in order to take all values into account that can contribute. The upper limit is x, because the noise level cannot be reduced if one adds multiple noise sources incoherently.

$$P\left(x\right) = \int_{-\infty}^{x} P_{\mathrm{NL}}\left(\alpha(x,c)\right) \cdot g(c) \cdot \frac{\partial\alpha(x,c)}{\partial x}\,\mathrm{d}c \tag{4.9}$$

While Equation 4.6 keeps all the information of both distributions, Eq. 4.9 does not. A single event is mapped to a probability distribution, and therefore this formula only makes sense in the context of thousands of measurements. Also, the information for the shape of P_{NL} is lost if the mean value of the inherent noise surpasses the one of the ambient noise. Then the only thing that matters for the shape of $P\left(x\right)$ is $g(c)$, while P_{NL} causes a tail to higher values. If there is difference of more than 5 dB between the mean values, this effect becomes dominant.

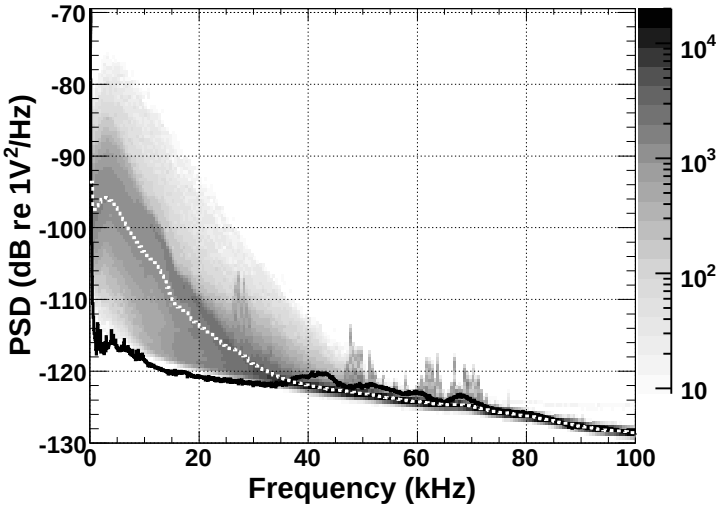

Figure 4.21.: *Power spectral density (PSD) of the ambient noise recorded with one HTI sensor on the topmost storey of the IL. The voltage used is the calibrated input voltage of the AcouADC board. Shown in shades of gray is the occurrence rate in arbitrary units, where dark colors indicate higher rates. Shown as a white dotted line is the median value of the in-situ PSD and as a black solid line the noise level recorded in the laboratory prior to deployment. Adapted from [10]*

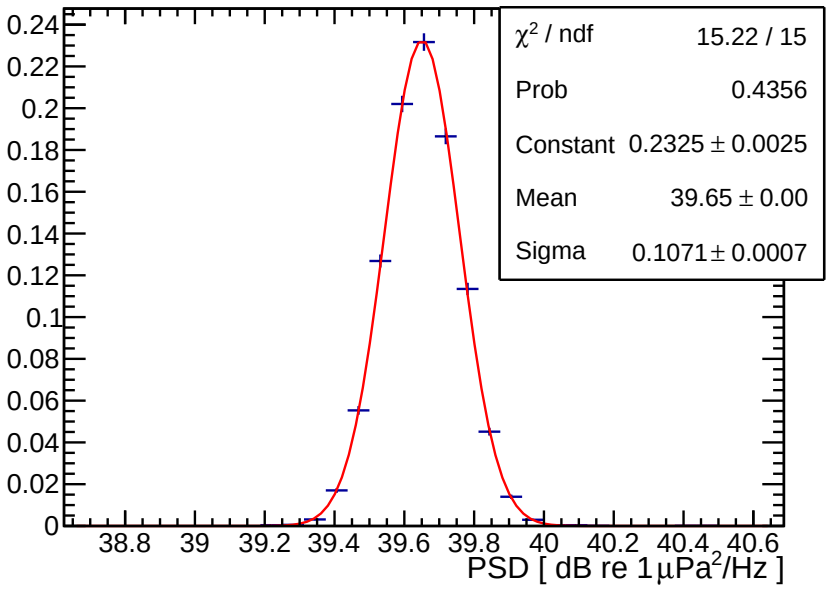

Figure 4.22.: *The distribution of the spectral power level of the filtered minimum bias data at* 97 kHz. *A Gaussian distribution has been fitted to the data.*

The integral can be evaluated numerically, and a C++-routine has been implemented to do so. An example for the behavior of the distribution can be seen in Fig. 4.23. A Monte Carlo test was also performed, by using Eq. 4.4 to generate a histogram of events from known distributions $g(c)$ and $P_{\mathrm{NL}}(y)$. The corresponding function for $P(x)$ can be fitted to that histogram, which reproduces the original values (within the errors of the fit) and gives a small $\chi^2/\mathrm{n.d.f.} \approx 1$. As an example, consider $g(c)$ as normalized Gaussian distribution with the values of $\overline{x}_g = 24.0428$ and $\sigma_g = 0.2$. The ambient noise distribution $P_{\mathrm{NL}}(y)$ is also assumed as Gaussian distribution with $\overline{x}_{NL} = 16.7371$ and $\sigma_{NL} = 6.5908$. The histogram is generated with 10^5 Monte Carlo points and $P(x)$ is fitted with a log-likelihood method in the range 23.5 to 34. The reduced χ^2 is 1.05 and the resulting fit parameters are $\overline{x}_g = 24.048(4)$, $\sigma_g = 0.205(2)$, $\overline{x}_{NL} = 16.67(4)$ and $\sigma_{NL} = 6.60(4)$. The test has been performed several times and always produces a similar close result. This is good indication that the formulas are correct and that the implementation works.

4.5.2. Fitting the data

In order to get the constant noise background, the formula for $P(x)$ can be fitted to the measured data, if one assumes an analytical function for $g(c)$ and $P_{\mathrm{NL}}(y)$. The scatter plot of the power spectral density is divided in 500 Hz wide slices. For each slice a histogram of the spectrum levels is created with variable bin sizes matched to the spread of the data, which forms the distribution $P(x)$. As function for $g(c)$ a Gaussian distribution is assumed, as it is seen for high frequencies (see Fig. 4.22). The width stays the same for them, so this parameter is determined by Gaussian fits to be $\sigma_g = 0.11$ and fixed for the rest of the analysis. Since $g(c)$ is a probability distribution, the amplitude is also defined by the width, in order to keep the integral over $g(c)$ normalized to 1. So the only parameter that has to be matched with the data is its mean value $\bar{x}_g$.
The function for the ambient noise $P_{\mathrm{NL}}(y)$ cannot be determined that easily. But, as discussed in the previous section, the exact shape is not so important, since information is lost in the convolution once the constant noise background has the same magnitude like $P_{\mathrm{NL}}(y)$. This is, however, the exact interval, where it is crucial to know the background level. The magnitude of

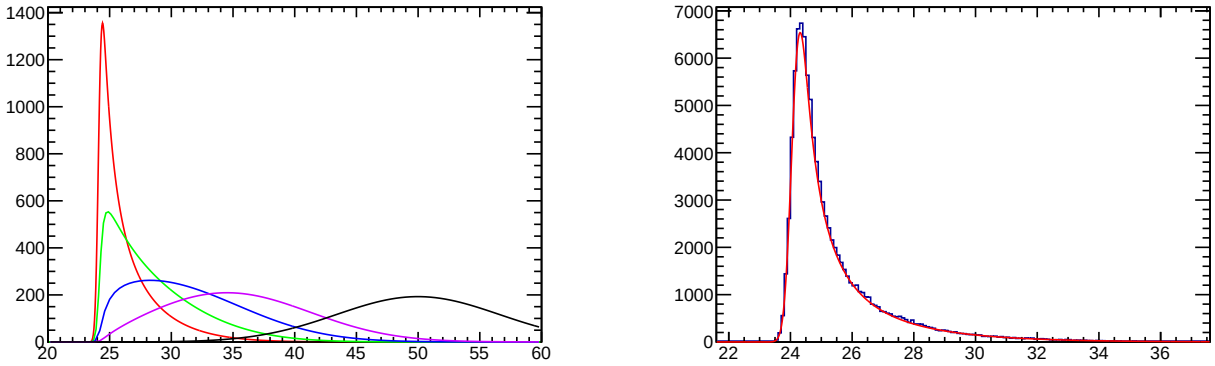

(a) Examples (b) Monte Carlo Test

Figure 4.23.: *An example for the behaviour of $P(x)$ (Eq. 4.9) for a Gaussian noise distribution P_{NL} with a fixed width $\sigma = 6.6$ and amplitude $a = 192$, but a varying mean value $\bar{x} = \{20, 25, 30, 35, 50\}$ is shown in (a). The constant noise part $g(c)$ was assumed to follow a normalized Gaussian distribution with the fixed values $\bar{x}_g = 24$ and $\sigma_g = 0.2$. The panel (b) shows a Monte Carlo test using Eq. 4.4 for 10^5 samples and $P(x)$ for the corresponding distribution. The reduced χ^2 is* 1.05.

the inherent noise is the searched quantity here, and not the exact shape of the ambient noise distribution. As long as $P_{\mathrm{NL}}(y)$ is a continuous distribution with a peak, it can reproduce the tail to higher intensities. Therefore $P_{\mathrm{NL}}(y)$ was also assumed to be a Gaussian, but all three parameters were fitted. Some examples for the fits are shown in Fig. 4.24 and the resulting inherent noise spectrum is shown in Fig. 4.25. The inherent noise surpasses the lower $3\,\sigma$ quantile at 25 kHz for the HTI hydrophones, which defines the upper frequency where the hydrophones are fully sensitive to the ambient noise. Above 30 kHz the ambient noise level is below the inherent noise even for higher sea states. At 50 kHz even the tails to higher sound levels start to disappear and the only thing left is the inherent detector noise. This means that the analysis of the spectrum should only be conducted below 30 kHz.

4.5.3. Deconvolution of the spectra

The inherent noise obtained by the fits can now be used to deconvolve the power spectral density. This can be realized with the inverse transformation of Eq. 4.9. The derivation of the inverse transformation uses the same steps as described above, while only two things differ: the formula $\alpha(x, c)$ has to be replaced with its inverse $\beta(y, c)$ and the limits for the integration change, as the function β already guarantees that only values that are physically allowed to contribute to $P_{\mathrm{NL}}(y)$ are considered.

$$P_{\mathrm{NL}}(y) = \int_{-\infty}^{\infty} P_x(\beta(y,c)) \cdot g(c) \cdot \frac{\partial \beta(y,c)}{\partial y}\,\mathrm{d}c \tag{4.10}$$

$$\beta(y,c) = 10 \cdot \log_{10}\left(10^{y/10} + 10^{c/10}\right) \tag{4.11}$$

For the deconvolution the inherent noise obtained by the fit for $g(c)$ is used, while $P(x)$ is the measured data. The result of this deconvolution is shown in Fig. 4.26. The calculated distribution exhibits a band of constant width from 5 kHz to 30 kHz, while the spread of the spectra shown in e.g. Fig. 4.10 becomes smaller with increasing frequencies. This proves that the the inherent noise of the hydrophones forms a lower limit for the recorded sound pressure level. Therefore the AMADEUS-setup cannot measure neutrino signals with the best possible signal to noise ratio, as the total noise of the sensors could be reduced further. It is theoretically

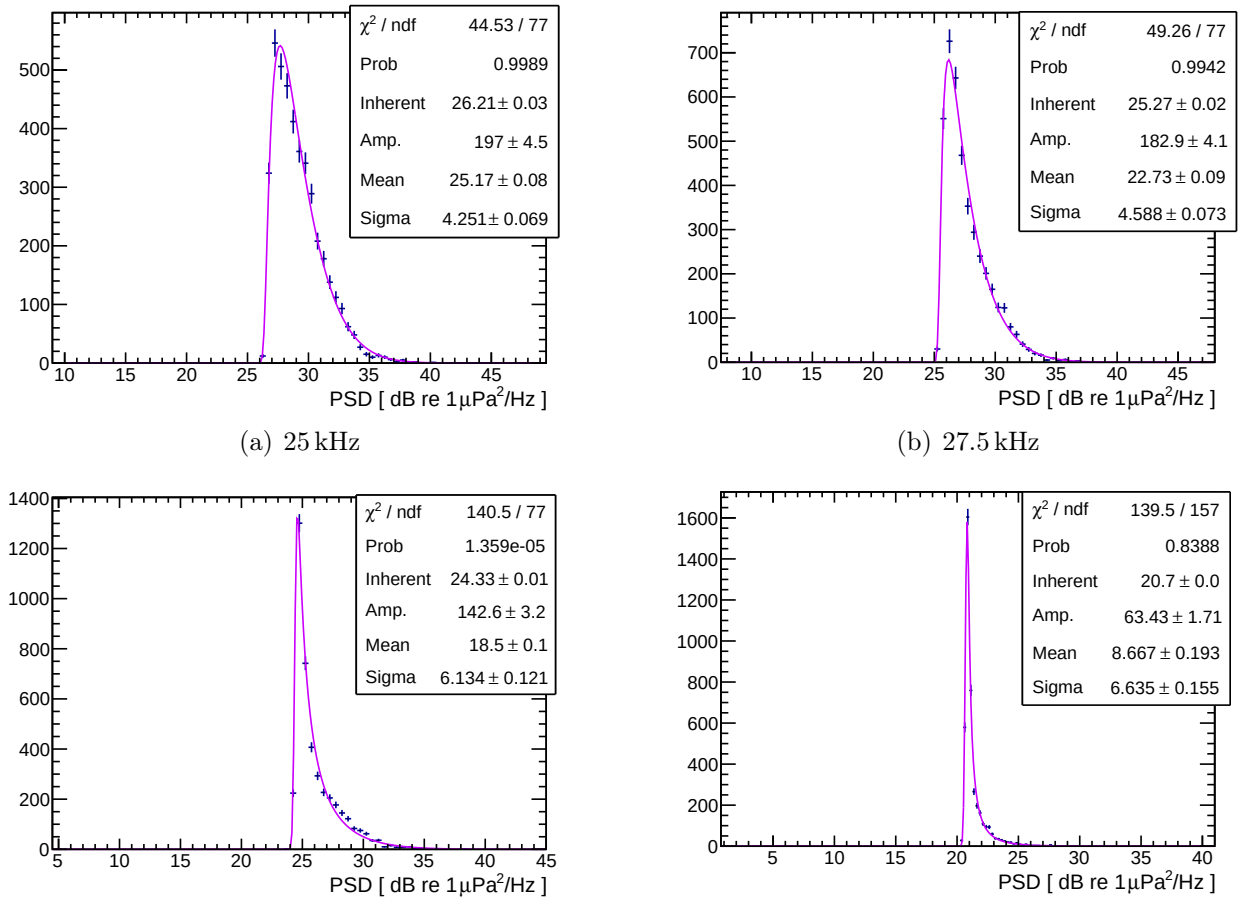

(a) 25 kHz (b) 27.5 kHz

(c) 30 kHz (d) 40 kHz

Figure 4.24.: *Some examples for the fit of $P(x)$ to the distribution of the recorded power spectral density by sensor 21.*

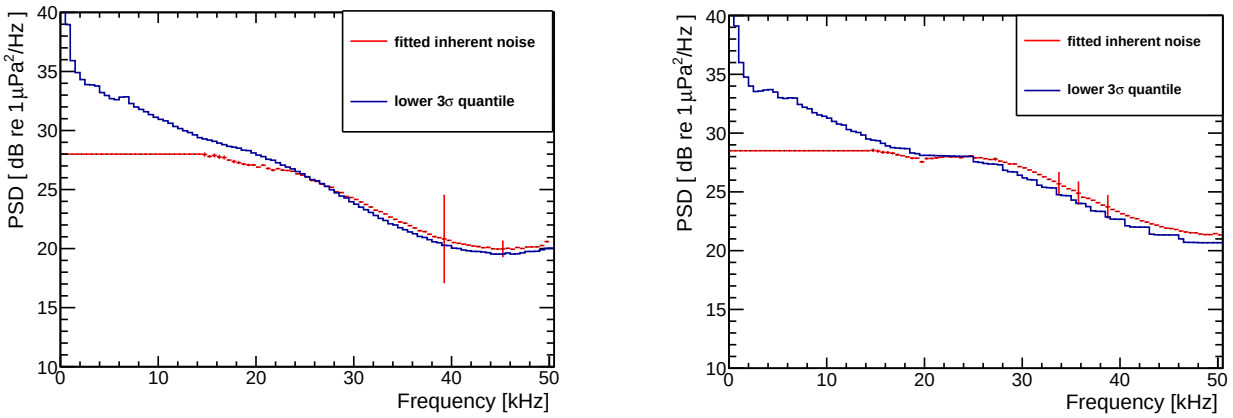

(a) Sensor 21 (b) Sensor 23

Figure 4.25.: *The resulting values for the inherent noise of sensor 21 and 23. The fits get worse when the shape of the ambient noise distribution begins to matter below* 20 kHz*. Therefore the value of the last fitted frequency at* 15 kHz *was used for all smaller frequencies. The lower* $3\,\sigma$ *quantile of recorded spectra is also shown for comparison.*

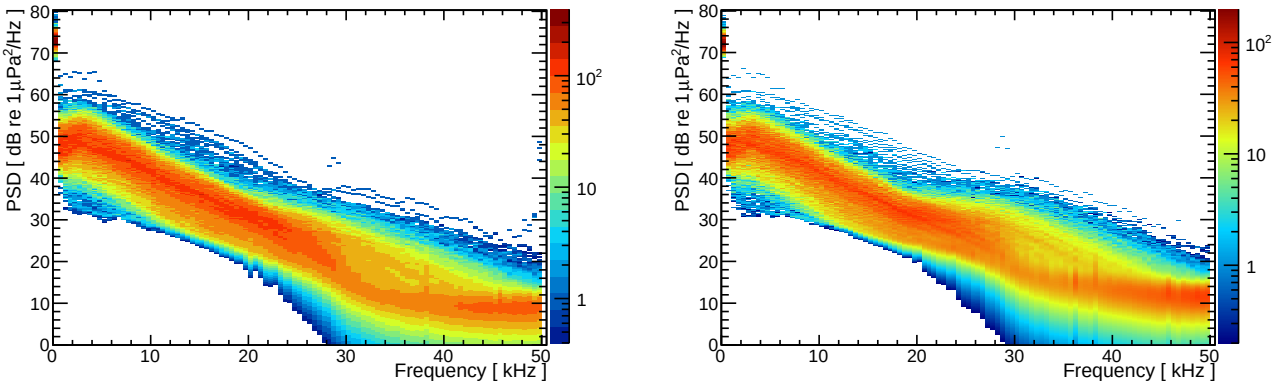

(a) Sensor 21 (b) Sensor 23

Figure 4.26.: *The deconvoluted power spectral density of the recorded minimum bias data from two sensors. The width of the distribution stays constant below* 25 kHz*, contrary to the spectra in Fig. 4.29. The deconvoluted spectrum is reliable up to* 30 kHz*, as too much information about the ambient noise is lost for higher frequencies.*

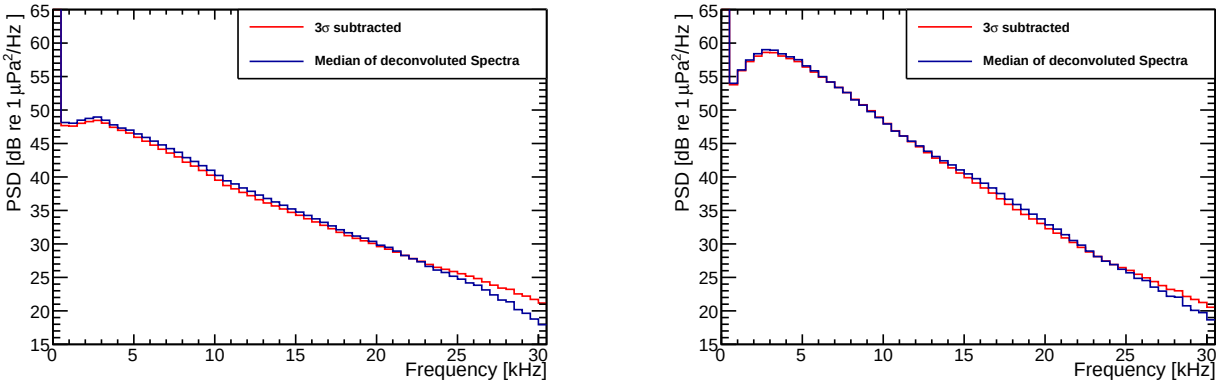

(a) Sea state 1 (b) Sea state 4

Figure 4.27.: *Comparison between the* $3\,\sigma$ *noise estimate and the deconvolution. The median of the spectra for both methods is shown for two sea states.*

possible to create a detector that is sensitive to the ambient noise in the whole relevant frequency range. That would be the optimal case for acoustic particle detection, as the ambient noise cannot be modified, while the inherent detector noise can be optimized.
Another method for the subtraction of the inherent noise is simply subtracting the lower $3\,\sigma$ quantile of the distribution of all spectra. This is a really fast procedure compared to the deconvolution, because no fits have to be made and no numeric integrals have to be evaluated. The value without the electronic background y is computed from the measured spectrum x and the quantile σ_3 in the following way:

$$y = 10 \cdot \log_{10}\left(10^{x/10} - 10^{\sigma_3/10}\right) \quad . \tag{4.12}$$

The median spectrum for both methods are compared in Fig. 4.27. The difference in the relevant frequency range below 30 kHz is less than 1 dB, and only above 27 kHz the gap increases to a maximum of 1 dB. So both methods seem to work fine, but as the $3\,\sigma$ subtraction is a commonly used variant, and mainly due to its short computation time, this method will be used in the further analysis.

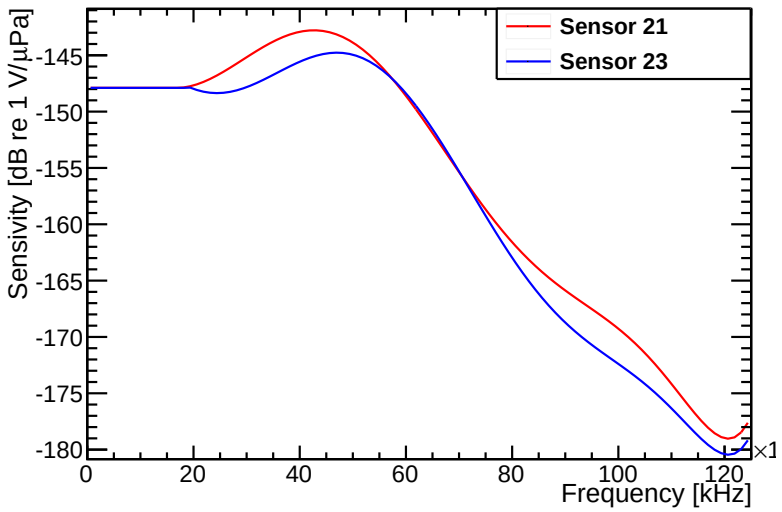

Figure 4.28.: *Two examples for the calibration used for the hydrophones (both from HTI). The functions are piecewise defined, and they are not differentiable at* 18 kHz*, see [6].*

4.6. Ambient noise spectra

Ambient noise spectra are required e.g. for simulations of acoustic particle detection in the deep sea, underwater communication or SONAR development. The power spectral density of the minimum bias data is generated by performing a Fourier transformation on the recorded sound file. Afterwards the calibration, as measured in the laboratory, is applied to the spectrum. Examples for the calibration function of two commercial hydrophones are displayed in Fig. 4.28. This causes an additional uncertainty to the data, because the calibration measured in the laboratory does not necessarily reflect the conditions in the deep sea. There are some sources or electric fields coupling in to the measurements, which cannot be prevented. Also the environmental conditions differ obviously, since the pressure in the laboratory is 1 bar while it is approximately 230 bar at the ANTARES site in 2300 m depth. Additionally the salinity and the acidity of the sea water might have an influence on the response of the hydrophone. The characteristics of the piezo also change in the deep sea compared to the laboratory. There is an uncertainty of ±2 dB in the calibration and anything that varies with depth adds to that uncertainty. Calibrating the hydrophones in the deep sea would yield a more accurate result. However, in situ calibration is not easy: as you have to have a strong, stable emitter (several 100 Pa if operated on the surface). If you include it to the detector it is also pressurized and you do not know its emission strength. At the time of writing, a calibration source is installed at the site which might help.

In order to keep different noise spectra comparable to each other, only the data recorded with commercial hydrophones is used. They show less variation in the response function than the self-made hydrophones and they don't deform the spectrum like the acoustic modules do due to the coupling of the piezoelectric elements to the glass sphere. There are three different storeys with the HTI hydrophones, storey 2 and 6 on the Instrumentation Line and storey 22 on Line 12. Additional devices are mounted on the Instrumentation Line that emit sound in certain frequency ranges. While it doesn't influence the total noise power level much, it poses a problem if one wants to examine the ambient noise spectrum. Since there is a storey available without the disturbing noise or at least with a highly attenuated one, it is the logical choice to use this one. Therefore the hydrophones on storey 22 were selected for the following analysis. The storey consists of 6 hydrophones pointing downwards, see Sec. 2.3. In order to get the maximum amount of data and to reduce the effects of the characteristics of a single hydrophone, all 6 sensors are used for this analysis. The dataset analyzed here is again reduced

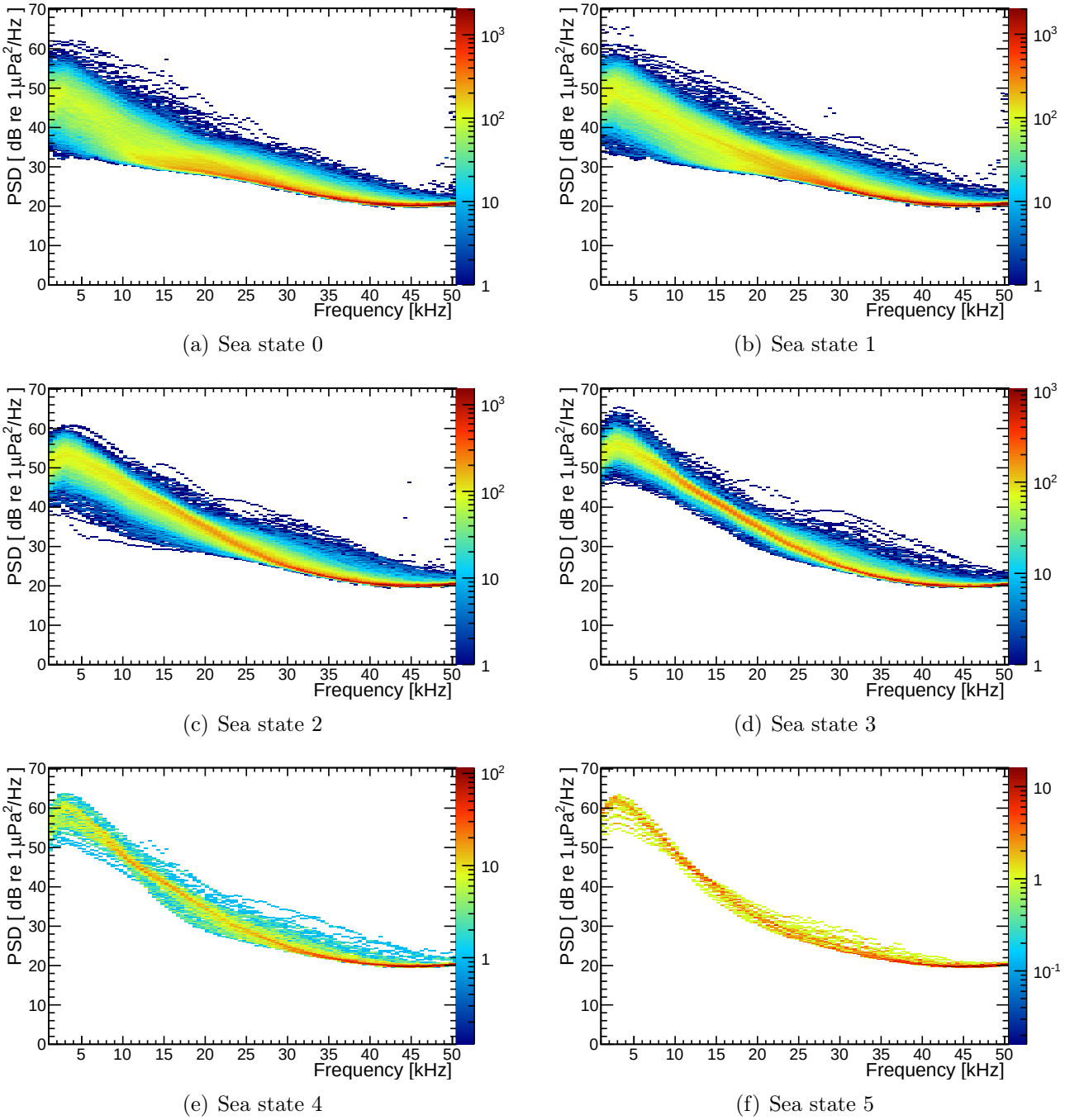

(a) Sea state 0

(b) Sea state 1

(c) Sea state 2

(d) Sea state 3

(e) Sea state 4

(f) Sea state 5

Figure 4.29.: *The measured ambient noise spectra for sensor 21. The data has been filtered for transient signals using the cuts discussed in chapter 4.2.*

to the years 2008–2011, because weather data is required to determine the sea state. For the comparison of the power spectral density with the Knudsen curves and for the study of their variation with the wind speed, the spectra are sorted by the sea state when they were recorded (see Tab. 3.2 for the assignment of wind speed to the sea state). The data from weather station 1 (Cap Cépet) is used to derive the sea state. A scatter plot of the power spectral densities recorded with sensor 21 for each sea state is shown in Fig. 4.29. The distributions of the PSDs can be used for example to calculate their average values or quantiles. Looking at these spectra in the whole frequency range, a steep rise in power level above 50 kHz is observed. This is an effect of the calibration that is only valid in the range 10 kHz to 50 kHz. Additionally the spectra contain the inherent noise of the hydrophones and electronic devices, which changes the behavior above 25 kHz, and it is removed as discussed in the previous section. The lower

$3\,\sigma$ quantile is used as estimate for this background and subtracted from the median of the spectra using Eq. 4.12. The resulting spectra for each sea state averaged over all hydrophones on storey 22 are shown in Fig. 4.30.

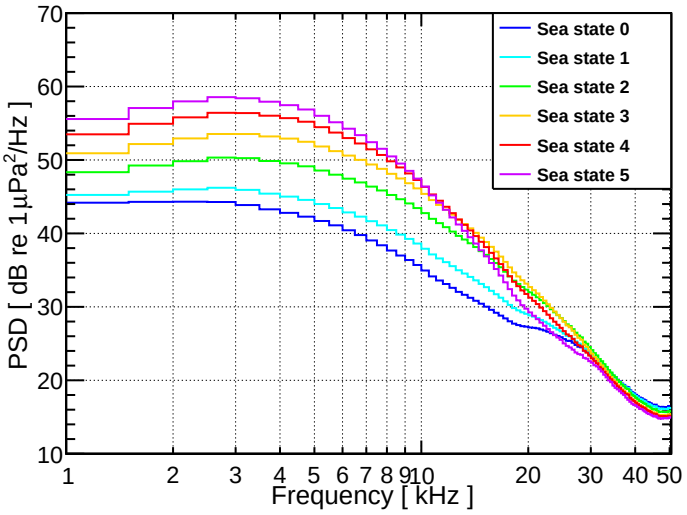

Figure 4.30.: *Measured ambient noise power spectral density for different sea states averaged over storey 22. The hydrophone calibration is used to get the noise level in* Pa. *The* $3\,\sigma$ *quantile has been subtracted to account for the inherent detector noise. See Tab. 3.2 for the wind speeds corresponding to each sea state.*

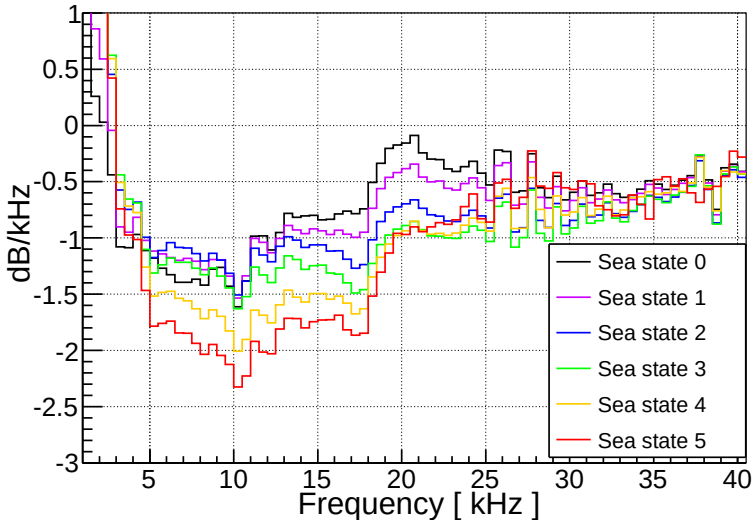

Figure 4.31.: *The first derivative of the measured ambient noise spectra for different sea states from Fig. 4.30. See Equation 4.13 for the computation algorithm. The sharp edge at* 18 kHz *is caused by the calibration, because it consists of two functions, which are matched continuously at* 18 kHz*, but not constantly differentiable. The steep rise below* 5 kHz *is propably a feature caused by the hydrophones.*

An algorithm used to calculate the first derivative of an discrete graph for value n with distance w to the next bin is:

$$\frac{dx_n}{df} = \left(x_{n-2} - 8 \cdot x_{n-1} + 8 \cdot x_{n+1} - x_{n+2}\right) / (12 \cdot w) \quad . \tag{4.13}$$

This is the common formula to evaluate the central derivative numerically with a 4th order precision. This formula is applied to the measured spectra, in order to see whether the slope

of the spectrum changes with the wind speed. Since the Knudsen curves simply assume that the amplitude of the noise increases, but the spectral index remains the same, the curves for different sea states should only be separated by a constant difference in dB. Therefore, if one derives these curves, they should have the exact same graph. As it is shown in the following formula, the derivative is independent of the value of the amplitude NL_{1k}.

$$\begin{aligned} \frac{d\mathrm{NL}}{df}(f) &= \frac{d}{df}\left(NL_{1k} - I \cdot \log_{10}(f) \right) \\ &= -\frac{I}{f \cdot \ln(10)} \end{aligned} \tag{4.14}$$

However, if one examines the derivation of the measured spectra in Fig. 4.31, it can be seen clearly that the slope changes. It is easy to see that the graphs have an lower value with increasing sea states within the frequency range of 5 kHz to 30 kHz. So, the absolute value of the spectral index describing the power law in the Knudsen curves would have to increase with increasing sea state to reflect that behavior appropriately. If one takes a close look to the spectra in 4.30, then the faster roll-off for higher wind speeds can also be observed there. Additional spectra are shown in Appendix A.3 for other sensors, proving that this is not caused by a feature of the detector. It should also be noted that a weak signal with a small frequency spread is easier to identify in the derivation than in the original spectrum: the ambient noise changes slowly with the frequency and generates a mostly flat line, while such a signal causes a sharp bipolar peak in the derivative.

5. Modeling the spectral noise shape

5.1. Ray tracing of the paths

In order to fully understand the spectral shape of the ambient noise in the deep sea, the position where the noise is created and how it reaches the hydrophone has to be considered. The properties of the spectrum will change along the path from the source to the detector, because the attenuation in sea water highly depends on the frequency. In general it can be said that the higher the frequency, the higher the losses per unit distance. This could explain the variation of the slope of the spectra discussed in the previous section. The absorption coefficient is calculated using the parametrization by Ainslie and McColm [32]. It changes with salinity, pressure(depth), temperature and acidity of the ocean. The absorption by a near surface bubble layer, which depends on the wind speed an therefore the sea state, is also considered.
Now, since it is assumed that the ambient noise in the ocean is caused by waves, wind or shipping noise, which are all generated at the air/sea interface, the sound has to be propagated from the surface to the deep sea. Here, a ray tracing algorithm executed by a computer program was chosen, since an analytical solution is not attainable with reasonable effort. The code described in the following part is based on a ray tracing software implementation from Max Neff [24] and has been adapted to simulate the ambient noise spectrum.
The implementation used here assumes that the sound ray is generated somewhere at the sea surface and emitted under a certain angle α_0, with the boundary condition that the ray is never reflected at the bottom of the ocean. The task to find a path from the starting point to the hydrophone can be solved similar to the propagation of light in a gradient fiber, if one assumes a horizontally homogeneous medium, i.e. only a depth-dependence of the parameters. So a polar coordinate system is chosen for the horizontal plane, with the radial coordinates r and ϕ. The assumption of a horizontally homogeneous medium leads to a radial symmetry in the paths of the rays. Therefore the only parameter that matters for the shape of the path is the distance between the detector and the origin of the ray. Then the ray can be propagated along the radial coordinate by solving the following ordinary differential equation system:

$$\frac{d}{dr}\sin(\alpha) = -\cos(\alpha)\cdot\frac{c'(z)}{c(z)} \tag{5.1}$$

$$\frac{d}{dr}\cos(\alpha) = \sin(\alpha)\cdot\frac{c'(z)}{c(z)} \tag{5.2}$$

$$\frac{d}{dr}z = \frac{\sin\alpha}{\cos\alpha} \tag{5.3}$$

With :

r : radial distance from the detector

z : depth of the ray at distance r

α : angle between the horizontal and the propagation direction

c : sound velocity at depth z

See Appendix A.2 for a derivation of the ray equations. The algorithm starts at a distance r_0 and emits the ray with an emission angle α_0. The ray is propagated the whole radial distance

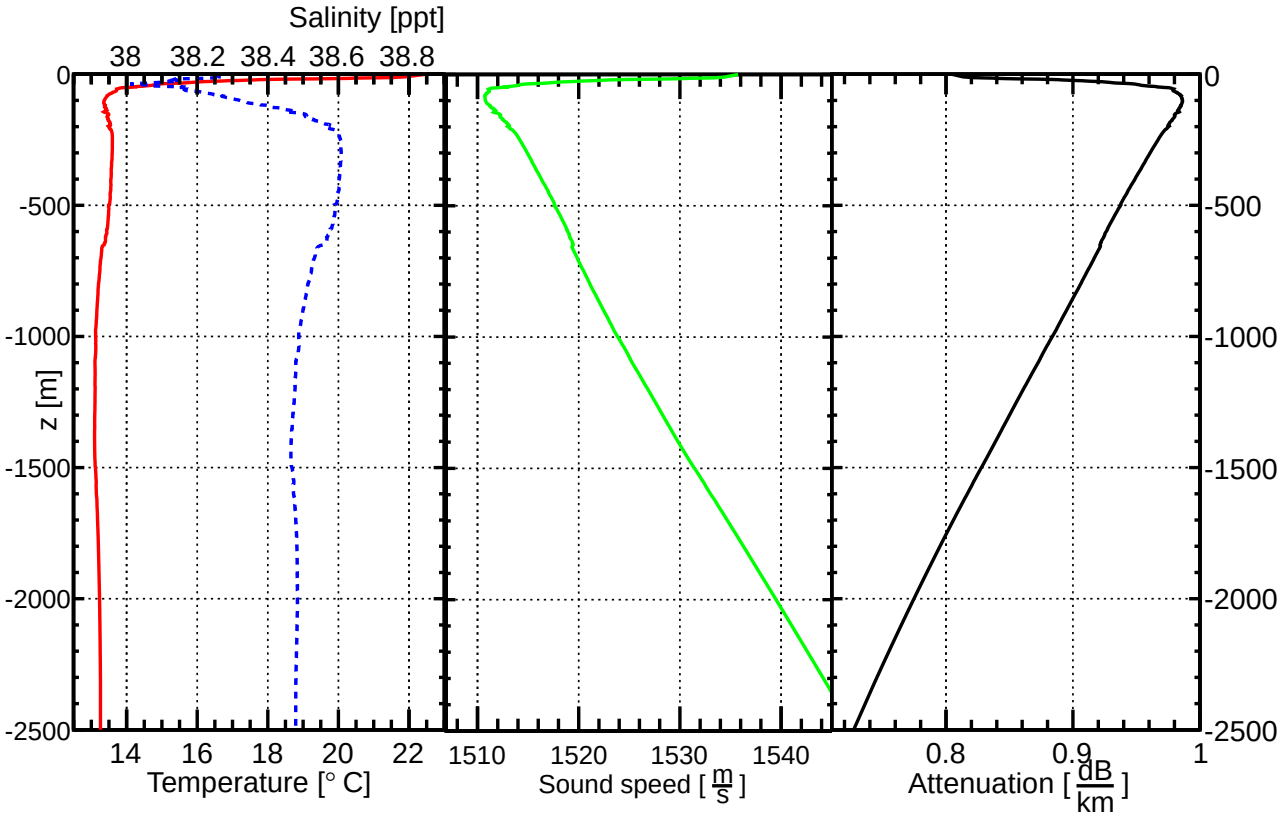

Figure 5.1.: *Depth profiles for some environmental parameters recorded at the ANTARES site. The left pane shows the salinity in blue and the temperature in red. The sound speed can be seen in the middle, while the attenuation coefficient is displayed on the right side. The latter two quantities are derived from the first two.*

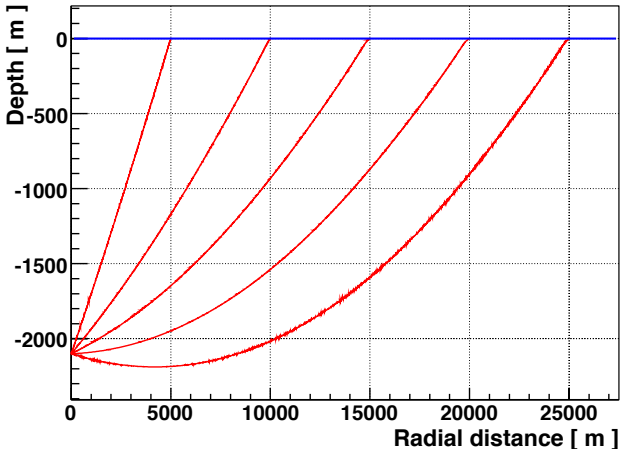

Figure 5.2.: *Example output of the ray tracing algorithm for several radial distances.*

between r_0 and the position of a receiver at $r = 0$ using the ray equations. If the ray cannot reach the receiver, a new emission angle α_1 is chosen and the algorithm starts at the same distance r_0 again. This process is repeated, until an exemplary hydrophone at 2100 m depth is hit. Then, another path for a new starting distance r_0 can be calculated. The depth profiles shown in Fig. 5.1 are used to determine the sound speed for the ray tracing. Some examples of the calculated paths for distances ranging between 5 km to 25 km are shown in the Fig. 5.2. In order to calculate the spectrum, it is assumed that the injection spectrum at the sea surface is a simple power law $A \cdot f^{-i}$, similar to the Knudsen curves. An isotropic emission characteristic is

assumed for the generation of the noise, and the same power law is used for all starting points. The increasing radial distance is taken into account by multiplying the amplitude with the area of the annulus, which is delimited by two neighboring starting values for the radial distance. The attenuation is calculated using the path from the surface to the detector. Two different sources of absorption were considered: the sound absorption by sea water and the loss while passing the near surface bubble layer. The formula for the viscous and chemical absorption in sea water α is according to Ainslie and McColm [32]:

$$\alpha = \sum_i \alpha_i \tag{5.4}$$

$$\alpha_1 = 0.106 \cdot \frac{f_1 f^2}{f^2 + f_1^2} \cdot \exp\left(\frac{pH - 8}{0.56}\right) \tag{5.5}$$

$$\alpha_2 = 0.52 \cdot \left(1 + \frac{T}{43}\right) \cdot \frac{S}{35} \cdot \frac{f_2 f^2}{f^2 + f_2^2} \cdot \exp\left(-\frac{z}{6}\right) \tag{5.6}$$

$$\alpha_3 = 0.00049 \cdot f^2 \cdot \exp\left(-\frac{T}{27} - \frac{z}{17}\right) \tag{5.7}$$

This formula returns the attenuation in $\frac{\mathrm{dB}}{\mathrm{km}}$ and uses the following notation for the input parameters: temperature T in °C, depth z in km, frequency f in kHz and salinity S in ppt. The relaxation frequencies f_1 and f_2 are determined in kHz with the following formula [32]:

$$f_1 = 0.78 \cdot \left(\frac{S}{35}\right)^{0.5} \cdot \exp\left(\frac{T}{26}\right) \qquad \text{(boron)} \tag{5.8}$$

$$f_2 = 42 \cdot \exp\left(\frac{T}{17}\right) \qquad \text{(magnesium)} \tag{5.9}$$

The second part of the absorption is caused by the bubble layer, that is present in the first 30 m of the sea water. The strength of the extinction highly depends on the wind speed, because the density of the bubbles is governed by the agitation of the sea surface. At a wind speed of 6 kn (sea state 2, almost 3), the waves begin to break. Breaking waves are the main cause for the formation of a near surface bubble layer, and most foam is generated in that way. Another source for bubbles is marine life, e.g. algae, but their contribution should be small and cannot be modeled that easily, since their population depends strongly on the season, sea currents and nutrient concentration. So this last effect is not considered here. Because the sound has to pass this layer, additional absorption and scattering takes place. The pressure wave interacts with the bubble and may for example initiate an oscillation, which causes scattering and sound extinction. This effect can be accounted for with a model developed by the Applied Physics Laboratory of the University of Washington [33]. Here is a formula for the depth integrated sound loss due to bubbles:

$$SL = \exp\left(-\frac{\beta(v)}{\sin\alpha}\right) \tag{5.10}$$

with the following parametrisation for β :

$$\beta(v) = \begin{cases} 0.8192 \cdot \left(\frac{f}{25}\right)^{0.85} \cdot \left(\frac{v}{11}\right)^{3.5}, & \text{if } v > 11\,\mathrm{m/s} \\ \left(\frac{f}{25}\right)^{0.85} \cdot 10^{-5.2577 + 0.4701 \cdot v}, & \text{if } v \leq 11\,\mathrm{m/s} \end{cases} \tag{5.11}$$

with the frequency f in kHz, emission angle α and wind speed v in $\mathrm{m\,s^{-1}}$. The final spectrum FS is then calculated from the injection spectrum IS with the following formula:

$$FS(f) = SL(f, v) \cdot 10^{-0.1 \cdot \alpha(f) \cdot l} \cdot IS(f) \tag{5.12}$$

Table 5.1.: *Parameters for the injection spectra in a logarithmic scale.*

Sea state	Amplitude [dB re 1 µPa^2/Hz]	Spectral index [dB re 1 µPa^2/Hz]
0	54.8(7)	−13.6(6)
1	60.7(6)	−17.0(5)
2	70.6(3)	−22.2(4)
3	78.8(2)	−27.8(2)
4	87.1(3)	−33.5(3)
5	92.1(2)	−34.2(2)

After the attenuation is taken into account, the noise reaching the detector from that point of the sea surface is known. In order to get the total noise, the ray tracing is done in 100 m radial steps, up to a distance of 26.5 km. For greater distances it is not possible to reach the detector without a reflection from the bottom. This is not considered here, because the reflection loss has a the magnitude of ∼10 dB. The angle, at which the ray reaches the hydrophone naturally changes with the starting distance. An example of the angular noise distribution can be seen in Fig. 5.3. Most of the noise, especially in the low frequency band, is received from the sides, which means that it doesn't matter whether the hydrophone is pointing upwards or downwards. This effect is also seen in the data recorded with AMADEUS, since there are storeys with a different orientation that exhibit the same ambient noise level. Also the average receiving angle for the surface noise increases with the frequency, which is an effect of the attenuation. The formula for the transmitted noise level is proportional to $\propto \exp(-\alpha l)$, so it decreases exponentially with the traversed distance. Since higher frequencies are damped more per unit distance and the length of the path increases with lower arrival angles, the attenuation dominates over the growing emission area for the high frequencies.

5.2. Fitting the model to the data

For each receiving angle, the spectra are added up, which gives the final result. As initial parameters for the injection spectrum, the values from the Knudsen curves are used. With these spectral indexes, the measured spectra cannot be reproduced. That is expected, since they were measured in a specific region of the world, and the sea currents and temperature can differ significantly for another location, causing a different ambient noise spectrum. Therefore the injection parameters were modified to match the measured noise spectra of sensor 21. For that to happen, the spectrum is simulated multiple times, and the difference to the measured data in the range of 5 kHz to 30 kHz is used to evaluate the quality of the input parameters, which is the frequency range where the detector is sensitive to the ambient noise. The measured data were filtered to remove the transient signals and the inherent noise of the hydrophone was subtracted as discussed in Sec. 4.5.3. The injection parameters producing the best matching spectra are displayed in Tab. 5.1. The absorption along the path to the hydrophone is not sufficient to explain the change in the slope of the spectra, and therefore the spectral index had to be modified with the sea state. However, this might not mean necessarily that this is also true for shallow water, as the data analyzed here was only acquired in the deep sea.

A plot of the resulting wave noise model for the ANTARES site is shown in Fig. 5.4 together with the median of the power spectral densities acquired in the years 2008–2011. The residuals for each sea state are shown in the Fig. 5.5. The modeled spectrum lies within ±1 dB of the median of the measured data in the range 7 kHz to 30 kHz. As expected, the model becomes

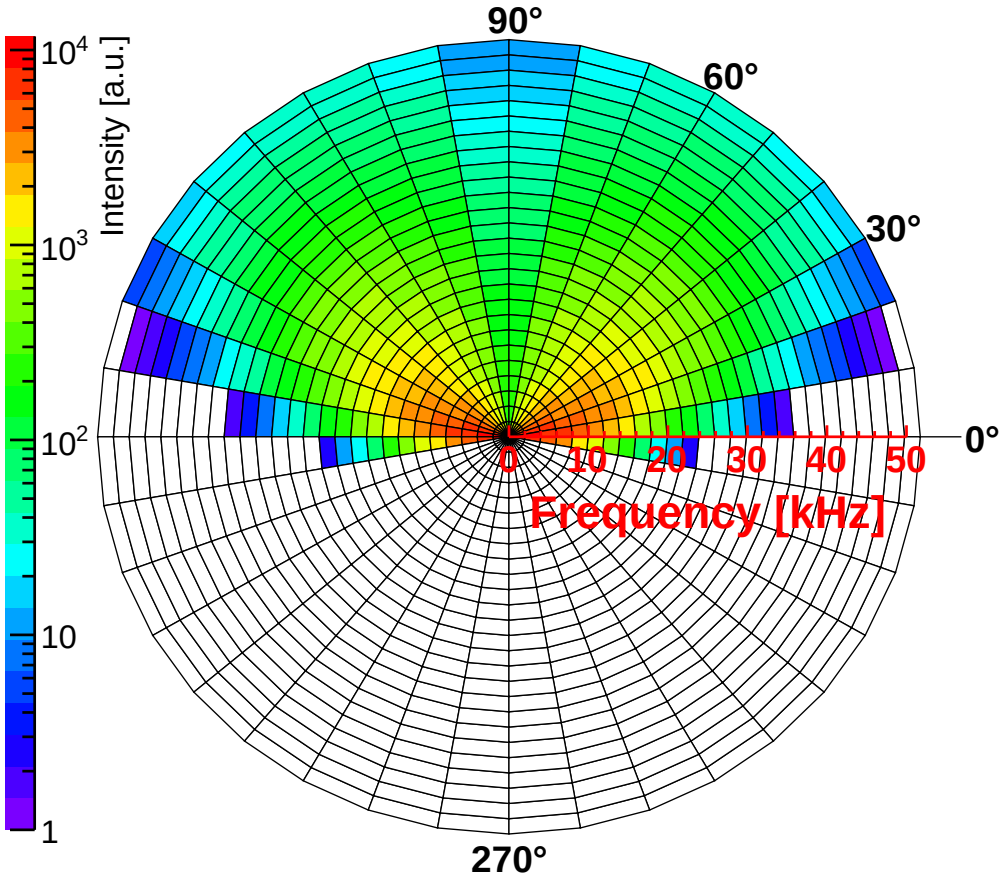

(a) Sound received per angle

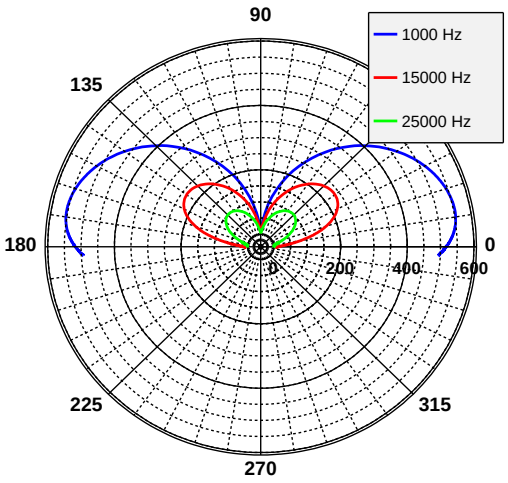

(b) Line profile

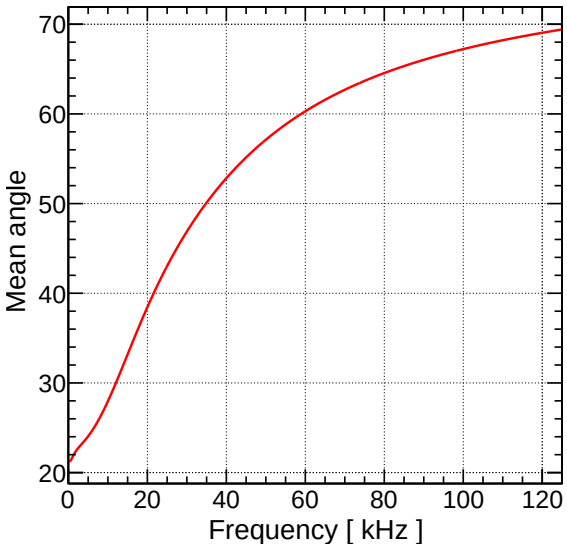

(c) Average receiving angle

Figure 5.3.: *Output of the ray tracing algorithm. Panel (a) shows the received noise per angle at the hydrophone. The frequency is mapped as the radial coordinate, while the color represents the intensity in arbitrary units. The line profiles of the received noise for certain frequencies are displayed in (b), while the plot in (c) illustrates the variation of the direction of the noise with the frequency.*

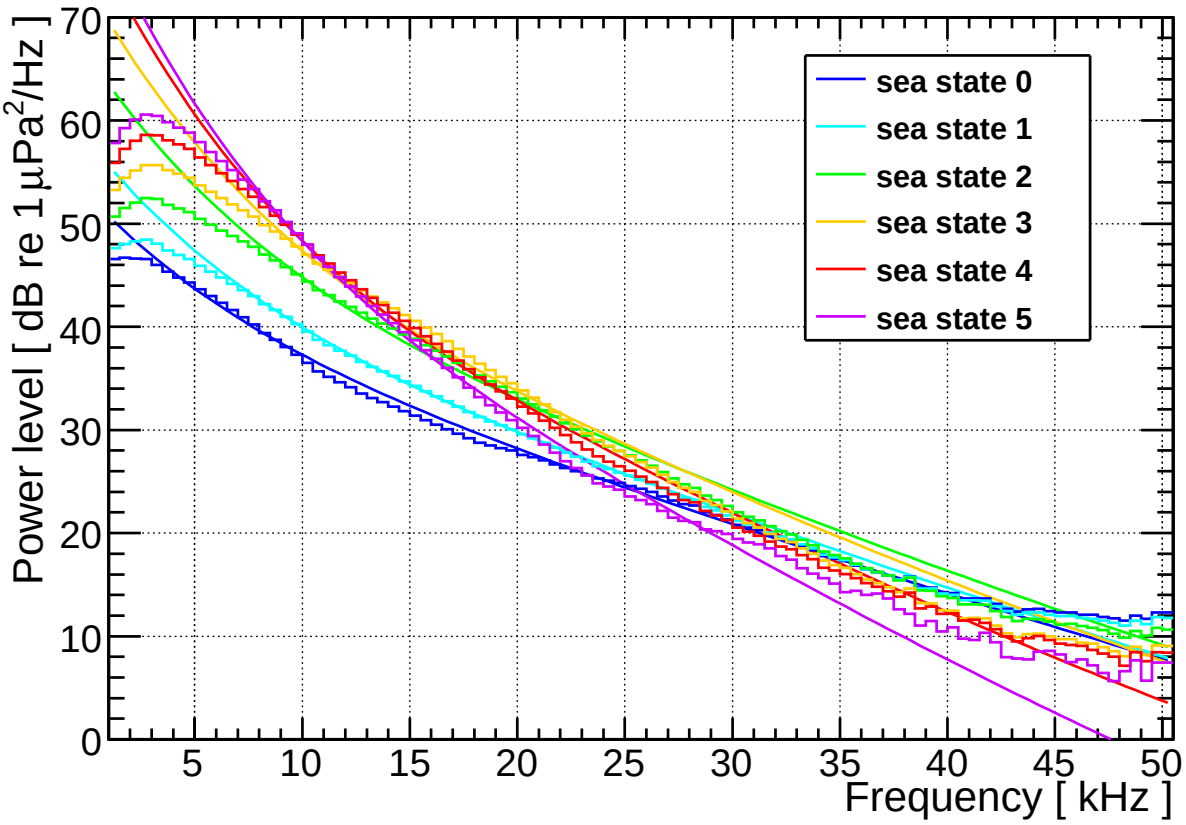

Figure 5.4.: *Measured noise spectra by sensor 21 after cuts for transient signals and subtraction of the $3\,\sigma$ quantile (histogram) and the model for the ambient noise (smooth lines).*

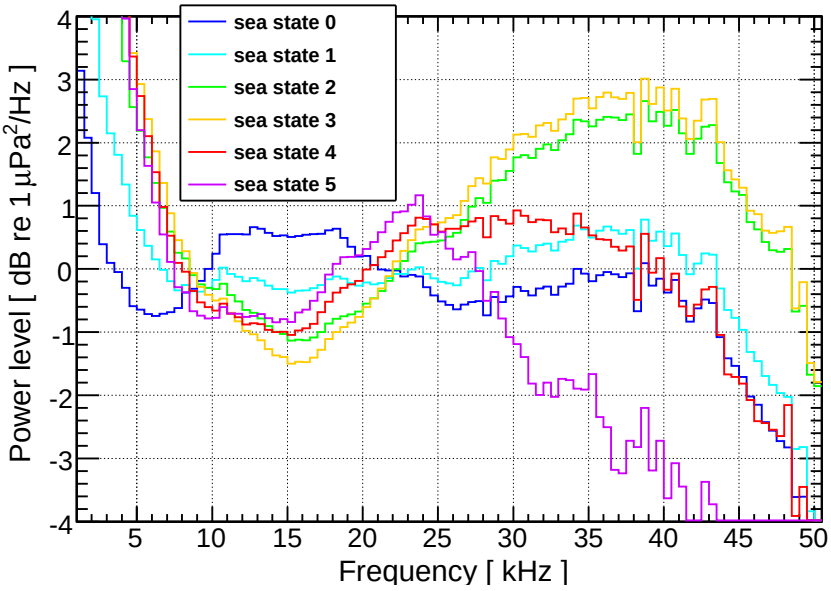

Figure 5.5.: *The residuals between the measured noise by sensor 21 and the model. Both values were simply subtracted, so a value greater than zero means that the model is above the measurement and vice versa.*

Table 5.2.: *A table containing the parameters to describe the simulated spectrum by an 8th order polynomial of the form $a_i \cdot f^i$. The frequency f has to be in* kHz*, while the returned value is in* dB re 1 µPa^2/Hz

sea state	a_0	a_1	a_2	a_3 10^{-3}	a_4 10^{-5}	a_5 10^{-7}	a_6 10^{-10}	a_7 10^{-12}	a_8 10^{-13}
0	52.28	−2.16	0.09	−2.88	5.41	−4.69	−6.49	42.69	−2.25
1	57.44	−2.53	0.10	−3.17	5.44	−4.15	−6.48	29.69	−1.28
2	65.69	−3.02	0.12	−3.46	5.45	−3.69	−6.28	20.05	−0.61
3	72.22	−3.61	0.14	−3.86	5.49	−3.00	−6.20	4.24	0.53
4	77.56	−4.28	0.17	−4.44	5.60	−1.99	−6.92	−19.18	2.30
5	79.92	−4.59	0.18	−4.61	5.62	−1.70	−6.94	−26.00	2.79

unreliable outside of this frequency band, since the hydrophones are not sensitive to the ambient noise above 30 kHz. To further estimate the error of the model, we can take a look at the other uncertainties in this analysis. First, the calibration was not performed perfectly accurate, because it has been done only in the laboratory and not in situ. The calibration source had a emission characteristic $\propto f^2$ with high uncertainties below 5 kHz. The error caused by the calibration in total is about 2 dB, which is already greater than the difference between the model and the data. The same calibration is used for all spectra of a unique hydrophone, so the distribution of the spectra is not affected. Only the absolute value and possibly the spectral index would change if the calibration is wrong, but the effect on them would be a simple offset for all sea states. Additionally, only absorption along the path is taken into account, while dispersion, scattering and additional sound sources (the bubbles) along the path are not considered. This is probably the main uncertainty in this model. Apart from that the classification of the spectrum in a certain sea state is also error prone, since the wind speed is measured 40 km away and the swell is not driven by the local wind conditions. This means that there are also falsely classified events in each sea state, broadening the distributions. But there is also a natural spread of the spectra, because a single sea state covers a range of about 5 kn of wind speeds. The spread of the spectra for one sea state is approximately 4 dB wide (see Fig. 4.29). The model lies well within that boundaries. Therefore this model can be considered a good estimate for the ambient noise spectrum in the deep sea.

The output of the ray tracing program is a spectrum parametrized by a long row of numbers. Since that is not as useful as an analytic function for the implementation in another computer program, a polynomial of degree 8 is fitted to the model $FS(f)$. The resulting values for that fit are shown in the Tab. 5.2, and were used to create a C++ implementation of the model. It provides various functions that take the average wind speed and the frequency as parameters, and return the ambient noise power spectral density in dB re 1 µPa^2/Hz, see App. A.4 for more details.

5.3. Comparison between simulated neutrino signals and the ambient noise model

The actual goal for the analysis of the ambient noise in this thesis is the comparison of the ambient noise with the expected neutrino signal. In order to do this comparison, the ACoRNe Acoustic Simulator [34, 35] was used to generate the neutrino signals in MATLAB [36]. Examples for the simulated signals and their energy spectral density (ESD) are shown in Fig. 5.6.

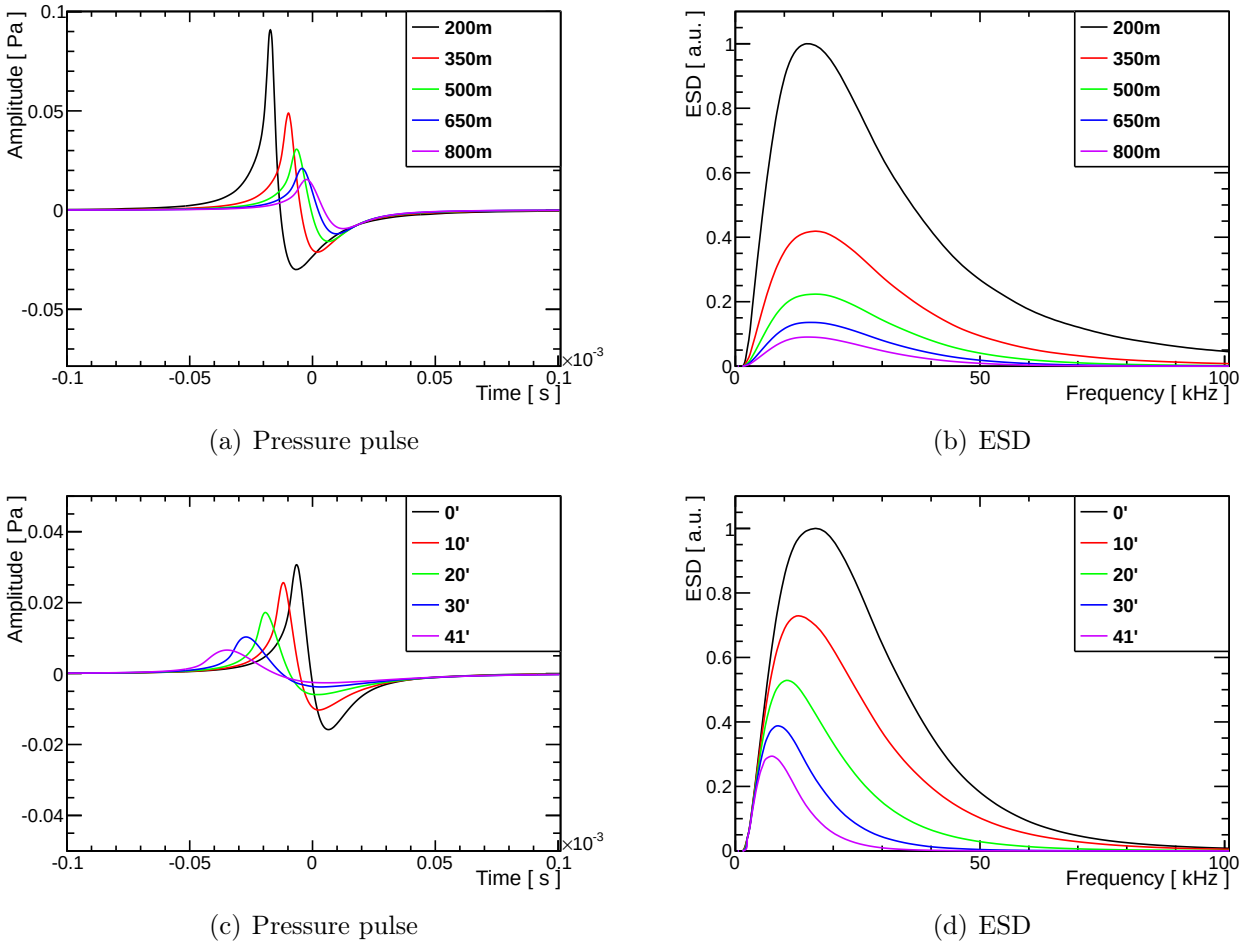

(a) Pressure pulse

(b) ESD

(c) Pressure pulse

(d) ESD

Figure 5.6.: *Examples for the simulated neutrino signals. Some pressure pulses for a neutrino energy of* 10 EeV *and varying distances in the plane of the* pancake *are shown in (a), and the corresponding energy spectral densities in (b). In (c) and (d) analogous graphs are displayed, but now for a* 10 EeV *neutrino at a fixed distance of* 500 m*, observed with varying angles to the main emission direction.*

The comparison of the simulated signal and the new ambient noise parametrization is performed in the frequency domain. In order to get the frequency range with the best signal-to-noise ratio (SNR), both spectra are integrated from a lower frequency f_{low} up to the upper limit f_{up}. The resulting values from the integration are divided through each other to get an estimate for the SNR, see Fig. 5.7. This procedure was repeated for different shower energies of 1 EeV, 10 EeV and 100 EeV, distances from 200 m to 800 m and sea states 0 to 5. The events were created with multiple angles below 1° to the direction of the pancake. The resulting optimal frequency range for all these events is 20(5) kHz to 56(6) kHz. Although the maximum of the spectrum for neutrino signals is in the range 5 kHz to 15 kHz, the SNR value for frequencies below 10 kHz is small compared to higher frequencies, because the ambient noise rapidly falls off with rising frequencies. Hence the lower frequency limit of the window is determined by the computer as 20(5) kHz.

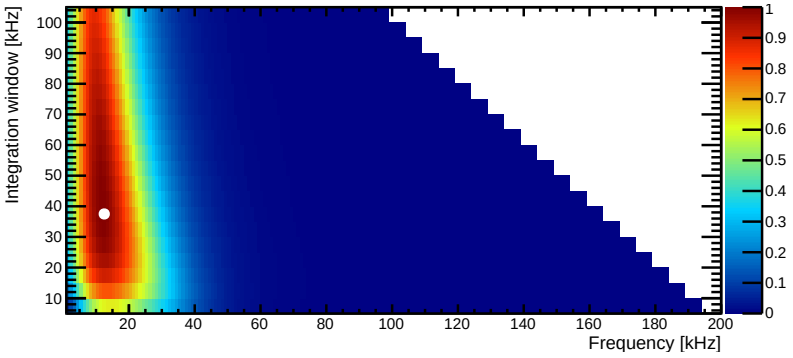

(a) 500 m 32′ 10 EeV Sea state 1

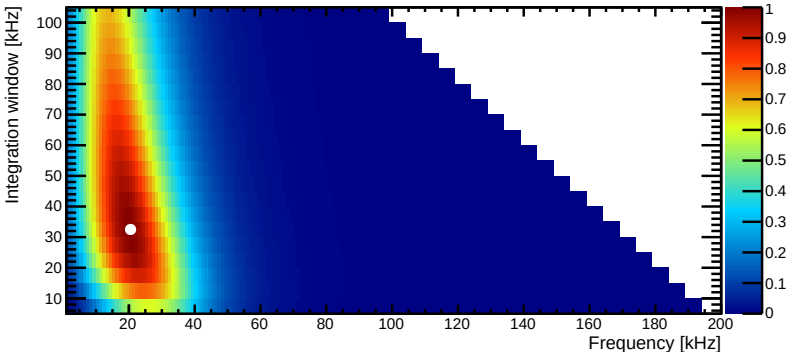

(b) 650 m 13′ 10 EeV Sea state 1

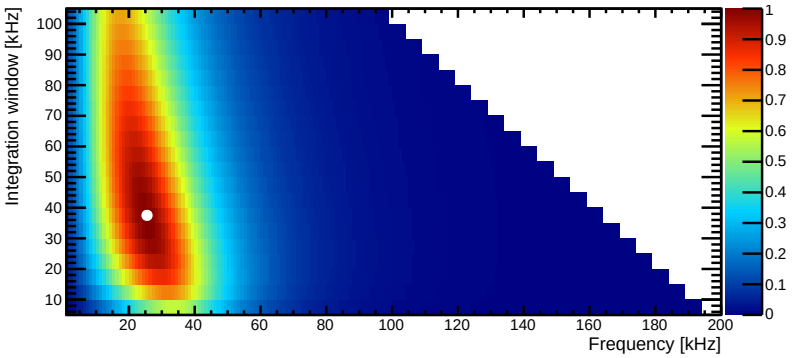

(c) 350 m 18′ 10 EeV Sea state 2

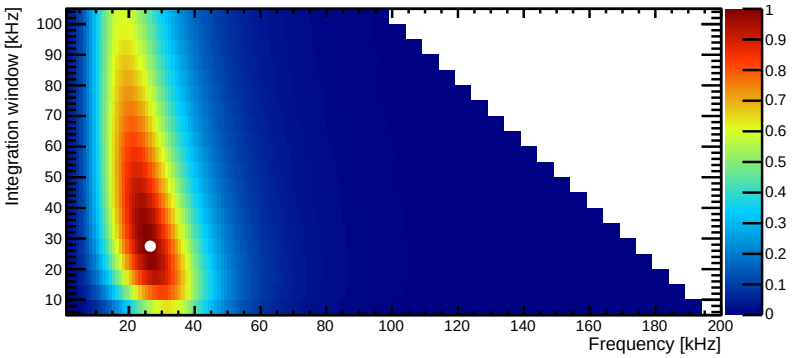

(d) 500 m 0° 100 EeV Sea state 4

Figure 5.7.: *Four examples for the determination of the optimal frequency range for acoustic neutrino detection. The abscissa is the start of the frequency window, while the ordinate defines its length. The color shows the SNR in arbitrary units. The position of the observer as radial distance, angle to the pancake axis and the neutrino energy are shown in the captions. A white marker is drawn at the best position, e.g. for (a) the optimal range is* 22 kHz *to* 60 kHz.

Considering that the emission is very focused at an angle of 90° to the shower axis and that the maximum in the energy spectral density is at lower frequencies for bigger angles, it might be advisable to reduce the lower frequency boundary. For example, at an angle of 30′ to the main emission direction, the frequency range with the best signal to noise is 16(5) kHz to 54(5) kHz. If the angle to the main emission direction is increased further, the the band with the best SNR falls to lower frequencies. So it should be advisable to use sensors which are sensitive from 10 kHz to 55 kHz and that have an inherent noise below the ambient noise level in that frequency range. This could increase the probability to detect the *pancake* if the sensor is not in the plane of propagation and it would yield the best SNR.
The dependency of the estimated signal-to-noise ratio in the optimal frequency range to the distance to the interaction point and shower energy is displayed in Fig. 5.8 as a consistency check. The SNR scales with the square of the primary energy, because the amplitude of the bipolar pulse is proportional to the shower energy and the energy spectral density scales with the square of the amplitude. The amplitude also scales with $\frac{1}{r}$, so the estimated value scales with $\frac{1}{r^2}$. However, these values are only estimates and should not be considered as true signal-to-noise ratios. A real SNR estimation would have to include the inherent detector noise, the response of the hydrophone and trigger efficiency. Also, the ESD wouldn't be used, but the signal amplitude. The method used here however is valid for the determination of the best frequency window for acoustic neutrino detection.

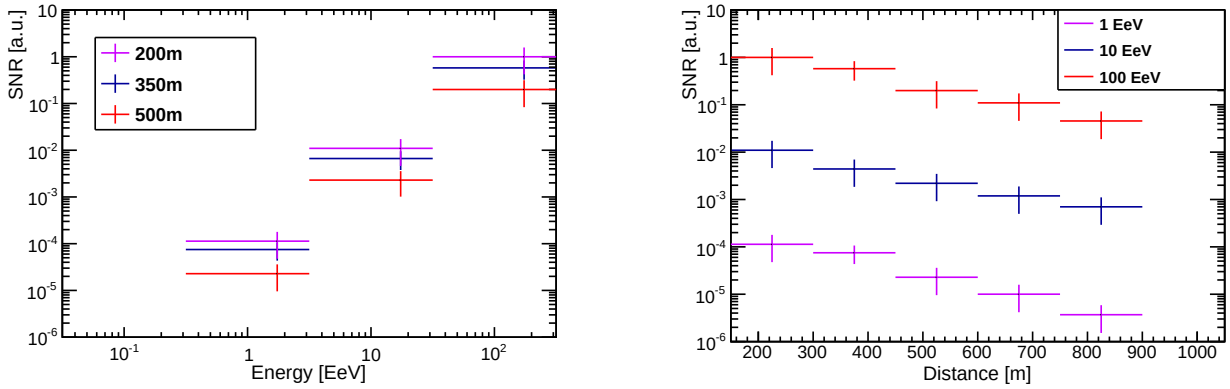

(a) Energy dependecy (b) Distance dependency

Figure 5.8.: *The dependency of the SNR to the distance and the neutrino energy.*

6. Summary and Conclusion

The ambient noise in the Mediterranean Sea at the ANTARES detector site was analyzed in this thesis. The ambient noise forms the background for acoustic neutrino detection, and it also determines the energy threshold, the array setup and the effective volume for a future acoustic detector. The investigation of this detection method is motivated by the large effective volume (greater than 100 km^3) needed to detect ultra-high energy neutrinos above 1 EeV with statistical significance. While this is also possible with the optical detection of neutrinos, the spacing between the instruments required for the detection of the Cherenkov photons has to be in the same magnitude like the attenuation length of 60 m for light with a wavelength in the detected region. The instrumentation density for the acoustic detection technique however is not constrained by the attenuation length, and a sparse detector with $\mathcal{O}(100)$ sensor clusters per 1 km^3 is sufficient. This reduces the cost to build such an array and increases the probability to get enough funding for such a project.
In this work, the minimum bias data of the acoustic test system AMADEUS was analyzed. A $\sim$10 s long acoustic sample is recorded every hour for all 36 acoustic sensors integrated in the ANTARES neutrino telescope. The average standard deviation of the pressure in all events recorded by the commercial (HTI) hydrophones is 34(3) mPa in the whole frequency range from 1 kHz to 125 kHz. However, the minimum bias data set contains transient signals and shipping noise, so different cuts were applied to get a pure set of the ambient noise. A filter for signals of the ANTARES positioning system was used, that removes samples with peaks in the spectrum from 45 kHz to 80 kHz. Another cut on the tails of the amplitude distribution of the pressure is applied, because the ambient noise should be Gaussian distributed and not heavy-tailed. Finally, a third cut on the rate at which the ambient noise increases with time is utilized. The weather varies slowly over time, so only shipping noise or heavy rain can cause drastic increases of the standard deviation between two measurements. Since ships have a broad noise spectrum due to the cavitation of their propeller, the total noise level is simply increased and no additional features in the spectrum appear. Accordingly, the cut on the rate is the only way to remove the shipping noise from the minimum bias data. These cuts remove a total of 38 % of the data samples. Interestingly, they remove 70 % more events in certain time intervals, specifically from 1:00 to 3:00 o'clock (UTC) and from 20:00 to 22:00 o'clock (UTC), than on average during the rest of the day, see Fig. 6.1. When the daylight savings time is taken into account, then this peak becomes smaller and is only one hour wide. This leads to the conclusion that it is an anthropogenic effect, because a natural phenomenon should not be influenced by the way humans track the time. It is attributed to ships (ferries) passing the detector, especially since the departure times at 21:00 CET of the night trips for a lot of ferry routes match with the two time intervals, if one keeps the distance they have to travel to the proximity of the detector in mind.

After the cuts are applied, the average standard deviation of the recorded pressure level by the HTI hydrophones is 22(3) mPa. The filtered minimum bias data should now be a good estimate for the pure ambient noise level, which is assumed to be caused by the waves at the sea surface. As the waves are agitated by the wind speed, a correlation between those two values should be observed. The correlation factor between the 10 min average wind speed measured at Cap Cépet and the ambient noise level recorded by all HTI hydrophones is 73.7(12) %. The swell is not considered here, which causes waves without the presence of local winds, so the

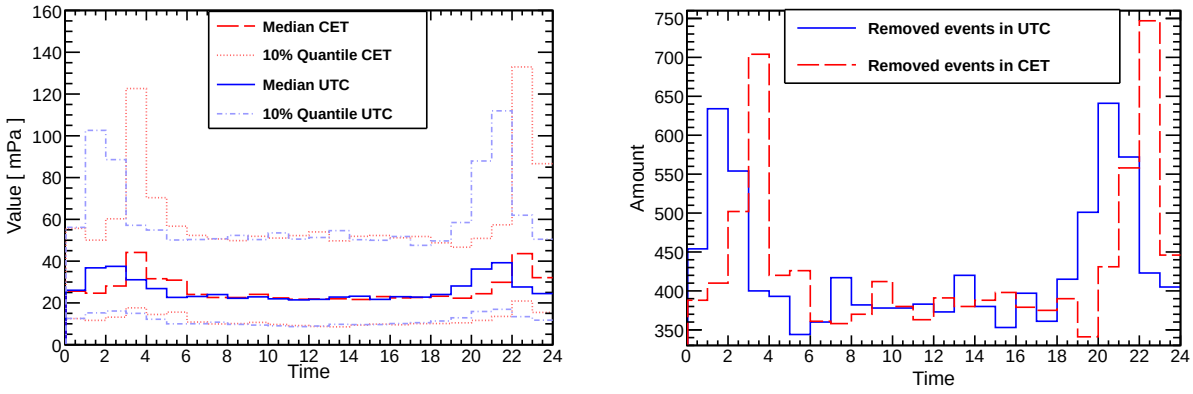

(a) Quantiles (b) Events removed

Figure 6.1.: *Graph (a) shows the quantiles of the distribution of the standard deviation from the minimum bias data of a HTI hydrophone during a day without filtering. There is a clear difference in the shape of the curves, depending on whether the daylight savings time is considered or not. Panel (b) shows the number of events removed per hour in the day, showing that the cuts used for the analysis are triggered more often during these high noise periods.*

correlation factor cannot reach 100 % even if the waves were the only cause for the ambient noise. Keeping this in mind, the observed correlation is in good agreement with the hypothesis that the ambient noise is driven by the waves. A variation of the correlation factor over time is also observed. The correlation drops to $\sim 60\,\%$ during the specific intervals of the day in which the cuts remove significantly more samples, while it is stable at about 75 % for the rest of the day. Again, this indicates an anthropogenic effect, since the wind speed shows no specific behavior during that time. The noise level also varies with the season, like it is also the case for the wind speed. During winter the wind is stronger in the Mediterranean Sea, which increases the standard deviation of the recorded samples by about 4 mPa. The correlation factor also changes during the year, and the shape of this graph is very similar to the average wind speeds recorded in these months. The maximum correlation of 80 % occurs in December and January, while the minimum of 60 % happens in May and August, see Figs. 6.2 and 6.3. This variation of the ambient noise background leads to a varying energy threshold and effective volume of an acoustic neutrino telescope and has to be considered in simulations for a future acoustic detector.

Another aspect for an R&D project like AMADEUS is the estimation of the development of the sensor characteristics over time. As it can be seen in the minimum bias data, the inherent noise of all three different sensor types used in this setup stayed constant from 2008–2012. Under the premise that the year-averaged ambient noise did not vary in this period, an assessment of development of the sensitivity can be made with the distributions of the recorded standard deviations in the minimum bias data. The sensitivity stays constant for the self-made hydrophones and the acoustic modules, while the commercial HTI hydrophones have lost 2 dB sensitivity. However, this is only a rough estimate, because currently there is no in situ calibration source. The assumption that the ambient noise is constant for these years might be wrong, although it is supported by the data from the self-made hydrophones.

Two methods for the determination of the spectrum of the inherent detector noise were also compared. One of them uses the lower $3\,\sigma$ quantile of all recorded spectra as the inherent noise. The other method developed here uses a deconvolution of the noise spectra, that are generated from two independent probability distributions. The latter method gives a more realistic result, if one knows the analytic functions for both distributions. It also works better once the electronic noise has the same (or a higher) magnitude than the ambient noise, because

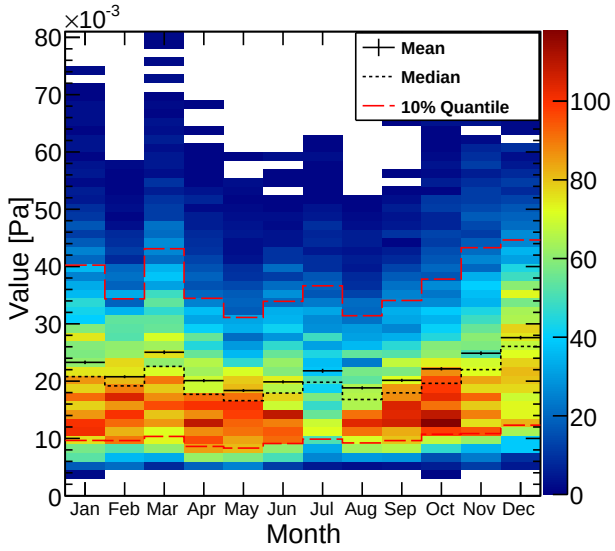

Figure 6.2.: *The standard deviation of the minimum bias samples during a year and the quantiles of the histograms.*

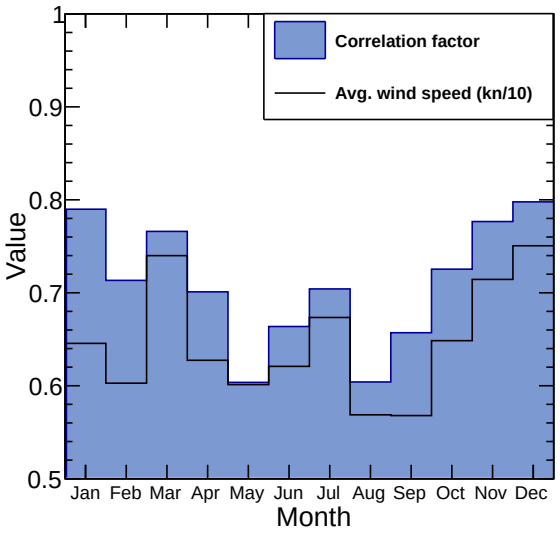

Figure 6.3.: *Monthly variation of the correlation factor in a year. The average wind speed is also shown.*

it is safe to assume a Gaussian distribution for this kind of noise. Both methods show that the commercial hydrophones have a lower inherent noise than the ambient noise up to 25 kHz, and that the data with the inherent noise subtracted can be used to extend the upper frequency limit for an analysis of the spectrum of the ambient noise with these sensors up to 30 kHz.
The observed ambient noise power spectral density shows a variation in the spectral index with the sea state, which is not included in the *Knudsen curves*. They describe the ambient noise spectrum through a power law with a fixed spectral index and an increasing amplitude for higher sea states. However, since these curves are only valid in shallow water, a new model has to be found for the ambient noise in the deep sea at the ANTARES detector site in 2100 m depth. Accordingly, a ray tracing program is used to propagate the noise from the sea surface to the detector, while the shape of the spectrum is modified along its path by viscous absorption, chemical relaxation processes of boron and magnesium dissolved in the sea water and absorption and scattering caused by a near surface bubble layer. The spectrum is assumed to be a power law at the sea surface with an isotropic emission characteristics. However, even when the absorption is taken into account, the spectral index still has to increase with higher wind speeds to match the data recorded by the sensors of AMADEUS, see Fig. 6.4. This might be a hint that the *Knudsen curves* have to be modified, but a cross check for that is still necessary, as only data from the deep sea was available for this analysis.
The new parametrization of the spectra, describing the ambient noise recorded by the commercial HTI hydrophones used in AMADEUS with an accuracy of 1 dB in the frequency range of 5 kHz to 30 kHz, is compared to simulated neutrino signals. The optimal frequency window for the acoustic detection of ultra-high energy neutrinos is found to be 10 kHz to 50 kHz. This would also mean that the sensors used in a future acoustic neutrino telescope should have a lower inherent noise than the hydrophones used in AMADEUS. Their equivalent spectral input self noise should be less than 20 dB re 1 $\mu Pa^2/Hz$ at 30 kHz and 10 dB re 1 $\mu Pa^2/Hz$ at 50 kHz to reach the best signal to noise ratio.
The standard deviation of the minimum bias samples in the optimal frequency range for neutrino detection of 10 kHz to 50 kHz and the parametrization of the ambient noise are shown in Fig. 6.5. Because the inherent noise of the sensors is not included in the model, it is also subtracted from the data using the $3\,\sigma$ estimation, which gives a value of 3 mPa for the inherent noise in that frequency band. The model and the data are in very good agreement, which

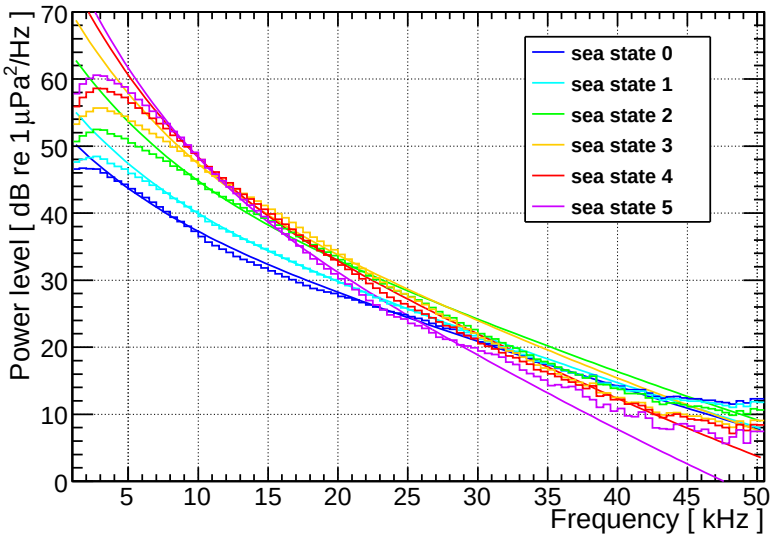

Figure 6.4.: *Measured noise spectra by sensor 21 after cuts for transient signals and subtraction of the* $3\,\sigma$ *quantile (histogram) and the model for the ambient noise (smooth lines).*

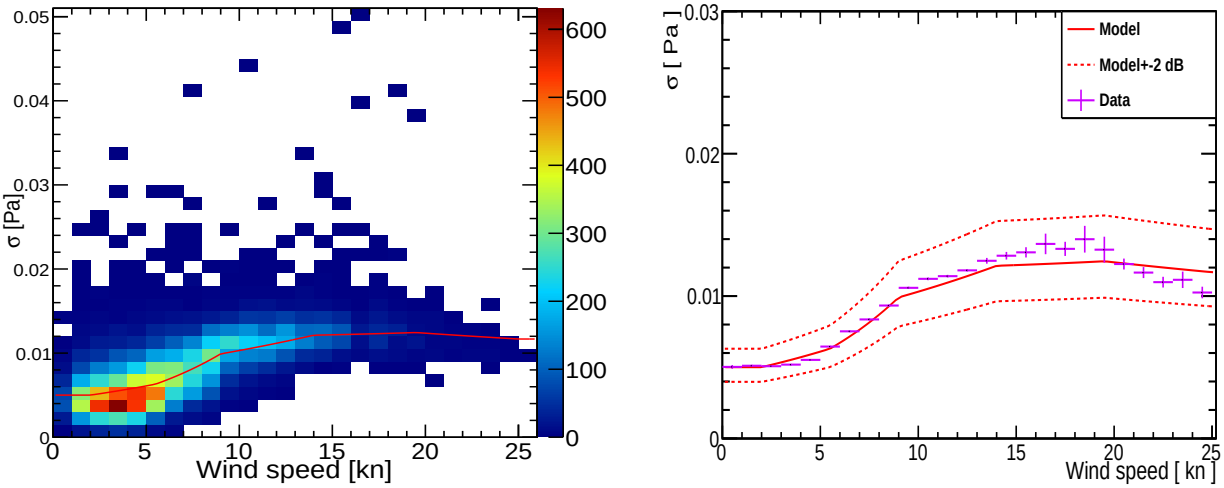

(a) Histogram (b) Profile

Figure 6.5.: *The total noise level predicted by the new model from* 10 kHz *to* 50 kHz *compared to the data recorded by HTI hydrophones. The inherent noise in that frequency range of* 3 mPa *was subtracted from the data.*

proves the validity of the parametrization. However, the plot shows a different behavior than expected, because the noise level quickly saturates with increasing wind speeds. The *Knudsen curves* would predict a steady increase of the noise. But the observed increase of the spectral index, which is also reflected in the new parametrization, leads to a saturation of the noise at 12 mPa. The variation in the noise level between sea state 0 and sea state 5 is reduced to a factor of 2.5, while the old model predicted a factor of almost 8. This is a very nice effect for acoustic particle detection, because the energy threshold is not affected by the weather as much as it was previously assumed.

As a conclusion, the acoustic test system AMADEUS in the ANTARES detector is well suited for the study of the ambient noise, and it can provide a lot of new inputs for a future full-scale acoustic neutrino telescope.

A. Appendix

A.1. Tables

Table A.1.: This table contains some statistical quantities of the unfiltered rms distributions. The interquartile range (IQR) is the difference between the .25 and the .75 quantile, while Sigma is the standard deviation. The Δ values describe the relative change to the previous year. A median of 0.05 mV indicates a defective hydrophone.

	Year	Entries	Median [mV]	IQR [mV]	Sigma [mV]	Δ Median	ΔIQR
	2008	7547	0.05	0.05	0	–	–
Sensor 0	2009	12069	0.05	0.05	0.01	1.00	1.00
	2010	7743	0.05	0.05	0	0.99	0.99
	2008	7547	3.94	3.13	4.70	–	–
Sensor 1	2009	12067	4.04	3.07	5.06	1.03	0.98
	2010	7739	4.07	3.09	3.85	1.01	1.00
	2008	7547	3.85	3.11	4.55	–	–
Sensor 2	2009	12065	3.78	3.16	5.03	0.98	1.02
	2010	7739	3.83	3.21	3.81	1.01	1.02
	2008	7547	7.77	6.35	4.85	–	–
Sensor 3	2009	12064	15.33	1.25	4.26	1.97	0.20
	2010	7739	16.94	0.65	3.03	1.10	0.52
	2008	7547	4.45	3.72	4.97	–	–
Sensor 4	2009	12063	4.31	3.69	5.23	0.97	0.99
	2010	7739	4.43	3.83	4.43	1.03	1.04
	2008	7547	4.07	3.40	4.82	–	–
Sensor 5	2009	12061	3.97	3.36	5.14	0.98	0.99
	2010	7739	4.01	3.40	4.04	1.01	1.01
	2008	7511	1.19	0.93	1.98	–	–
Sensor 6	2009	12013	1.14	0.91	2.05	0.96	0.97
	2010	7846	1.07	0.83	1.30	0.94	0.91
	2008	7511	1.29	1.00	2.15	–	–
Sensor 7	2009	12011	1.25	0.99	2.26	0.97	0.99
	2010	7846	1.17	0.91	1.42	0.94	0.92
	2008	7511	1.17	0.91	1.94	–	–
Sensor 8	2009	12009	1.12	0.87	1.97	0.96	0.96
	2010	7846	1.05	0.79	1.25	0.93	0.91

Continued on next page...

Table A.1 – *Continued from previous page*

	Year	Entries	Median [mV]	IQR [mV]	Sigma [mV]	Δ Median	ΔIQR
	2008	7511	1.25	0.97	2.11	–	–
Sensor 9	2009	12009	1.19	0.97	2.17	0.95	1.00
	2010	7846	1.14	0.89	1.40	0.96	0.92
	2008	7511	1.13	0.88	1.92	–	–
Sensor 10	2009	12009	1.07	0.86	2.02	0.94	0.98
	2010	7846	1.01	0.78	1.24	0.95	0.90
	2008	7511	1.27	1.00	2.15	–	–
Sensor 11	2009	12008	1.16	0.94	2.18	0.92	0.94
	2010	7846	1.10	0.88	1.37	0.95	0.93
	2008	3628	5.28	4.16	5.56	–	–
	2009	1266	5.87	4.47	4.62	1.11	1.07
Sensor 12	2010	8054	5.44	4.58	4.84	0.93	1.03
	2011	10133	5.10	4.42	5.20	0.94	0.96
	2012	9666	5.26	4.20	5.06	1.03	0.95
	2008	3628	7.49	6.62	6.85	–	–
	2009	1266	5.41	4.57	4.90	0.72	0.69
Sensor 13	2010	8054	4.86	4.43	4.64	0.90	0.97
	2011	10133	4.28	4.12	5.14	0.88	0.93
	2012	9666	4.48	3.99	4.86	1.05	0.97
	2008	3628	10.98	9.86	8.76	–	–
	2009	1266	6.77	5.62	5.85	0.62	0.57
Sensor 14	2010	8054	6.10	5.65	5.59	0.90	1.01
	2011	10133	5.53	5.31	5.80	0.91	0.94
	2012	9666	5.91	5.13	5.64	1.07	0.97
	2008	3595	7.86	7.14	7.34	–	–
	2009	1266	6.30	4.88	5.42	0.80	0.68
Sensor 15	2010	8054	5.67	4.99	5.04	0.90	1.02
	2011	10133	5.28	4.69	5.46	0.93	0.94
	2012	9666	5.49	4.56	5.23	1.04	0.97
	2008	3580	5.12	4.44	5.59	–	–
	2009	1266	4.17	3.01	3.53	0.81	0.68
Sensor 16	2010	8054	3.77	3.00	3.83	0.90	0.99
	2011	10133	3.38	2.68	4.16	0.90	0.90
	2012	9666	3.46	2.56	3.88	1.02	0.95
	2008	3388	5.59	4.40	5.81	–	–
	2009	1266	3.43	2.33	2.95	0.61	0.53
Sensor 17	2010	8053	3.23	2.54	3.32	0.94	1.09
	2011	10133	3.00	2.40	3.93	0.93	0.95
	2012	9663	3.17	2.37	3.62	1.06	0.99

Continued on next page...

Table A.1 – *Continued from previous page*

	Year	Entries	Median [mV]	IQR [mV]	Sigma [mV]	Δ Median	ΔIQR
	2008	3526	1.28	0.97	2.32	–	–
	2009	1286	1.32	0.95	1.16	1.03	0.97
Sensor 18	2010	8011	1.14	0.91	1.27	0.86	0.97
	2011	10161	1.01	0.85	1.62	0.89	0.93
	2012	9629	1.01	0.79	1.35	1.00	0.93
	2008	3526	1.23	0.92	2.25	–	–
	2009	1286	1.24	0.89	1.08	1.01	0.96
Sensor 19	2010	8011	1.09	0.85	1.18	0.88	0.96
	2011	10161	0.96	0.78	1.49	0.89	0.91
	2012	9629	0.96	0.73	1.26	1.00	0.93
	2008	3526	1.27	1.01	2.34	–	–
	2009	1286	1.42	1.03	1.23	1.12	1.02
Sensor 20	2010	8011	1.17	0.96	1.31	0.83	0.94
	2011	10161	0.98	0.81	1.52	0.83	0.84
	2012	9629	0.92	0.70	1.23	0.95	0.87
	2008	3519	1.26	1.02	2.33	–	–
	2009	1286	1.33	0.96	1.12	1.05	0.95
Sensor 21	2010	8010	1.15	0.93	1.24	0.86	0.96
	2011	10161	1.02	0.85	1.57	0.89	0.92
	2012	9629	1.02	0.80	1.25	1.00	0.94
	2008	3519	1.30	1.04	2.39	–	–
	2009	1286	1.39	0.99	1.16	1.07	0.95
Sensor 22	2010	8009	1.19	0.95	1.32	0.86	0.96
	2011	10160	1.05	0.87	1.63	0.88	0.91
	2012	9629	1.04	0.80	1.30	1.00	0.92
	2008	3327	1.28	0.97	2.33	–	–
	2009	1286	1.31	0.92	1.09	1.02	0.95
Sensor 23	2010	8009	1.12	0.89	1.23	0.85	0.96
	2011	10157	0.99	0.82	1.55	0.89	0.92
	2012	9629	0.99	0.77	1.32	1.00	0.94
	2008	7359	1.16	1.01	1.84	–	–
Sensor 24	2009	11998	1.12	0.94	1.93	0.96	0.93
	2010	7738	1.02	0.82	1.13	0.91	0.88
	2008	7358	1.27	1.07	2.03	–	–
Sensor 25	2009	11997	1.21	1.00	2.08	0.95	0.93
	2010	7738	1.11	0.89	1.25	0.92	0.90
	2008	7358	1.17	1.01	1.90	–	–
Sensor 26	2009	11996	1.12	0.92	1.89	0.96	0.91
	2010	7738	1.02	0.82	1.15	0.91	0.88
	2008	7322	1.15	0.97	1.86	–	–
Sensor 27	2009	11996	1.05	0.91	1.85	0.91	0.93
	2010	7738	0.96	0.76	1.15	0.92	0.84

Continued on next page...

Table A.1 – *Continued from previous page*

	Year	Entries	Median [mV]	IQR [mV]	Sigma [mV]	Δ Median	ΔIQR
	2008	7306	1.15	1.02	1.83	–	–
Sensor 28	2009	11995	1.06	0.92	1.81	0.92	0.90
	2010	7738	1.00	0.81	1.23	0.94	0.88
	2008	7116	1.20	1.05	1.88	–	–
Sensor 29	2009	11995	1.09	0.95	1.91	0.91	0.90
	2010	7738	1.04	0.85	1.26	0.96	0.90
	2008	3440	4.33	3.51	4.83	–	–
	2009	1271	4.75	3.66	3.96	1.10	1.04
Sensor 30	2010	7945	4.20	3.74	3.97	0.89	1.02
	2011	10159	3.69	3.57	4.38	0.88	0.95
	2012	9655	3.91	3.44	4.43	1.06	0.96
	2008	3440	0.05	0.05	0	–	–
	2009	1271	1.41	1.01	1.25	27.98	20.18
Sensor 31	2010	7941	1.18	1.01	1.37	0.84	1.00
	2011	10158	0.99	0.89	1.64	0.84	0.88
	2012	9655	1.00	0.83	1.44	1.01	0.94
	2008	3440	4.32	3.51	4.90	–	–
	2009	1271	4.88	3.73	4.17	1.13	1.06
Sensor 32	2010	7941	4.32	3.83	4.02	0.88	1.03
	2011	10158	3.79	3.65	4.49	0.88	0.95
	2012	9655	4.02	3.53	4.43	1.06	0.97
	2008	3439	4.40	3.55	4.94	–	–
	2009	1271	0.08	0.13	3.00	0.02	0.04
Sensor 33	2010	7940	0.05	0.05	0	0.63	0.40
	2011	10158	0.05	0.05	0	1	1
	2012	9655	0.05	0.05	0	1	1
	2008	3438	4.54	3.68	4.96	–	–
	2009	1271	5.07	3.93	4.15	1.12	1.07
Sensor 34	2010	7940	4.47	4.00	4.24	0.88	1.02
	2011	10155	3.92	3.81	4.63	0.88	0.95
	2012	9655	4.16	3.68	4.58	1.06	0.97
	2008	3438	1.53	1.20	2.84	–	–
	2009	1271	1.59	1.12	1.37	1.04	0.93
Sensor 35	2010	7940	1.28	1.05	1.45	0.81	0.94
	2011	10155	1.06	0.89	1.65	0.82	0.85
	2012	9655	1.04	0.81	1.33	0.98	0.91

Table A.2.: This table contains some statistical quantities of the filtered rms distributions shown in figure 4.17. The interquartile range (IQR) is the difference between the .25 and the .75 quantile, while sigma is the standard deviation. The Δ-values indicate the relative change between two years.

	Year	Entries	Median [mV]	IQR [mV]	Sigma [mV]	ΔMedian	ΔIQR
	2008	5355	1.10	0.84	0.74	–	–
Sensor 6	2009	7374	1.04	0.71	0.62	0.94	0.85
	2010	5422	1.06	0.74	0.63	1.02	1.03
	2008	5517	1.17	0.91	0.79	–	–
Sensor 7	2009	7917	1.08	0.80	0.68	0.93	0.88
	2010	5809	1.10	0.84	0.68	1.02	1.05
	2008	5467	1.06	0.81	0.72	–	–
Sensor 8	2009	7699	0.97	0.69	0.60	0.92	0.86
	2010	5688	0.99	0.73	0.61	1.02	1.05
	2008	5520	1.15	0.89	0.78	–	–
Sensor 9	2009	7722	1.05	0.78	0.67	0.92	0.88
	2010	5812	1.08	0.82	0.67	1.03	1.05
	2008	5518	1.04	0.79	0.69	–	–
Sensor 10	2009	7689	0.94	0.68	0.58	0.91	0.86
	2010	5789	0.96	0.72	0.59	1.02	1.05
	2008	5495	1.17	0.91	0.80	–	–
Sensor 11	2009	7601	1.05	0.78	0.67	0.90	0.86
	2010	5727	1.06	0.80	0.67	1.00	1.03
	2008	2617	1.17	0.88	0.87	–	–
	2009	988	1.24	0.90	0.64	1.05	1.02
Sensor 18	2010	5944	1.08	0.85	0.72	0.88	0.95
	2011	7515	0.92	0.77	0.65	0.85	0.90
	2012	7199	0.93	0.72	0.61	1.01	0.94
	2008	1405	1.42	0.75	0.75	–	–
	2009	789	1.40	0.78	0.57	0.98	1.05
Sensor 19	2010	4555	1.20	0.70	0.65	0.86	0.90
	2011	6046	1.01	0.66	0.57	0.84	0.94
	2012	5962	0.99	0.60	0.54	0.98	0.91
	2008	2493	1.19	0.89	0.87	–	–
	2009	971	1.35	0.98	0.69	1.13	1.10
Sensor 20	2010	5852	1.12	0.89	0.76	0.83	0.91
	2011	7417	0.89	0.73	0.63	0.79	0.82
	2012	7120	0.85	0.65	0.54	0.95	0.88
	2008	2460	1.21	0.89	0.87	–	–
	2009	982	1.25	0.91	0.64	1.04	1.02
Sensor 21	2010	5908	1.10	0.86	0.73	0.88	0.94
	2011	7466	0.93	0.77	0.66	0.85	0.90
	2012	7159	0.94	0.72	0.60	1.01	0.94

Continued on next page...

Table A.2 – *Continued from previous page*

	Year	Entries	Median [mV]	IQR [mV]	Sigma [mV]	ΔMedian	ΔIQR
Sensor 22	2008	2455	1.23	0.91	0.91	–	–
	2009	977	1.29	0.94	0.67	1.05	1.02
	2010	5899	1.12	0.87	0.75	0.87	0.93
	2011	7509	0.94	0.78	0.66	0.84	0.90
	2012	7173	0.95	0.73	0.59	1.01	0.93
Sensor 23	2008	2419	1.19	0.88	0.85	–	–
	2009	986	1.22	0.88	0.62	1.02	1.00
	2010	5944	1.06	0.83	0.71	0.88	0.94
	2011	7540	0.90	0.75	0.63	0.85	0.91
	2012	7239	0.92	0.71	0.60	1.02	0.94
Sensor 24	2008	5402	1.01	0.77	0.67	–	–
	2009	7944	0.90	0.67	0.59	0.89	0.87
	2010	5742	0.91	0.69	0.58	1.02	1.04
Sensor 25	2008	5307	1.12	0.84	0.74	–	–
	2009	7764	1	0.73	0.64	0.89	0.87
	2010	5633	1.01	0.76	0.64	1.01	1.04
Sensor 26	2008	5305	1.04	0.79	0.69	–	–
	2009	7980	0.91	0.67	0.58	0.88	0.85
	2010	5727	0.92	0.69	0.58	1.01	1.03
Sensor 27	2008	5115	1.05	0.77	0.68	–	–
	2009	7376	0.92	0.65	0.56	0.87	0.83
	2010	5494	0.90	0.65	0.55	0.98	1.00
Sensor 28	2008	5148	1.03	0.77	0.67	–	–
	2009	7583	0.90	0.65	0.56	0.88	0.85
	2010	5623	0.91	0.67	0.56	1.01	1.03
Sensor 29	2008	2511	0.68	0.48	0.54	–	–
	2009	7519	0.92	0.68	0.59	1.35	1.41
	2010	5548	0.93	0.70	0.59	1.02	1.03
Sensor 31	2009	938	1.38	0.99	0.71	–	–
	2010	5745	1.17	0.94	0.77	0.85	0.95
	2011	7390	0.95	0.82	0.69	0.81	0.88
	2012	7151	0.96	0.77	0.61	1.01	0.94
Sensor 35	2008	2459	1.46	1.09	1.00	–	–
	2009	953	1.49	1.06	0.76	1.02	0.98
	2010	5790	1.23	0.97	0.81	0.82	0.91
	2011	7320	0.97	0.81	0.68	0.79	0.83
	2012	7071	0.96	0.74	0.60	0.99	0.92

A.2. Derivation of the ray equations

The correct path between two points for any physical quantity that follows a wave equation can be found by applying Fermat's principle to the problem. It states that the actual path traversed by the ray is the one that has a constant travel time when the path is varied by an infinitesimal amount. This derivation can be found in many textbooks, e.g. [37]. Expressed as a mathematical formula:

$$T = \int_{P1}^{P2} \frac{1}{c(\vec{r})} \,\mathrm{d}s \tag{A.1}$$

$$\delta T \stackrel{!}{=} 0 \tag{A.2}$$

T is the travel time, $c(\vec{r})$ is the speed of the wave at position $\vec{r}$ and $\mathrm{d}s$ is the infinitesimal displacement. Calculating the variation of the travel time and expressing the sound speed with the refraction index n yields:

$$\delta T = \delta \frac{1}{c} \int_{P1}^{P2} n \,\mathrm{d}s \tag{A.3}$$

$$= \frac{1}{c} \int_{P1}^{P2} \delta n \,\mathrm{d}s + n\delta \mathrm{d}s \tag{A.4}$$

Using Einstein's convention for sums, one can write $\mathrm{d}s = \sqrt{dx_i \cdot dx_i}$. This formula can be used to evaluate $\delta \mathrm{d}s = dx_i \mathrm{d}s^{-1} \delta dx_i = \frac{dx_i}{ds} \delta \frac{dx_i}{ds} ds$. Additionally the variation of the refraction index can be expressed by the variations of the coordinates $\delta n = \partial_{x_i} n \, \delta x_i$. Therefore one finds that

$$\delta T = \frac{1}{c} \int_{P1}^{P2} \delta n \,\mathrm{d}s + n\delta \mathrm{d}s \tag{A.5}$$

$$= \frac{1}{c} \int_{P1}^{P2} \left(\partial_{x_i} n \, \delta x_i + n \frac{dx_i}{ds} \delta \frac{dx_i}{ds} \right) \mathrm{d}s \tag{A.6}$$

Partial integration can be used to eliminate the dependency of $\delta \frac{dx_i}{ds}$:

$$\delta T = \frac{1}{c} \int_{P1}^{P2} \left(\partial_{x_i} n - \frac{d}{ds} \left(n \frac{dx_i}{ds} \right) \right) \delta x_i \,\mathrm{d}s + \left[n \frac{dx_i}{ds} \delta x_i \right]_{P1}^{P2} \tag{A.7}$$

The variation vanishes at the start and end, since only the path is varied, while the two end points remain unchanged. Thus the last term also vanishes, and the equation of motion for the ray can be read. Because we demand that this integral is zero for any variation, the integrand has to be zero:

$$\frac{d}{ds} \left(n \frac{dx_i}{ds} \right) = \frac{\partial n}{\partial x_i} \tag{A.8}$$

$$n \frac{d^2 x_i}{ds^2} = \frac{\partial n}{\partial x_i} - \frac{dx_i}{ds} \frac{dx_j}{ds} \frac{\partial n}{\partial x_j} \tag{A.9}$$

Expressing the equation with vectors might show its meaning a bit more clearly.

$$n\frac{d}{ds}\vec{t} = \nabla n - \vec{t}\left(\vec{t}\nabla n\right) \tag{A.10}$$

$\vec{t}$ is the tangential vector of the trajectory. Since we are looking for an equation that can be used by an algorithm in a computer program to calculate the path between two points in the ocean, we have to apply the formula to that concrete case. If we introduce a Cartesian coordinate system with the x-axis parallel to the surface of the ocean and the z-axis pointing upwards, $\vec{t}$ can be expressed as $(\cos\alpha, 0, \sin\alpha)^t$. Looking at a component of A.10, the final ray equations can be derived with simple algebra:

$$n\frac{d}{ds}\cos\alpha = \frac{\partial n}{\partial x} - \cos\alpha\left(\cos\alpha\,\frac{\partial n}{\partial x} + \sin\alpha\,\frac{\partial n}{\partial z}\right) \tag{A.11}$$

$$-n\sin\alpha\frac{d\alpha}{ds} = \sin^2\alpha\frac{\partial n}{\partial x} - \sin\alpha\,\cos\alpha\,\frac{\partial n}{\partial z} \tag{A.12}$$

$$\frac{d\alpha}{dx}\frac{dx}{ds} = -n^{-1}\sin\alpha\frac{\partial n}{\partial x} + n^{-1}\,\cos\alpha\,\frac{\partial n}{\partial z} \tag{A.13}$$

$$\frac{d\alpha}{dx} = -\tan\alpha\frac{1}{n}\frac{\partial n}{\partial x} + \frac{1}{n}\frac{\partial n}{\partial z} \tag{A.14}$$

$$\frac{d\alpha}{dx} = \tan\alpha\frac{1}{c}\frac{\partial c}{\partial x} - \frac{1}{c}\frac{\partial c}{\partial z} \tag{A.15}$$

the relations $n = k \cdot c^{-1}$ and $\frac{dx}{ds} = \cos\alpha$ were used. The first term describes the change of α when there is a horizontal gradient in the sound speed profile, while the second term refers to the vertical gradient. This differential equation can be simplified even more for our problem, because we assume that the ocean is isotrope at a certain depth, so $\frac{\partial c}{\partial x}$ is zero. Additionally it is advisable to use equations which do not require the calculation of transcendent functions, because it saves a lot of computational time. Instead of solving the differential equation for α and then calculating $\tan\alpha$, one can use $\sin\alpha$ and $\cos\alpha$ as coordinates. The differential equations for the trigonometric functions are determined by $\frac{d\alpha}{dx}$.

A.3. Spectra

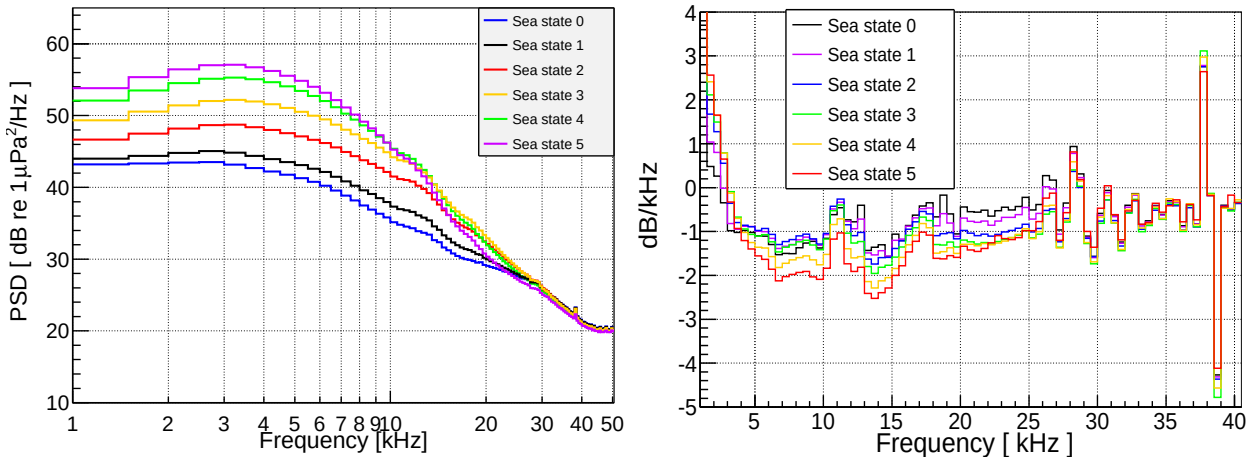

(a) Spectra (b) First derivative

Figure A.1.: *The median of the noise spectra as seen by the hydrophones on storey 2 (HTI). There are clear signals visible at multiple frequencies. The dent at* 18 kHz *is an effect of the calibration.*

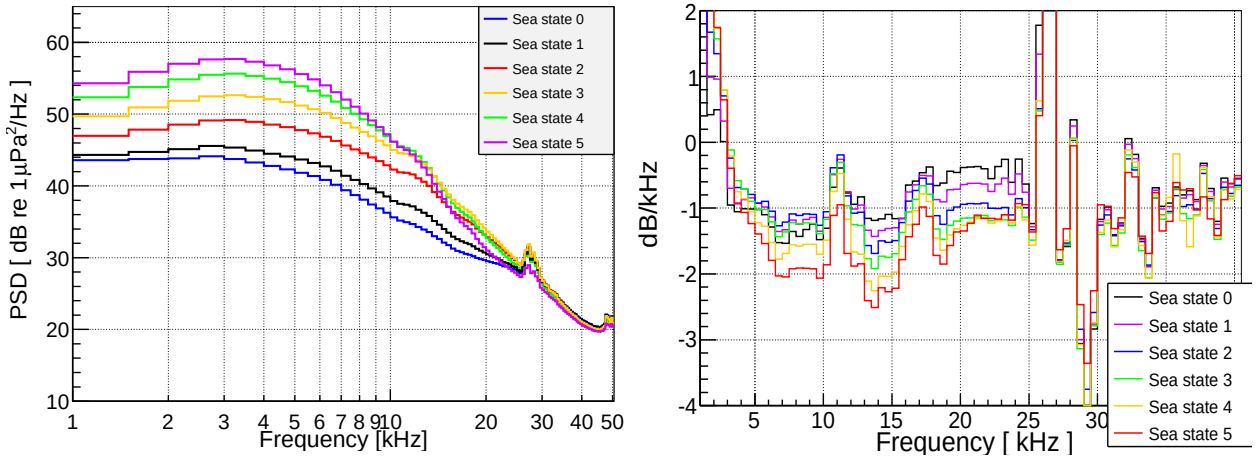

(a) Spectra (b) First derivative

Figure A.2.: *The median noise spectra recorded by the hydrophones on storey 6 (HTI). There are clear signals visible at multiple frequencies. The dent at* 18 kHz *is an effect of the calibration.*

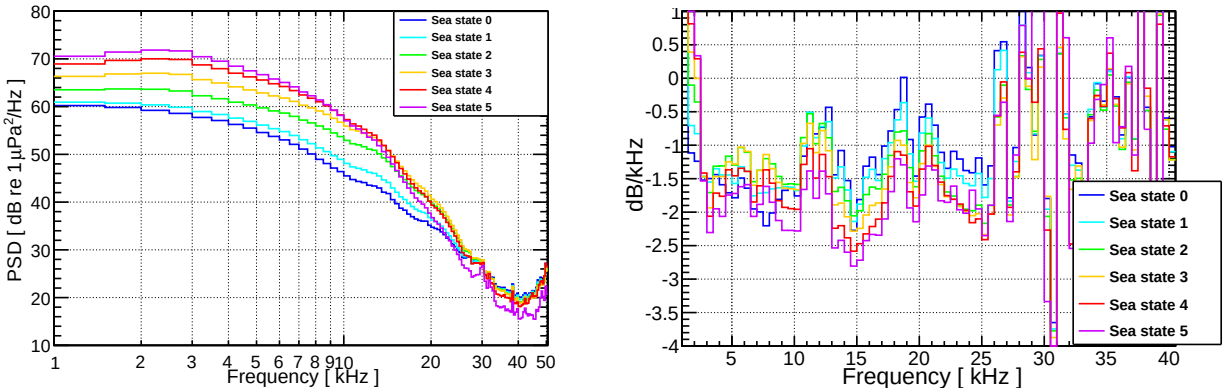

(a) Spectra (b) First derivative

Figure A.3.: *The median of the noise power spectral density recorded by sensor 5 (LTI hydrophone). The inherent noise was subtracted. The PSDs for different sea states show different slopes.*

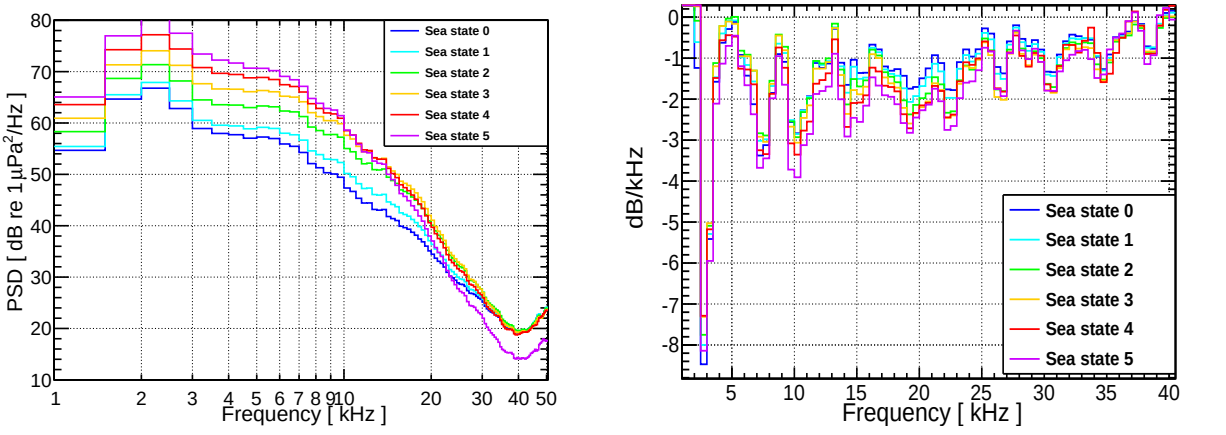

(a) Spectra (b) First derivative

Figure A.4.: *The median of the noise power spectral density recorded by sensor 14 (acoustic module). The inherent noise was subtracted and the PSDs were smoothed with ROOT. The acoustic modules deform the the spectra due to the coupling of the piezo elements to the galss sphere and reflections. The spectral index also varies with the sea state.*

A.4. Implementation of the new model

The C++ implementation of the new model is based on 8th degree polynomials fitted to the output of the raytracing program (Sec. 5), see Tab. 5.2 for the coefficients. It is possible to access the fitted polynomials directly via the functions **SpectrumSeaState_n** for sea state n. But the wind speed is obviously a continuous value, while the model only consists of 6 discrete spectra. In order to provide a framework that properly reflects the continuous nature of the problem, the discrete spectra have to be interpolated. The implementation in the function **AmbientNoiseSpectrum** first determines the current sea state A from the wind speed (according to Tab 3.2). Then a scaling value q is calculated from the difference in wind speed to the next sea state B. Finally, the linearly interpolated value

$$S(v, f) = A(f) \cdot (1 - q(v)) + q(v) \cdot B(f) \tag{A.16}$$

is returned. Therefore a continuous function for both input parameters is created. The valid range for these values is 0 kn to 25 kn ($0\,\mathrm{m\,s^{-1}}$ to $15\,\mathrm{m\,s^{-1}}$) and 5 kHz to 30 kHz. In order to prevent the polynomial from growing indefinitely, an exponential decay of the spectrum is added for frequencies above 70 kHz, ensuring that no unexpected behavior occurs. There is also another function **AmbientThermalNoise** that returns the output of the previous one and the thermal noise added using this formula:

$$TN(f) = -15 + 20 \log_{10}(f) \tag{A.17}$$

$$NL(f) = 10 \log_{10}\left(10^{-0.1 \cdot S(v,f)} + 10^{-0.1 \cdot TN(f)}\right) \tag{A.18}$$

Bibliography

[1] K. Greisen, 'End to the cosmic ray spectrum?', *Phys. Rev. Lett.*, 16 (1966) p. 748.

[2] G. T. Zatsepin and V. A. Kuzmin, 'Upper limit of the spectrum of cosmic rays', *JETP Lett.*, 4 (1966) p. 78.

[3] 'Erlangen Centre for Astroparticle Physics', Website, `http://www.ecap.nat.uni-erlangen.de/`.

[4] 'Antares Modules for Acoustic Detection under the Sea', Website, `http://www.ecap.nat.uni-erlangen.de/acoustics/research/amadeus_project/index.shtml`.

[5] 'Astronomy with a Neutrino Telescope and Abyss environmental RESearch', Website, `http://antares.in2p3.fr/`.

[6] C. L. Naumann, *Development of sensors for the acoustic detection of ultra high energy neutrinos in the deep sea*, Dissertation, Friedrich-Alexander-Universität Erlangen-Nürnberg (2007).

[7] K. Graf, *Experimental Studies within ANTARES towards Acoustic Detection of Ultra-High Energy Neutrinos in the Deep-Sea*, Dissertation, Friedrich-Alexander-Universität Erlangen-Nürnberg (2008).

[8] M. Neff, *Studie zur akustischen Teilchendetektion im Rahmen des ANTARES-Experiments: Entwicklung und Integration von Datennahmesoftware*, Diploma-thesis (FAU-PI1-DIPL-07-003).

[9] N. Kurahashi and G. Gratta, 'Oceanic Ambient Noise as a Background to Acoustic Neutrino Detection', *Phys. Rev. D*, 78 (2008) p. 092001, DOI:10.1103/PhysRevD.78.092001.

[10] J. Aguilar et al., 'AMADEUS - The Acoustic Neutrino Detection Test System of the ANTARES Deep-Sea Neutrino Telescope', *Nucl. Instrum. Meth. A*, 626-627 (2011) pp. 128–143.

[11] J. Aguilar et al., 'ANTARES: the first undersea neutrino telescope', *Nucl. Instrum. Meth. A*, 656 (2011) pp. 11–38, arXiv:1104.1607 [astro-ph.IM].

[12] S. Adrián-Martínez et al., 'The positioning system of the ANTARES Neutrino Telescope', *JINST*, 7 (2012), T08002.

[13] J. A. Aguilar et al., 'Background light in potential sites for the ANTARES undersea neutrino telescope', *Astrop. Phys.*, 13 (2000) pp. 127–136, arXiv:astro-ph/9910170.

[14] J. A. Aguilar et al., 'Sedimentation and Fouling of Optical Surfaces at the ANTARES Site', *Astrop. Phys.*, 17 (2003) pp. 253–267, arXiv:astro-ph/0206454.

[15] J. A. Aguilar et al., 'Transmission of light in deep sea water at the Antares site', *Astrop. Phys.*, 23 (2005) pp. 131–155, arXiv:astro-ph/0412126.

[16] 'Listen to the Deep Ocean Environment', Website (2012), `http://www.listentothedeep.com/`.

[17] P. A. Cherenkov, '[Visible emission of clean liquids by action of γ radiation]', *Doklady Akademii Nauk SSSR*, 2 (1934) p. 451.

[18] G. A. Askariyan et al., 'Acoustic Detection of High Energy Particle Showers in Water', *Nucl. Instr. and Meth.*, 164 (1979) p. 267.

[19] J. Learned, 'Acoustic Radiation by Charged Atomic Particles in Liquids', *Phys. Rev. D*, 19 (1979) p. 3293.

[20] K. Graf et al., 'Testing Thermo-Acoustic Sound Generation in Water with Proton and

Laser Beams', in *Acoustic and Radio EeV Neutrino Detection Activities (ARENA 2005)*, ed. R. Nahnhauer and S. Böser, *Int. J. Mod. Phys.*, A21 (2006) pp. 127–131.

[21] 'High Tech, Inc.', Website (2013), `http://www.hightechincusa.com/`.

[22] J. Müller, *Untersuchung zum Tiefsee-Hintergrundrauschen am ANTARES-Standort*, Bachelor-thesis (ECAP-2010-041), Friedrich-Alexander Universität Erlangen-Nürnberg (2010).

[23] CERN, 'ROOT, A Data Analysis Framework', Software (2013), `http://root.cern.ch/drupal/`.

[24] M. Neff, *Studies on the Selection of Neutrino-like Signals for the Acoustic Detection Test Device AMADEUS*, Dissertation, Friedrich-Alexander-Universität Erlangen-Nürnberg (2012).

[25] V. O. Knudsen, R. S. Alford and J. W. Emling, 'Underwater ambient noise', *J. Mar. Res.*, 3 (1948) p. 410.

[26] R. H. Mellen, 'The Thermal-Noise Limit in the Detection of Underwater Acoustic Signals', *J. Acoust. Soc. Am.*, 24 (1952) pp. 478–490.

[27] B. Bergmann, *Untersuchung zum Tiefsee-Hintergrundrauschen am ANTARES-Standort*, Bachelor-thesis (ECAP-2010-042), Friedrich-Alexander Universität Erlangen-Nürnberg (2010).

[28] 'Corsica Ferries', Website (2012), `http://www.corsica-ferries.de/`.

[29] 'MarineTraffic', Website (2012), `http://marinetraffic.com/ais/`.

[30] Met Office, Hadley centre, 'HadISST 1.1 - Global sea-Ice coverage and SST (1870-Present)', Website (2012), `http://www.metoffice.gov.uk/hadobs/hadisst/`.

[31] M. Rutkowska et al., 'Degradation of polyurethanes in sea water', *Polymer Degradation and Stability*, 76 (2002) pp. 233–239.

[32] M. A. Ainslie and J. G. McColm, 'A simplified formula for viscous and chemical absorption in sea water', *J. Acoust. Soc. Am.*, 103 (1998), 3 pp. 1671–1672.

[33] APL–UW author team, 'APL–UW High-Frequency Ocean Environmental Acoustic Models Handbook', Tech. Rep. APL–UW 9407, Applied Physics Laboratory, University of Washington (1994).

[34] ACoRNe Collaboration, 'The ACoRNe Acoustic Simulator', Matlab code, `http://www.hep.shef.ac.uk/research/acorne/shower.php`.

[35] S. Bevan et al., 'Simulation of ultra high energy neutrino induced showers in ice and water', *Astrop. Phys.*, 28 (2007), 3 pp. 366–379.

[36] MathWorks, Inc., 'MATLAB', Software (2013), `http://www.mathworks.com/products/matlab/`.

[37] W. Munk, P. Worcester and C. Wunsch, *Ocean Acoustic Tomography*, Cambridge University Press (1995).

List of Figures

List of Tables

Erklärung

Hiermit bestätige ich, dass ich diese Arbeit selbstständig und nur unter Verwendung der angegebenen Quellen und Hilfsmittel angefertigt habe.

Erlangen, den 26. März 2013

Dominik Kießling